

# TRIBOLOGICAL BEHAVIOR OF POROUS AL ALLOYS

by

Avijit Sinha

Submitted in partial fulfilment of the requirements  
for the degree of Master of Applied Science

at

Dalhousie University  
Halifax, Nova Scotia  
March 2015

© Copyright by Avijit Sinha, 2015

# TABLE OF CONTENTS

LIST OF TABLES .....	v
LIST OF FIGURES .....	vi
ABSTRACT .....	ix
LIST OF ABBREVIATIONS AND SYMBOLS USED.....	x
ACKNOWLEDGEMENTS.....	xii
CHAPTER 1 INTRODUCTION.....	1
CHAPTER 2 LITERATUR REVIEW .....	4
2.1 Why Aluminium Alloys .....	4
2.2 Application of Al Alloy in Automotive Industry .....	5
2.3 Designation of Aluminium Alloys .....	6
2.3.1 Wrought Aluminum Alloy Designation System.....	7
2.3.2 Cast Aluminum Alloy Designation System.....	9
2.4 Porosity in Al Casting .....	10
2.5 Powder Metallurgy Processing.....	12
2.5.1 Powder Production .....	12
2.5.2 Powder Mixing and Blending.....	16
2.5.3 Compaction.....	17
2.5.4 Sintering .....	21
2.6 Cold Isostatic Pressing .....	24
2.7 Porosity in Al Powder Metallurgy.....	25
2.8 Wear .....	26
2.9 Mechanism of Wear .....	26
2.9.1 Abrasive Wear.....	26
2.9.2 Adhesive Wear .....	29

2.9.3 Surface Fatigue.....	30
2.9.4 Erosive Wear.....	31
2.9.5 Fretting Wear.....	33
2.9.6 Delamination.....	34
2.10 Wear Behavior of Aluminium.....	36
2.11 Wear Regime Maps in Al-Si alloys.....	37
2.12 Effect of Silicon Content on Wear.....	41
2.13 Effect of Grain Size on Wear.....	43
2.14 Effect of Porosity on Wear.....	43
CHAPTER 3 EXPERIMENTAL METHODS.....	45
3.1 Materials.....	45
3.2 Powder Metallurgy Specimens Preparation.....	45
3.2.1 Powder Blending.....	45
3.2.2 Powder Compaction.....	46
3.2.3 Sintering.....	47
3.3 Materials Microstructural Characterization.....	48
3.3.1 Optical Microscopy.....	48
3.3.2 Porosity Measurement.....	49
3.3.3 Area Percent Porosity.....	51
3.3.4 X-ray Diffraction.....	52
3.4 Macro and Micro Mechanical Properties.....	53
3.4.1 Rockwell Hardness Testing.....	53
3.4.2 Nanoindentation.....	54
3.5 Tribological Characterization.....	56
3.5.1 Reciprocating Wear Test.....	56
3.6 Scratch Testing.....	58
3.7 Scanning Electron Microscopy (SEM).....	59

3.8 Optical Profilometer .....	59
CHAPTER 4 RESULTS AND DISCUSSION .....	61
4.1 Materials Characterization.....	61
4.1.1 Al A380M alloy.....	61
4.1.2 Pure Al and Al 6061 .....	64
4.1.2.1 Powder Characterization.....	64
4.1.2.2 Pore formation in Sintered Pure Al and Al 6061 Alloy.....	69
4.2 Effect of Porosity on Mechanical Properties .....	75
4.3 Effect of Surface Porosity on Wear Rate.....	80
4.4 Effect of Normal Load and Coefficient of Friction on Wear Behavior.....	85
4.5 Worn Surface Evolution .....	89
4.6 Scratch Behavior of Porous Pure Al and Al 6061 .....	103
CHAPTER 5 CONCLUSIONS AND RECOMMENDATIONS.....	114
REFERENCES.....	116
Appendix A: Raw Data .....	130

## LIST OF TABLES

Table 2.1 Wrought alloy designation system.....	8
Table 2.2 Cast alloy designation system.....	10
Table 3.1 Basic properties of sintered pure Al .....	50
Table 3.2 Basic properties of sintered Al 6061.....	50
Table 3.3 Operating conditions for reciprocating wear test.....	58
Table 4.1 Composition of Al A380M aluminium alloy.....	61
Table 4.2 Microstructural characteristics of Al A380M.....	63
Table 4.3 Chemical composition of pure Al and Al 6061 powders.....	65
Table 4.4 Particle size distribution of pure Al and Al 6061 .....	68
Table 4.5 Microstructural characteristics and hardness values of sintered pure Al and Al 6061 .....	74
Table 4.6 Nanoindentation test data for Al A380M .....	77
Table 4.7 Nanoindentation test data for porous pure Al and Al 6061 alloy .....	79
Table 4.8 Scratch test data for porous pure Al and Al 6061 .....	103

## LIST OF FIGURES

Figure 1.1 Top view of center support assembly .....	2
Figure 2.1 Typical porosity in cast aluminum alloy .....	11
Figure 2.2 Formation of metal powder by gas atomization near the gas nozzle .....	13
Figure 2.3 Typical air atomization process.....	14
Figure 2.4 Water atomization process .....	15
Figure 2.5 Action of a jar mill .....	16
Figure 2.6 Particle deformation with increasing pressure during uniaxial compaction .....	18
Figure 2.7 Sequence for die compaction .....	19
Figure 2.8 A plot of density versus compaction pressure during metal powder.....	20
Figure 2.9 Density profile in single action and double action compaction .....	20
Figure 2.10 Different stages of sintering, (a) initial stage, (b) intermediate stage, (c) final stage .....	23
Figure 2.11 The sequence of steps leading to pore isolation and spheroidization.....	24
Figure 2.12 Cold isostatic pressing system.....	25
Figure 2.13 Abrasion wear.....	28
Figure 2.14 Different abrasion mechanism.....	29
Figure 2.15 Schematic representation of adhesive wear.....	30
Figure 2.16 Schematic of fatigue wear due to formation of surface and subsurface cracks.....	31
Figure 2.17 Schematic of erosive wear.....	32
Figure 2.18 Schematic of cavitation erosion due to impingement of liquid bubbles .....	33
Figure 2.19 Delamination wear.....	35
Figure 2.20 Wear map for steel-on-steel during dry sliding.....	39
Figure 2.21 Wear map of aluminum alloy outlining the boundaries for each wear mechanism .....	39
Figure 2.22 Void and crack nucleation around the silicon particles under the contact surface.....	40
Figure 2.23 Wear rate versus load for four different Al-Si alloy systems .....	40
Figure 2.24 Wear mechanism map for aluminum alloy .....	41
Figure 3.1 Turbula Model T2M Mixer used for homogenizing the powder .....	45
Figure 3.2 Cold isostatic pressing machine .....	46
Figure 3.3 Lindberg tube furnace used to sinter green compacts .....	47
Figure 3.4 Temperature profile during sintering of pure Al and Al 6061 powders.....	48

Figure 3.5 Olympus BX51 research microscope .....	49
Figure 3.6 Bruker D8-Advance XRD system .....	53
Figure 3.7 Rockwell hardness tester (Leco R600).....	54
Figure 3.8 Berkovich diamond indenter .....	56
Figure 3.9 Reciprocating wear tester .....	57
Figure 3.10 Schematic diagram of scratch tester .....	59
Figure 3.11 Optical profilometer .....	60
Figure 4.1 XRD pattern of Al A380M alloy.....	62
Figure 4.2 Optical micrograph of HPDC A380M Al .....	63
Figure 4.3 SEM images of raw powders (a) pure Al (b) Al 6061 .....	64
Figure 4.4 XRD pattern of pure Al .....	65
Figure 4.5 XRD pattern of Al 6061 .....	66
Figure 4.6 Particle size distribution curve for pure Al .....	67
Figure 4.7 Particle size distribution curve for Al 6061.....	67
Figure 4.8 Optical micrographs of pure Al samples mixed with (a) no wax (b) 1.5% wax (c) 10.5% wax (d) 14.5% wax.....	71
Figure 4.9 Optical microscopy of Al 6061 samples mixed with (a) no wax (b) 1.5% wax (c) 10.5% wax (d)14.5% wax.....	73
Figure 4.10 Variation in hardness with surface porosity for pure Al and Al 6061.....	76
Figure 4.11 Load vs indentation depth profile for A380 M alloy.....	77
Figure 4.12 Load vs depth profile for (a) pure Al and (b) Al 6061 using 100 mN load.....	79
Figure 4.13 Weight loss versus sliding distance curve for (a) pure Al (1.9% porosity) and (b) Al 6061(3.5% porosity) .....	82
Figure 4.14 Wear rate versus surface porosity for pure Al under 10 Hz frequency .....	83
Figure 4.15 Wear rate versus surface porosity for Al 6061 under 10 Hz frequency .....	83
Figure 4.16 Schematic diagram depicting the effect of (a) non-uniform and (b) uniform pore distribution on wear rate.....	84
Figure 4.17 Normal load vs wear rate for (a) Al A380M alloy (b) pure Al (1.9% porosity) .....	86
Figure 4.18 COF vs load for Al A380M alloy.....	87
Figure 4.19 COF vs surface porosity for pure Al and Al 6061 at 3N load.....	88

Figure 4.20 Optical profilometry scans of wear tracks; (a, b) Al A380M at 3, 4 and 5N load and 10 Hz frequency.....	90
Figure 4.21 Optical profilometry scans of wear tracks; (a, b) pure Al (1.9%porosity) and (c, d) (15.1% porosity) at 3, 4 and 5N load and 10 Hz frequency. ....	90
Figure 4.22 Optical profilometry scans of wear tracks; (a, b) Al 6061 (3.5%porosity) and (c, d) (20.7% porosity) at 3, 4 and 5N load and 10 Hz frequency. ....	91
Figure 4.23 Volume loss vs surface porosity for (a) pure Al and (b) Al 6061 .....	92
Figure 4.24 SEM micrographs of worn surface (a,b,c) and (d) EDS analysis of wear track for Al A380M alloy.....	95
Figure 4.25 SEM images of worn surface (a,b,c,d) for porous pure Al.....	98
Figure 4.26 SEM images of worn surface (a,b,c,d) for porous Al 6061 alloy.....	100
Figure 4.27 EDS analysis of wear tracks for (a) pure Al and (b) Al 6061 alloy .....	101
Figure 4.28 Wear debris at 2.5N load and 10 Hz a) pure Al b) Al 6061 .....	102
Figure 4.29 SEM micrographs of scratch track for pure Al (1.9% porosity) .....	106
Figure 4.30 SEM micrographs of scratch track for pure Al (15.1% porosity) .....	108
Figure 4.31 SEM micrographs of scratch track for pure Al (3.5% porosity) .....	111
Figure 4.32 SEM micrographs of scratch track for pure Al (20.7% porosity) .....	113

## **ABSTRACT**

Aluminium alloys are becoming attractive for critical structural applications for their light weight, high specific strength, high corrosion resistance and good heat conductivity. It is suitable for manufacturing many components such as clutch housings in the automotive industry. These alloys can be fabricated using powder metallurgy techniques in which porosity is a common feature. The presence of pores is responsible for decreasing the effective load bearing cross-sectional area and act as a stress concentration site for strain localization and damage, decreasing both strength and ductility. Not only the total area percentage of porosity influences the degradation in properties but the size, shape and inter connectivity of the porosity also play an important role. The present study aims to establish a better understanding of the relationship between surface porosity and corresponding wear behavior. In this study, porous specimens were produced using powder metallurgy techniques. The extent of wear damage and the type of wear was investigated under low load range of 1.5-5N against a AISI 52100 bearing steel ball using a reciprocating ball-on-flat wear configuration and frequency of 10 Hz. Scanning electron microscopy of the wear tracks and wear debris was carried out to identify wear mechanisms. This study revealed that due to the combined effect of the real area of contact and subsurface cracking, wear rate increased with increasing porosity content. The friction and wear behavior of Al A380M, pure Al and Al 6061 as a function of porosity content can be attributed to their hardness and corresponding wear mechanism.

## LIST OF ABBREVIATIONS AND SYMBOLS USED

Symbols	Description
A	Area of contact
$A_{A_i}$	The area fraction of the porosity of $i^{\text{th}}$ field
$\overline{A_A}$	The average area fraction of porosity of the total 'n' field
$A_r$	Real area of contact
dp/dh	Slope at maximum load
$E^*$	Elastic modulus
$E_1$	Elastic modulus for Berkovich indenter
$E_2$	Elastic modulus for test material
EDS	Energy-dispersive X-ray spectroscopy
F	Force (N)
$F_N$	Applied load
$F_X$	Tangential load (N)
$F_Z$	Normal load (N)
$F_T$	Tangential force
95% CI	95% confidence interval
% RA	Percent relative accuracy
CIP	Cold Isostatic Pressing
COF	Coefficient of friction

$h_c$	Contact depth
$h_{max}$	Maximum indentation depth
H	Hardness
Hs	Scratch hardness
HPDC	High pressure die casting
HRH	Rockwell hardness H scale
$P_{max}$	Maximum applied load
P/M	Powder metallurgy
$\rho_{Green}$	Green density of the compact
$\rho_{water}$	Water density
$\rho_{Sintered}$	Sintered density of the compact
s	Sliding distance
SEM	Scanning Electron Microscopy
UMT	Universal Micro-Tribometer
$\nu_1$	Poisson's ratio of Berkovich indenter
$\nu_2$	Poisson's ratio of test material
<i>Vol % porosity</i>	Volume percentage of porosity
XRD	X – Ray Diffraction

## **ACKNOWLEDGEMENTS**

The author would like to acknowledge the guidance, inspiration and continuous support offered by Dr. Zoheir Farhat throughout this project. The author would like to thank Auto21 for financial assistance, Magna Powertrain for providing A380M aluminum alloy. The author would also like to thank Dr. D.P Bishop and Randy Cooke for their assistance with sample preparation. The author is grateful to Advanced Tribology Lab member Md. Aminul Islam for his assistance and suggestions during the entire project. Moreover, the excellent technical support offered by Mr. Dean Grijm, and Mrs. Patricia Scallion is highly appreciated.

Finally, the author would like to acknowledge the support of his family and friends, who have always been there for him throughout his academic career.

## CHAPTER 1 INTRODUCTION

In automotive applications, aluminium is an attractive alternative to ferrous alloys due to its high strength to weight ratio and high thermal conductivity. The combination of light weight, high strength, good corrosion and impact resistance made aluminium alloys suitable candidates for many applications [1,2]. However, their low wear resistance compared to other materials (i.e. steels, ceramics) limits their use. The wear response of aluminium alloys significantly depends on microstructural features such as the nature, size, shape and distribution of micro-constituents (porosity and second phase particles) [3]. It is well established that these microstructural features are functions of the fabrication processes employed [4,5].

High pressure die casting (HPDC) is a common method for producing aluminium parts. It is a fully automated, large volume, high productivity process for the production of complex, thin walled near net shape castings. Due to their smooth surface finish and excellent dimensional tolerance, most high pressure die castings require no machining except the removal of flash around edges and possible drilling and tapping holes. More recently, near net shape processing of aluminium by classical press and sinter powder metallurgy has emerged as unique and important metal forming method [6]. Minimum metal loss, low energy consumption and ability to produce variety of alloy systems have made powder metallurgy attractive. Powder metallurgy is being used to produce complex automobile parts such as connecting rods, cams, roller bearings, cylinder liners, etc. [7-13].

Magna powertrain, is a leading supplier for the global automobile industry in the fields of powertrain design, development, testing and manufacturing. They manufacture the center support assembly of a double sided clutch housing used to support the power transmission shaft. But their high pressure die cast (HPDC) components are prone to porosity formation which leads to poor tribological characteristics. The top view of the double sided clutch housing is shown in Figure 1.1. The cavity shown in this Figure is known as the piston cavity and the surrounding surface of the cavity is known as the 'seal surface.' Porosity in the seal surface causes lack of pressure tightness and decreases the strength and ductility. Piston slides into the piston cavity with a linear reciprocating back and forth motion. Due to the presence of porosity, reciprocating friction between the piston and the seal surface creates wear damage leading to premature failure.

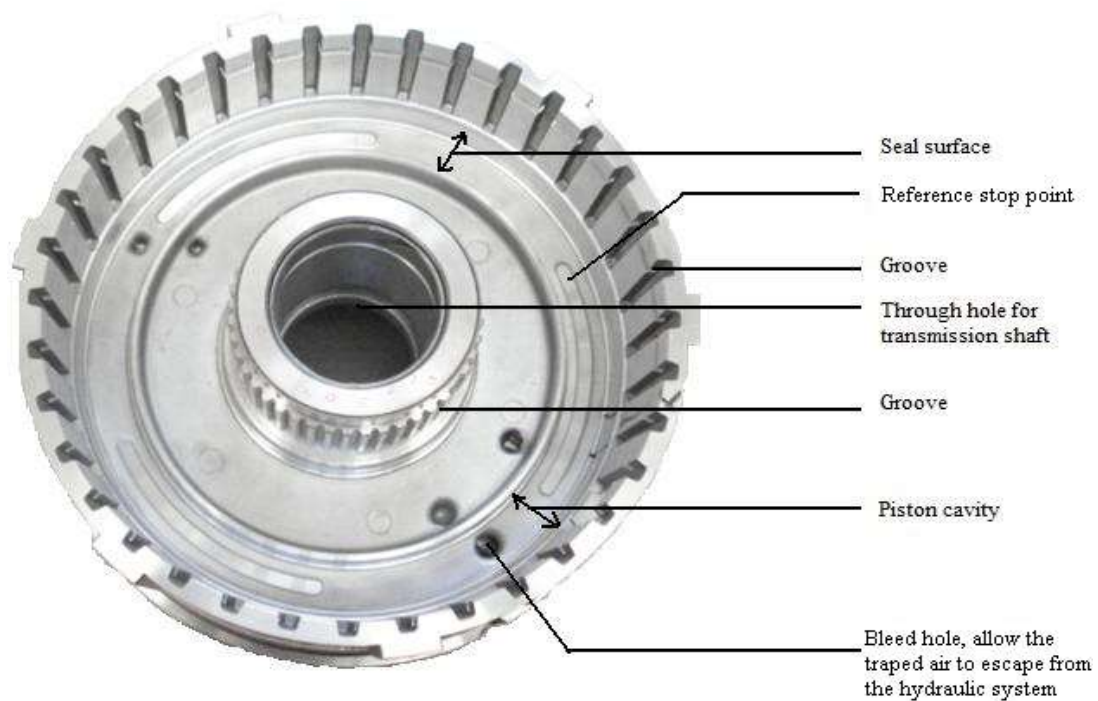


**Figure 1.1 Top view of center support assembly**

The influence of porosity on the wear behavior is not clearly understood [14,15], it has been reported in some studies as beneficial and in others as detrimental. Chen et al. [16] investigated the influence of porosity on composite materials and concluded that porosity could be beneficial to the performance of materials under some conditions. They suggested that porosity may help absorb the impact energy that accompanies crack splitting, which reduces crack propagation, thus delays rapid fracture. A study conducted by Simchi and Danninger [17] showed a positive influence of porosity on wear behavior.

Commonly, the presence of pores has a detrimental effect on the wear performance of materials [18-30]. The potentially negative effect of porosity on the wear resistance is influenced by pore size, shape, distribution and density. Pores act as pre-existing incipient cracks in the subsurface layer, waiting to become unstable at an appropriate stress level [31]. Porosity is accompanied by a decrease in mechanical properties of materials such as strength and ductility [32-34]. For instance, Hardin and Beckermann [35] demonstrated an apparent reduction in elastic moduli of components due to the presence of pores. Experiments performed by Deshpande and Lin [36] reported that porosity in materials decreases their wear resistance due to the no-load bearing characteristics of pores on the wear surface. They also explained

that depending on pore geometry and distribution, wear resistance varies and may promote severe wear. Suh [37] has found that an increase in porosity content reduces the required crack length needed to link up pores which promotes delamination. The effect of porosity on the wear and friction of metals has been studied by Vardavoulias et al. [38], they suggested that the pores enhance surface roughness of the materials, decrease the real area of contact between two sliding surfaces and consequently increase the contact pressure and promote particle detachment during sliding. Gui et al. [39] considered pores as crack sources which can be created when an external force is applied. In general, high porosity in materials leads to low strength and high wear rate [40].

Hence, a detailed understanding of the effect of porosity is necessary to assess wear properties of cast and P/M Al alloys. In this study, an attempt has been made to identify the relationship between surface porosity and wear behavior of aluminium alloys. In addition, wear behavior of different microstructures (from different production methods) was investigated. A series of reciprocating wear tests have been conducted under different loads and wear mechanisms are identified.

## CHAPTER 2 LITERATURE REVIEW

### 2.1 Why Aluminium Alloys

The properties of Aluminium and its alloys that make them the most economically attractive for a wide variety of applications are:

**Light weight:** Aluminium weighs roughly one-third as much as most of the common metals, but is one and a half times as heavy as Magnesium. It is employed in applications to reduce weight of components and structures, particularly linked to transport, especially in automotive and aerospace.

**High strength-to-weight ratio:** Due to having high strength to weight ratio aluminium is used advantageously in applications where high strength and low weight are required.

**Ease of fabrication and machinability:** It can be easily cast, rolled to any desired thickness (aluminium foils are common), stamped, drawn, spun, forged and extruded to all shapes.

**High resistance to atmospheric corrosion:** When aluminium is exposed to air, a thin aluminium oxide passive film forms on the surface, protecting the metal from corrosion. When scratched, the layer rapidly reforms retaining the protection. This feature is utilized in construction, buildings and household utensils.

**Resilience under static and dynamic loading:** Aluminium products behave elastically under static and dynamic loading conditions, that is, they have the ability to resume both shape and size, which is desirable when flexibility is required.

**Strength at low temperature:** Brittle fracture problems do not occur with aluminium. Aluminium does not undergo ductile to brittle transformation at low temperature as common in steels making them particularly suitable for low temperature applications.

**Electrical and thermal conductivity:** Aluminium is an excellent conductor of both heat and electricity. The great advantage of aluminium is that by weight, the conductivity of aluminium is around twice that of copper. This made aluminium the most commonly used material in large power transmission lines.

**Recycling:** The recyclability of aluminium is unparalleled. When recycled there is no degradation in properties compared to virgin aluminium. Furthermore, recycling of aluminium only requires around 5 percent of the input energy required to produce virgin aluminium metal.

## 2.2 Application of Al Alloy in Automotive Industry

Car manufacturers first started to use aluminium over a hundred years ago. Back then aluminium was a new and a poorly explored metal, however its light weight and corrosion resistance showed its great potential for application in the emerging automotive industry. The first sports car featuring a body made of aluminium was presented to the general public at the Berlin international motor show in 1899. The first engine with aluminium parts was made two years later in 1901. The 'light metal' added to the handling of the car, but difficulties in metal working, lack of knowledge and its high price impeded the use of aluminium in mass car production at the beginning of the century.

Recently, light weight, high strength alloys are in high demand in the automotive industry due to the desire to reduce automobile weight to provide more energy efficient vehicles. Thus, using aluminum alloy is attractive as it has excellent mechanical and fatigue properties, low density, resistance to corrosion, a high strength to weight ratio and reasonable cost. At present, vehicles manufactured in North America use average of 250 pounds of aluminum which is 2.5 times more than the amount of aluminum used thirty years ago [41]. Aluminum is used in many different systems in vehicles, including:

- Powertrain components (i.e. pistons, transmission cases, and engine blocks)
- Radiators and heat exchangers
- Wheels
- Closure panels (i.e. hoods, deck lids, and fenders)
- Chassis and suspension parts (i.e. brake calipers, knuckles, and cross members)

Some of these areas have covered nearly 100% of the market, such as pistons, transmission cases, radiators, and heat exchangers. Others, such as engine blocks and wheels, have nearly 70% of the market. The idea of using aluminum for the primary body structure has been explored, with varying success. Currently, only a few lower-volume and higher-cost vehicles use aluminum body parts. As the body is the single largest component of the entire vehicle, this area offers the greatest opportunity for the use of aluminum to grow in the automotive industry. By using aluminum instead of steel, the weight of the car body can be reduced by 40%; although strength is not the limiting factor, aluminum was found to be lacking the stiffness that steel provides [42]. Thus, further improvements need to be made in order to fully integrate aluminum alloys into the production of certain major automotive parts.

## **2.3 Designation of Aluminium Alloys**

### **Designation Criteria**

Aluminium alloys may be divided into two broad classes, cast and wrought products. These two classes can be further subdivided into families of alloys based on chemical composition and finally on temper designation. The alloy and temper designation systems in use today for wrought aluminum were adopted by the aluminum industry in about 1955, the current system for cast aluminium was developed somewhat later. The aluminum industry managed the creation and continues the maintenance of the systems through its industry organization, The Aluminum Association. The alloy registration process is carefully controlled and its integrity is maintained by the Technical Committee on Product Standards of the Aluminum Association, made up of industry standards experts.

### **Alloying Elements**

The principal alloying elements are copper, silicon, manganese, magnesium, lithium and zinc. Elements such as nickel, chromium, titanium, zirconium and scandium may be added in small amounts to achieve specific properties. Other elements may also be present in small amounts as unwanted impurities. These elements, known as tramp or residual elements have no beneficial effects on mechanical properties and the aluminium producers attempt to eliminate these from their products. The main effects of the alloying elements are as follows:

Manganese (Mn) and Magnesium (Mg) increase strength through solid solution strengthening and improve work hardening ability. Copper (Cu) gives substantial increase in strength, permits precipitation hardening, increases corrosion resistance, ductility and weldability. Silicon (Si) increases strength and ductility and in combination with magnesium produces precipitation hardening. Zinc (Zn) substantially increases strength through precipitation hardening. Iron (Fe) increases strength of pure aluminium, generally is a residual element. Chromium (Cr) increases stress corrosion resistance. Nickel (Ni) improves elevated temperature strength. Titanium (Ti) and Zirconium (Zr) are used as a grain-refining elements, particularly in filler metals. Lithium (Li) and Scandium (Sc) substantially increase strength, Young's modulus and provide precipitation hardening.

### **2.3.1 Wrought Aluminum Alloy Designation System**

The Aluminum Association Wrought Alloy Designation System consists of four numerical digits, sometimes with alphabetic prefixes or suffices, but normally just the four numbers: The first digit defines the major alloying class of the series, starting with that number. The second defines variations in the original basic alloy; that digit is always a zero (0) for the original composition, a one (1) for the first variation, a two (2) for the second variation, and so forth; variations are typically defined by differences in one or more alloying elements of 0.15–0.50% or more, depending upon the level of the added element. The third and fourth digits designate the specific alloy within the series; there is no special significance to the values of those digits except in the 1xxx series (see below), nor are they necessarily used in sequence. Table 2.1 shows the meaning of the first of the four digits in the alloy designation system. The alloy family is identified by that number and the associated main alloying ingredient(s).

**Table 2.1 Wrought Alloy Designation System**

<b>Alloy</b>	<b>Main Alloying Element</b>
1000	Mostly pure aluminum; no major alloying additions
2000	Copper
3000	Manganese
4000	Silicon
5000	Magnesium
6000	Magnesium and silicon
7000	Zinc
8000	Other elements (e.g., iron or tin)
9000	Unassigned

Members of the 1000 series family are commercially pure aluminum or special purity versions, and as such do not typically have any alloying elements intentionally added; however they contain minor impurities that are not removed unless the intended application requires it. The 8000 series family is an “other elements” series, comprised of alloys with rather unusual major alloying elements such as iron and nickel. The 9000 series is unassigned. The major benefits of understanding this designation system are that one can tell a great deal about the alloy just from knowing to which series it belongs. As indicated earlier, the 1xxx series are pure aluminum and its variations; compositions of 99.0% or more aluminum are by definition in this series. Within the 1xxx series, the last two of the four digits in the designation indicate the minimum aluminum percentage. These digits are the same as the two digits to the right of the decimal point in the minimum aluminum percentage specified for the designation when expressed to the nearest 0.01%. As with the rest of the alloy series, the second digit indicates modifications in impurity limits or intentionally added elements. Compositions of the 1xxx series do not respond to any solution heat treatment but may be strengthened modestly by strain hardening. The 2xxx series alloys have copper as their main alloying element and because it will go into solid solution in aluminum in significant amounts, will respond to solution heat treatment; which are referred to as heat treatable. The 3xxx series alloys are based on manganese and are strain hardenable; they do not respond to solution heat treatment. The 4xxx series alloys are based on silicon; some alloys are heat treatable, others are not, dependent upon

the amount of silicon and the other alloying constituents. The 5xxx series alloys are based on magnesium and are strain hardenable, not heat treatable.

### **2.3.2 Cast Aluminum Alloy Designation System**

The designation system for cast aluminum alloys is similar in some respects to that for wrought alloys but has a few very important differences as noted by the following description. Like the wrought alloy system, the cast alloy designation system also has four digits, but differs from the wrought alloy system in that a decimal point is used between the third and fourth digits to make clear that these are designations to identify alloys in the form of castings or foundry ingot for the wrought alloy designation system.

The first digit indicates the alloy group, as can be seen in Table 2.2. For 2xx.x through 8xx.x alloys, the alloy group is determined by the alloying element present in the greatest mean percentage, except cases in which the composition being registered qualifies as a modification of a previously registered alloy. Note that in Table 2.2, the 6xx.x series is shown last and are designated as the unused series. The second and third digits identify the specific aluminum alloy or, for the aluminum 1xx.x series, indicate purity. If the greatest mean percentage is common to more than one alloying element, the alloy group is determined by the element that comes first in sequence. For the 1xx.x group, the second two of the four digits in the designation indicate the minimum aluminum percentage. These digits are the same as the two digits to the right of the decimal point in the minimum aluminum percentage when expressed to the nearest 0.01%. The fourth digit indicates the product form. For example, xxx.0 indicates castings, and xxx.1 for the most part indicates ingot having limits for alloying elements the same as those for the alloy in the form of castings. A fourth digit of xxx.2 may be used to indicate that the ingot has composition limits that differ from but fall within the xxx.1 limits; this typically represents the use of tighter limits on certain impurities to achieve specific properties in the cast product produced from that ingot. Table 2.2 shows the cast alloy designation system.

**Table 2.2 Cast Alloy Designation System**

<b>Alloy</b>	<b>Main Alloying Element</b>
1xx.x	Pure aluminum, 99.00% max.
2xx.x	Copper
3xx.x	Silicon, with added copper and/or magnesium
4xx.x	Silicon
5xx.x	Magnesium
7xx.x	Zinc
8xx.x	Tin
9xx.x	Other elements
6xx.x	Unused series

## **2.4 Porosity in Al casting**

Porosity is used to describe voids or cavities that form within a casting during solidification. It is often the cause of poor mechanical properties in rejected casting, including limited strength and ductility, low fracture toughness, irregular crack initiation and propagation characteristics, and lack of pressure tightness [43-45]. Porosity in aluminium casting is caused by the precipitation of air from liquid solution or by shrinkage during solidification. Blow holes, entrapped gas and mold reactions also result in porosity that adversely affects mechanical properties as well as physical acceptability of the cast component. Depending on its origin, porosity in high pressure die casting is usually classified as shrinkage porosity, gas porosity and flow porosity.

The affinity for the generation of shrinkage porosity is related to both the liquid/solid volume fraction at the time of final solidification and the solidification temperature range of the alloy. Due to volumetric differences between liquid and solid states, shrinkage occurs during solidification. Shrinkage porosity is formed when the gate area (from which the molten metal is injected into the die cavity) solidifies before solidification in other areas of the casting is completed (since in this case the passage for molten metal to feed the shrinkage due to solidification is cut off) [46]. Thermal conditions of the die (dictated by its water cooling system, the spray settings, the thermal conductivity of the die material, the cycle time, etc.) and the temperature of the molten metal are the major factors which affect the amount of shrinkage porosity

for a given alloy composition and casting geometry. A typical example of shrinkage porosity is shown in Figure 2.1 (a). Gas porosity is caused mainly by the trapped air, steam and burning products of organic lubricants used in the shot sleeve. Two main features of conventionally produced HPDCs are the extreme turbulence experienced by the molten metal as it is forced at high speed into a die, and the very rapid rate at which it then solidifies [47]. Because of this, castings usually contain internal pores in which gases such as air, hydrogen or vapors formed by the decomposition of organic die wall lubricants are entrapped. An example of gas porosity is shown in Figure 2.1 (b).

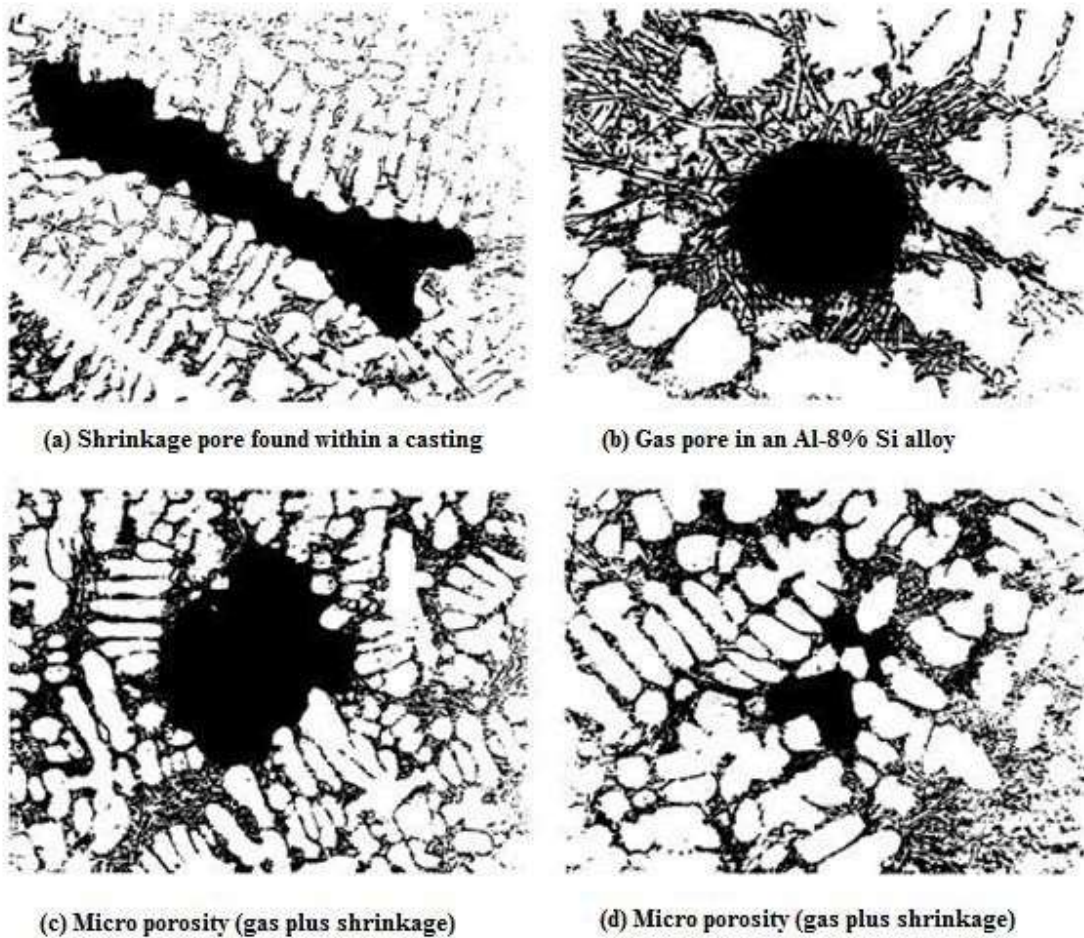


**Figure 2.1 Typical porosity in cast aluminum alloy [48]**

The majority of porosity encountered in casting is due to a combination of gas and shrinkage. Small amounts of dissolved air significantly increase the pore size when shrinkage voids form. These pores generally occur in the inter dendritic regions, which are the last parts of the structure to freeze. Some examples are shown in Figure 2.1 (c) and (d). Flow porosity results from inadequate pressure towards the

end of cavity filling. Numerous factors can affect the porosity levels in a casting. For example, any factors affecting the fluid flow conditions during cavity filling (such as the moving speed of piston in the shot sleeve, the velocity of the molten metal flowing through the gate, geometry and location of the gate for a given casting, pressure applied, etc.) may potentially affect the amount and distribution of entrapped air. Planar defects such as oxide skins and cold shuts may also be present.

## **2.5 Powder Metallurgy Processing**

Powder Metallurgy (P/M) is the science of producing metal powders and making finished or semi-finished objects from mixed or alloyed powders with or without the addition of nonmetallic constituents. P/M parts can be mass produced to net shape or near net shape, eliminating or reducing the need for subsequent machining. P/M processes waste very little material, about 97% of the starting powders are present in the final product. P/M parts can be made with a specified level of porosity, to produce porous metal parts. For example: filters, oil-impregnated bearings and gears. The powder metallurgy process generally consists of four basic steps: powder manufacture, powder blending, compacting and sintering. Compacting is generally performed at room temperature, and the elevated-temperature process of sintering is usually conducted at atmospheric pressure. Optional secondary processing often follows to obtain special properties or enhanced precision.

### **2.5.1 Powder Production**

The chemistry and production of metal powders used in the manufacturing of P/M components have a large influence on the quality of the finished part. Therefore it is essential to select the appropriate starting materials from both economical and performance points of view. There are several methods used to produce metal powders including atomization and mechanical milling as well as chemical techniques based on gaseous and electrolytic reaction practices. Powder fabrication methods such as atomization and mechanical milling methods will be introduced in this section.

Atomization involves the formation of powder from the molten metal stream which is broken into droplets. This technique is used to produce powder of any composition and is by far the most popular commercial method. An important aspect of this technique is the rapid solidification of the powder from the melt. Atomization is attractive for several reasons that include:

1. Particle size can be controlled to a considerable extent.
2. Can be utilized for any metal/alloy that can be melted.

3. Powders with different chemistries can be readily produced.
4. Production rates can approach 400kg/hr.

There are many forms of atomization including gas atomization, water atomization and centrifugal atomization. The main techniques for the production of aluminium powders are water and gas atomization.

In a gas atomization process, the raw material is melted in a crucible and then it is allowed to flow through a small nozzle into a vacuum chamber. The metal stream existing the nozzle is broken up by the rapid expansion of gas, as depicted schematically in Fig. 2.2 [49]. The metal stream falls freely down to the chamber bottom. The expanding gas causes a large depressurization and disruption of the melt stream. Different type of gases is employed but all are either inert ( $N_2$ , He, Ar) or oxidizing (air). For the production of aluminium powder, air is the most commonly used gas, as it is less expensive than an inert gas.

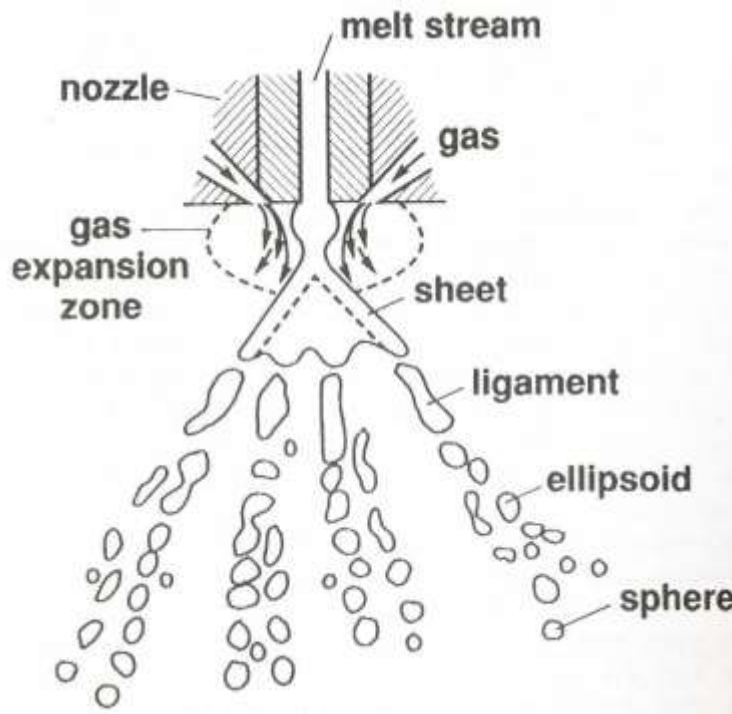


**Figure 2.2 Formation of metal powder by gas atomization near the gas nozzle [49]**

The design of a gas atomization system depends on the metal or alloy being atomized. Possible types of layout include 'horizontal' or 'vertical'. The latter is the more common approach and is generally used for Al, Mg, Ni and Zn. Figure 2.3 shows a schematic diagram of a vertical inert gas atomizer. Horizontal

atomizers are normally used for the production of low melting point powders such as Sn. The resultant powder is typically spherical in shape when an inert gas is utilized, but of a more irregular powder shape when an oxidizing gas such as air is employed. The spherical shape of powder is due to the slow cooling rate and the concomitant ability to form particles with the lowest possible surface energy per unit volume prior to solidification.

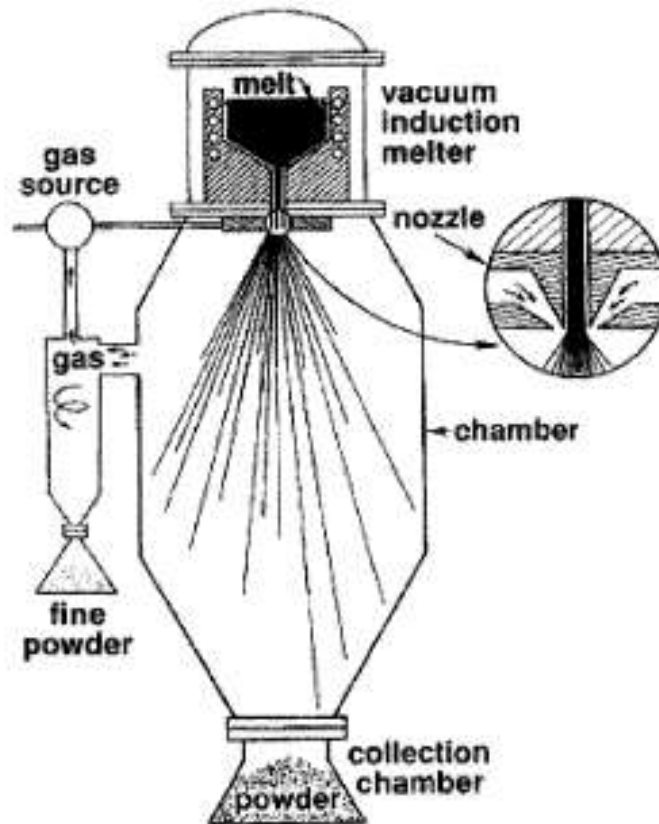


**Figure 2.3 Typical air atomization process**

The main advantage of gas atomization is the product homogeneity, the absence of contamination due to totally inert processing conditions and the spherical shape of the produced powder.

Water atomization is similar to gas atomization but the molten metal stream is disintegrated by water jets (Fig.2.4). Here, the cooling rate is higher than for gas and consequently the chemical segregation into

powder is smaller. The resultant powder shape is more irregular, the powder surface is rougher and more oxidized. A high water velocity causes a decrease in the mean particle size.

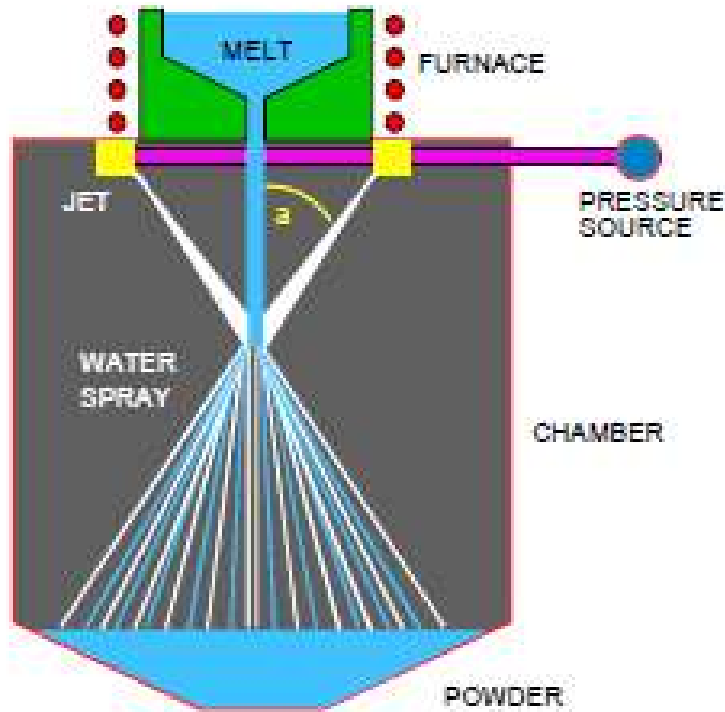


**Figure 2.4 Water atomization process**

Another way of metal powder production is mechanical milling. This method uses a mixture of balls and elemental powder to create a micro alloyed composite powder in an attritor or another high energy ball mill. These powders are normally greater than  $1\mu\text{m}$  in diameter and angular in shape. The processes employed include repeated milling, cold welding, impaction, shearing and compression. This leads to a homogenized material with a uniform dispersion of inclusions. A good balance between milling and welding can be achieved by the proper choice of organic fluids (process controlling agents). Due to heavy cold work, mechanically alloyed powders are not easy to consolidate. Some of the drawbacks associated with this method include extended process time and substantial machinery wear. Because of the nature of the process powder contamination is also problematic and there is a limited control of the particle size

distribution. Figure 2.5 shows the action of a typical jar mill used for mechanical milling of metal powder. The jar is rotated continuously on its side and the repetitious impact of the falling balls grind the materials into powders.

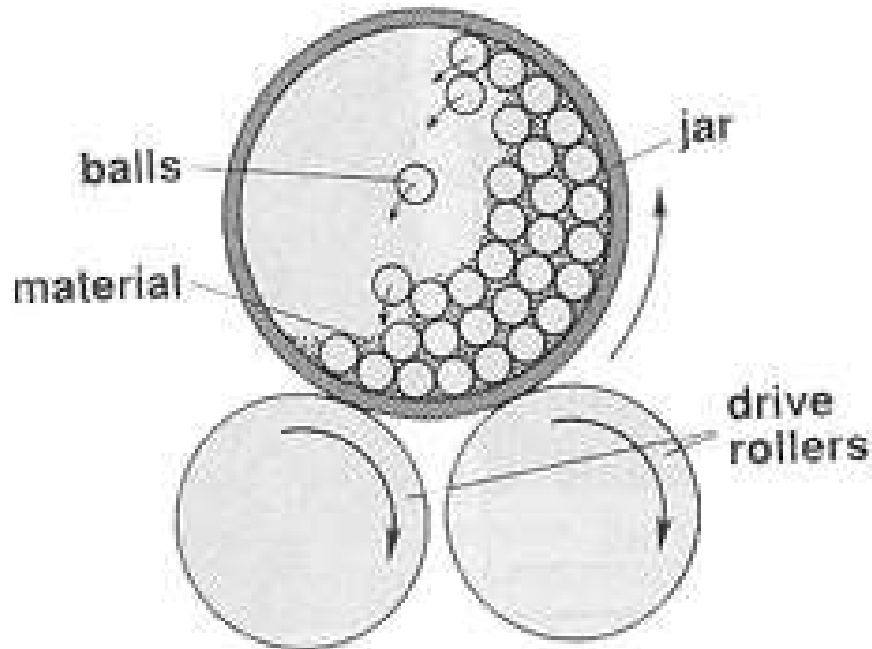


**Figure 2.5 Action of a jar mill**

### **2.5.2 Powder Mixing and Blending**

Generally, the starting material is the mixture of various grades or sizes of powders. Blending and mixing of powders ensure a uniform distribution of different constituents like powders, additives and lubricants. A powder volume of 20 to 40% is the optimum amount of powder that can be mixed at one time [50]. However, this is determined by the type of mixer and the speed at which the mixer is being mixed. These operations are necessary, especially if the application involves a multi-component system. Blending and mixing are often carried out under controlled conditions (inert gas atmosphere or using a liquid medium) to avoid contamination of powder.

Blending is the process in which powders of the same nominal composition but having different particle sizes are integrated. Blending of metal powder is an important treatment and is done: (i) to obtain a

homogenous distribution particle sizes, (powders consisting of different particle sizes are often blended to minimize porosity), and (ii) for intermingling of the lubricant with powders to modify metal-powder interaction during compaction and facilitate the compaction.

Mixing refers to the process of combining powders of different chemistries such as elemental powder mixes or metal-nonmetal powders. In mixing, additives like graphite and lubricants are also used to obtain a homogenous mixture. A mixing operation is a must before compaction of the powders, except in cases where a single elemental powder is to be compacted without the addition of lubricant. In case of mixing of two or more metal powders, particle characteristics like size and distributions play a role in influencing the degree of mixing. This is important because many P/M applications use metal and non-metallic ingredients of different specific gravities, particle size and shape to give optimum properties.

Mixing may be done either in wet or dry condition. Wet mixing is used to produce finer and homogenous mixture of powders. Liquid mediums like alcohol, acetone, benzene or distilled water are used as milling medium in wet milling. Various types of blenders and mills are used for mixing. Rod mills or ball mills are employed extensively for mixing hard metals such as carbides. In general, Y-mixers or double cone mixers are most popular for blending. The use of powder mixing rather than pre-alloyed powders is attributed to both economic and technical issues. Powder mixtures are often less expensive and have better compacting properties. Important factors affecting mixing are: i) type of powders and their characteristics, ii) time of mixing, iii) temperature of mixing and iv) type of mixing (wet or dry mixing). Therefore, mixing must be controlled to produce a homogenous distribution of ingredients having specific particle characteristics.

### **2.5.3 Compaction**

The term “compaction” is used to describe the consolidation of powder particles without the application of heat. This is an important step in powder processing as it enables the forming of loose metal powders into desired shapes with sufficient strength for handling for the subsequent processes. In this process, the powder particles are mainly cold weld or interlocked as illustrated in Fig 2.6 to provide compact strength. Compaction can be performed using a single action or double action approach. In single action, the compact is pressed from one direction, whilst in the latter, compressive forces are applied in two directions. In some cases, isostatic compression is employed where the compact is subjected to

compressive forces from all directions simultaneously. Of the methods available to the industry, those most widely used include die compaction, hot/cold isostatic compaction, direct powder forging and metal injection molding [51-53].

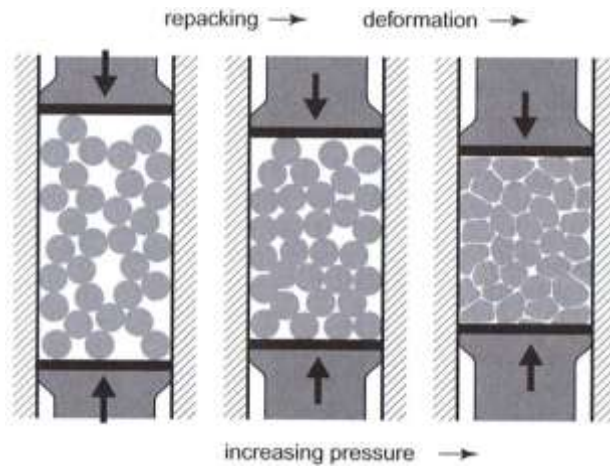


**Figure 2.6 Particle deformation with increasing pressure during uniaxial compaction [54].**

Uniaxial pressing is the most commonly used technique, where the powders are loaded and axially compacted in a hard, rigid die made from tool steel or cemented carbide. Fig.2.7 illustrates the various stages of the uniaxial powder compaction process. Prior to loading the powders, the upper punch is retracted and the lower punch is in fill position. The next step is to load the powders into the die cavity. The lower punch may move down to help uniform powder distribution and loading during filling. Most compactions are performed in this manner so that both the upper and lower punches move. The feed shoe moves back and forth to inject the powder evenly. Both punches are then loaded for generating stress within the powder mass. At the end, the upper punch is removed and the lower punch is used to eject the compact from the die (Fig 2.7). The pressing cycle then repeats with a new fill of powder [54].

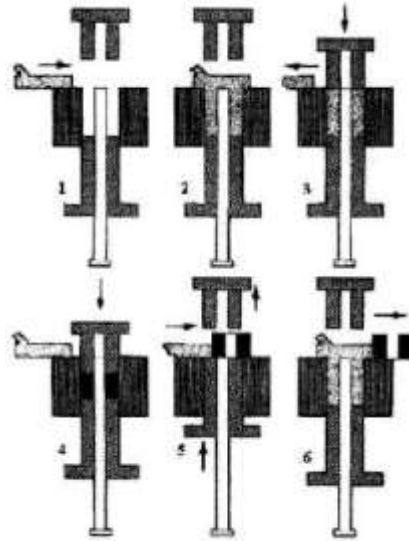


**Figure 2.7 Sequence for die compaction [55]**

The pressure acting during a uniaxial pressing cycle can be divided into three types:

1. Pressure applied directly on the compacting powder (this is assuming that no pressure is lost due to friction of the particles and the die walls, and that there is an even distribution of pressure and density in the compact);
2. Pressure lost due to the friction of particles against the die wall.
3. Pressure created by the uneven distribution of density in various parts of the compacts.

Here, the powder compaction takes place over a few stages (Fig 2.8). In the first stage, a rearrangement of powder particles occurs to fill the larger voids. In the second stage, particles begin to deform on a localized basis at the particle-particle interfaces. Uniform deformation begins in the next stage, where the pores begin to collapse and powders become work hardened. At the final stage of compaction, particles are heavily work hardened and act as a solid, incompressible body. Particles undergo appreciable strain hardening, making it increasingly difficult to compact to a higher density [56]

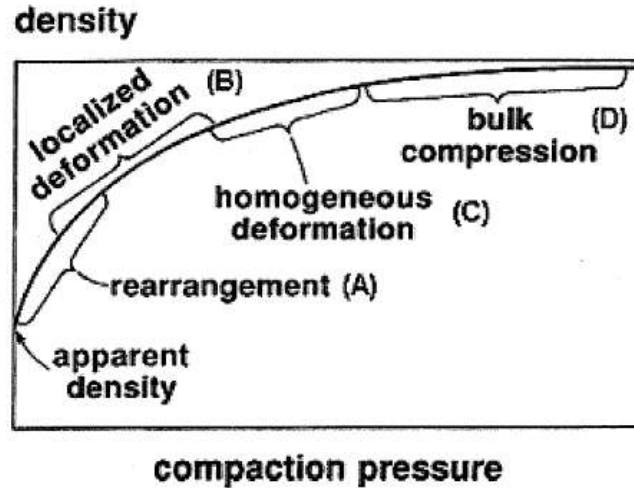


Figure 2.8 A plot of density versus compaction pressure during metal powder compaction.

The largest problem associated with uniaxial die compaction is the occurrence of the die wall friction. Die wall friction causes the applied pressure to decrease with the depth traveled into the powder bed. The consequence of this is that the density of green body is non-uniform. Both single action (pressure applied from one side only) and double action (pressure applied from both sides) compaction experience this type of problem. In the former, the density is greatest near the applied load and decreases as the distance from the load increases. On the other hand, double action compaction causes the density of the green body to be highest at both punch faces and lowest at an intermediate point termed the density split (Fig. 2.9).

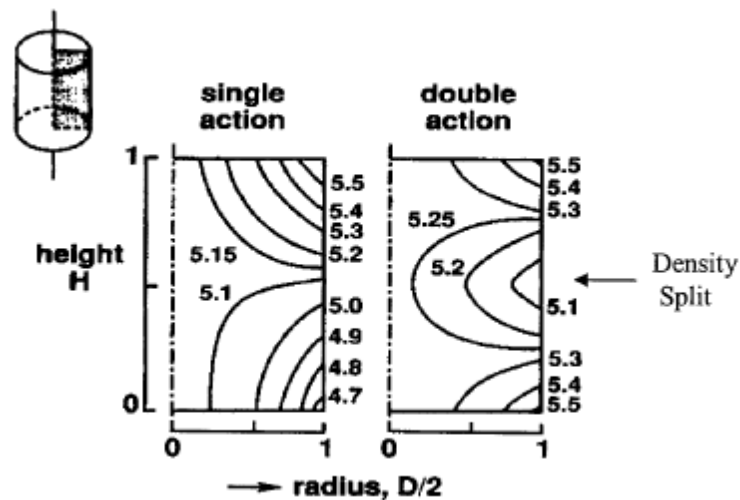


Figure 2.9 Density profile in single action and double action compaction [54]

#### 2.5.4 Sintering

Once green bodies of an appropriate geometry and density have been compacted they are consolidated via thermal energy. Sintering is mainly a thermal process which increases the strength of a powder mass by bonding adjacent particles via diffusion or related atomic level events. This diffusion amongst adjacent powder particles and alloying additions results in the formation of strong inter-particle bonds which improve mechanical properties. To sinter reactive metals such as Al, an essential consideration is the surrounding atmosphere. To avoid any detrimental reactions with oxygen, inert or reducing atmospheres are frequently used [57].

When green bodies are heated compact will reduce its energy by lowering its overall surface area. To accomplish this, a variety of thermally activated mass transport mechanisms are engaged to form necks between adjacent particles. Such mechanisms are divided into two categories: surface-transport and bulk transport. Surface transport involves the migration of atoms from the central mass of a particle to a surface. Bulk transport mechanisms include volume diffusion, grain boundary diffusion, plastic flow and viscous flow.

From a practical perspective, the two most significant factors in sintering are sintering time and temperature; the latter is regarded as the most important variable. Compact porosity, particle size and powder type (elemental or master alloy) also influence sintering response. The majority of P/M materials are sintered in a solid state manner at approximately 0.6 to 0.8 of the absolute melting point of the material. While sintering proceeds, the microstructure changes considerably as the temperature is increased and the time is prolonged. The associated evolution sequence can be broken down into 3 key stages - initial, intermediate and final.

The initial stage is primarily focused on the growth of sinter bonds (necks) that form between the contacts that exist in green compacts. Although all mass transport mechanisms are involved at this stage, those of most importance are the lower temperature mechanisms of evaporation-condensation and surface diffusion. Vapor flows into the neck, due to the vapor pressure differential that exists, and atoms diffuse to the neck in response to the locally high concentration of vacancies that exist. An important gauge in assessing the

stage or degree of sintering is the extent to which the pores are rounded and their respective size. In the initial stage, the porosity is quite coarse and shows only slight rounding as shown in Figure 2.10 (a). The strength of a sintered product in this condition will be very low and is said to be “under sintered”.

The intermediate stage is the most important of the three as it governs the extent of densification and largely determines the properties of the sintered product. This stage is characterized by simultaneous pore rounding, densification and grain growth (Figure 2.10 (b)). Since the curvature gradients are largely eliminated during the initial stage of sintering, the driving force for continued sintering becomes the elimination of surface area energy through changes in the pore structure. At this stage, the pores can be thought of as cylindrically-shaped regions with a high concentration of vacancies. Consequently, vacancies diffuse away from pores, while a corresponding flux of atoms (mass) flows into them. This reduces the amount of porosity and surface area contained within the compact and is manifested as densification. The cylindrical pores eventually pinch-off into smaller, highly rounded pores that are located at grain boundary intersections. At this point, the third “final stage” of sintering begins.

When compared to the initial and intermediate stages of sintering, the final stage is a very slow process. It is rarely attained in commercial applications for P/M. The final stage of sintering commences when closed, highly rounded pores exist at grain boundary intersections. The driving force for continued densification in the final stage is exclusively the reduction of surface area and surface energy. When much of the surface area is eliminated in the preceding stages, the relative magnitude of the driving force has diminished greatly. In order to attain further improvements in densification and strength during this stage the interaction between grain boundaries and porosity must be examined.

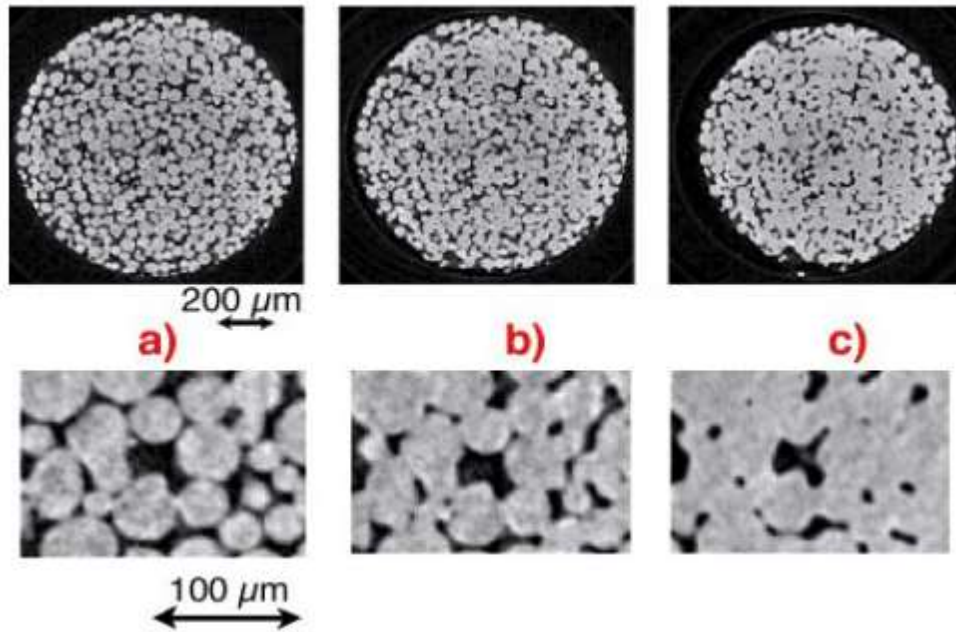


**Figure 2.10 Different stages of sintering, (a) initial stage, (b) intermediate stage, (c) final stage**

The presence of pores is common in the P/M process. Pores are bound to grain boundaries because they lower the grain boundary area and therefore, the overall free energy of the sintered compact. As the sintering process continues, the porosity and the binding energy of the pore-to-grain boundary diminish. Under this condition, the pores can eventually break free from grain boundaries by two mechanisms. One possibility is attributed to increased grain boundary mobility. This occurs at higher sintering temperatures and longer sintering times such that the grain boundaries move faster than the pores and eventually break free (Figure 2.11). A second possibility is Ostwald ripening. In essence, this means that large pores will grow at the expense of smaller ones. For this to occur at an appreciable rate, the pores must lie along grain boundaries which act as paths for rapid diffusion. However, if the grains grow too quickly the pores will become separated from the grain boundaries. From a practical perspective, once pores break away from grain boundaries by either mechanism, densification stops at this point. An example of a microstructure that can be reached in the final stage of sintering is presented in Figure 2.10 (c).

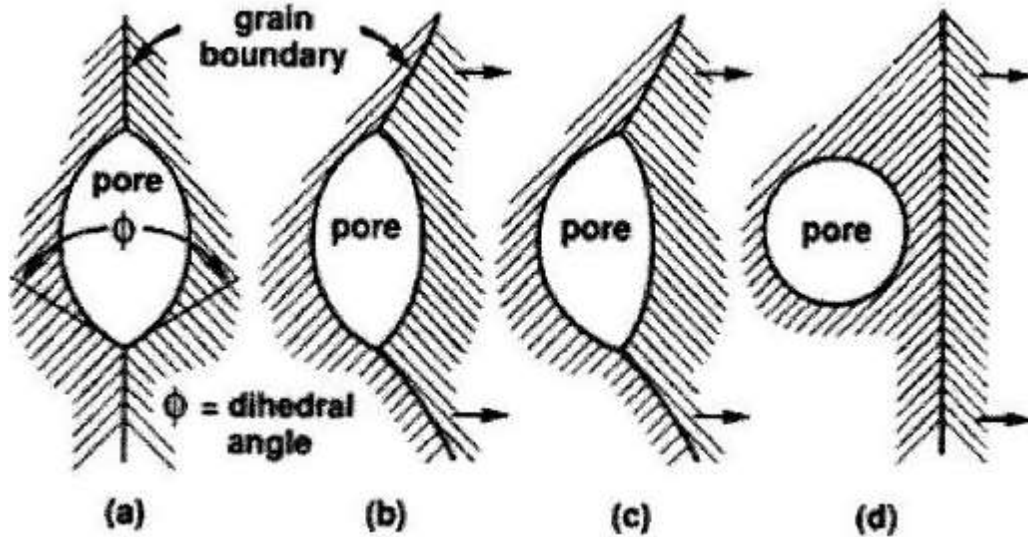


**Figure 2.11** The sequence of steps leading to pore isolation and spheroidization in the final stage of sintering via grain boundary mobility [58].

## 2.6 Cold Isostatic Pressing

CIP is a compaction method in which isostatic compression is introduced to a body of loose powder by using pressurized liquid. Isostatic compression is possible as described by Pascal's Law, which states that pressure can be transmitted equally and in all directions through gas or liquid such that the pressure variations (initial differences) remain the same. With applying sufficient liquid pressure, the concentration of porosity within the loose powder can be reduced and in turn, the density of the green compact can be increased. Generally, a liquid pressure is chosen such that the yield stress of the material is exceeded. A typical Cold Isostatic Pressing system is shown in Figure 2.12.

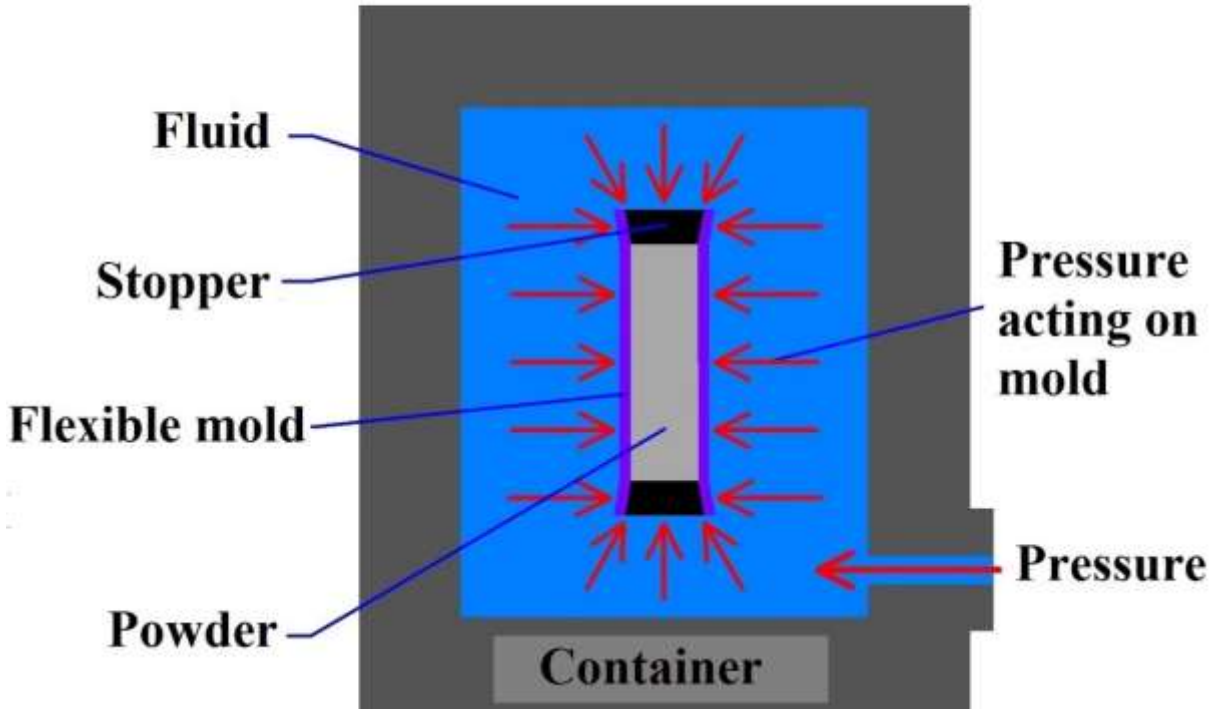


**Figure 2.12 Cold isostatic pressing system**

CIP has certain advantages over die compaction. First of all, as there is no rigid die, the use of lubricant to reduce die wall friction is not needed. As lubricant is a contaminant that tends to be detrimental for mechanical properties, its exclusion is a benefit. Another positive aspect of CIP is the ability to make large complex parts, which can be essential in some scenarios. This is not possible with conventional die compaction due to press capacity limitations.

### **2.7 Porosity in Al Powder Metallurgy**

After sintering, voids may still be left within the compact. Porosity is the fraction of voids left in the total compact volume. It may be measured by finding the weight and dimensions of the compact and comparing the density calculated from these values to the theoretical maximum. Generally, a high density compact that has as low porosity as possible is desired in order to attain peak mechanical properties. Even at very low concentrations, residual porosity can still impart a negative effect overall.

Knowledge of the bulk porosity value alone is not enough to understand the ultimate impact of porosity on mechanical properties. In this regard, the pore structure such as size, shape, and level of connectivity can also play a vital role. For example, a compact that has one very large pore may fail whereas another compact with an equal volume of porosity, but with many more very small pores, may not. Moreover, increased irregularity of the pore shape invokes the opposite behavior. Porosity has a particularly detrimental effect on impact, fracture, and fatigue behavior. Fatigue crack initiation is thought to be directly linked to the residual porosity in PM specimens, as pores act as stress concentrators. Kim et al. observed that in many cases, the fatigue crack initiation site was that of a single subsurface pore [59].

## **2.8 Wear**

Wear is the surface damage or removal of the material from one or both of two solid surfaces in a sliding, rolling or impact motion relative to one another. In most of the cases, wear occurs through surface interactions at asperities. During relative motion, first material on the contacting surface may be displaced so that properties of the solid body, at least at or near the surface are altered. Such a process is complicated, involving time-dependent deformation, failure and removal of materials at the counterface. The wear process is actually common in machines with or without the presence of lubricant.

## **2.9 Mechanism of Wear**

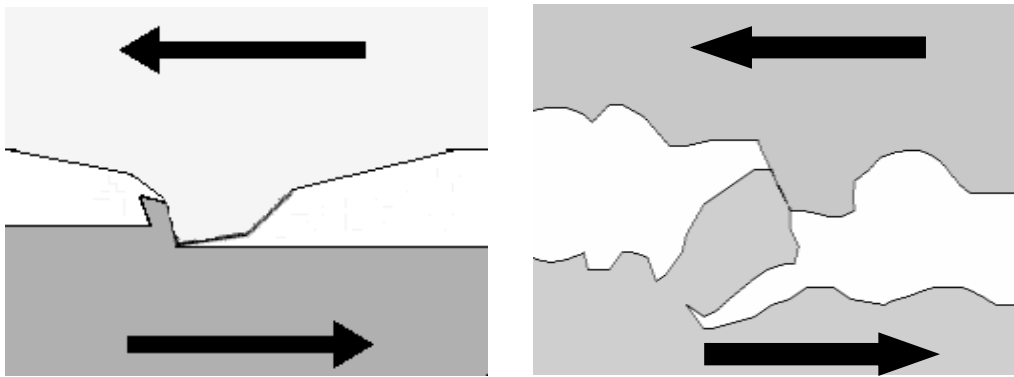
The wear processes can also be explained in terms of a “tribosystem,” which includes a solid body, a counter-body, an interfacial element and the environment. The overall interaction between the different parameters in the tribosystems will lead to different wear types [60-64]. There are many operative wear mechanisms, but the most common mechanisms of wear include abrasion, adhesion, surface fatigue, erosion and delamination. Detailed descriptions of the wear mechanisms are outlined in the following section.

### **2.9.1 Abrasive Wear**

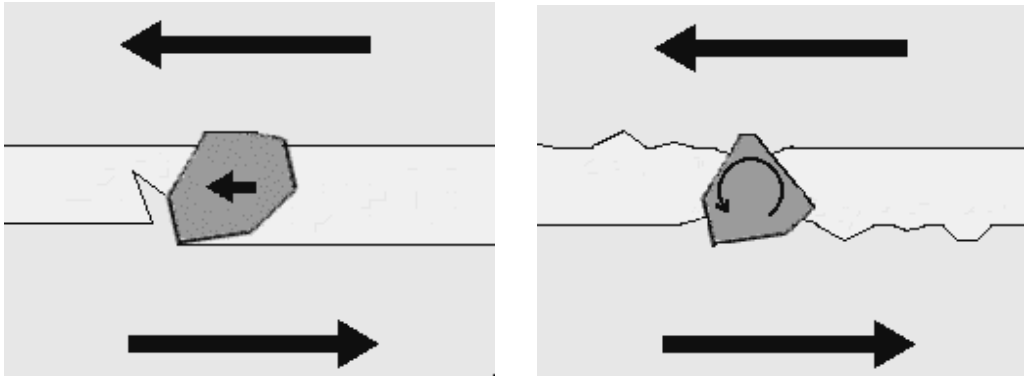
Abrasive wear occurs when material is removed from one surface by another harder material, leaving hard particles of debris between the two surfaces. It can also be called scratching, gouging or scoring depending on the severity of wear.

Abrasive wear has been reported to account for at least 50% of wear problems that are encountered in industry today. It is mostly experienced when hard particles such as rocks or metal fragments slide or roll under pressure across a surface, potentially leading to cutting of grooves in a similar manner to a cutting tool, displacing elongated chips or slivers of metal [65]. Abrasion is categorized according to the types of contacts as well as contact environment [66]. Depending on the way the asperities pass over the worn surfaces, abrasive wear modes could be two-body or three-body.

Two body abrasive wear occurs when one surface (usually harder than the second) cuts material away from the second. It occurs in a similar fashion to mechanical operations such as machining, grinding and cutting. On the other hand, a three body abrasive wear mode is observed when a third body generally a small particle of grit or abrasive, lodges between the two surfaces, abrades one or both of these surfaces. In terms of comparison between two-body and three-body abrasive wear modes, two-body wear is faster than three-body. Three-body wear is almost ten times slower than two-body abrasive wear, since it has to compete with the other mechanisms that are taking place [67-70]. Secondly, two-body abrasive wear occurs in a similar fashion to mechanical operations such as machining, grinding and cutting, while in three-body abrasive wear, slower mechanisms of material removal is involved.



Two-body abrasion



Three-body abrasion

**Figure 2.13 Abrasive wear**

Many mechanisms have been proposed to explain how material is removed during abrasion. These mechanisms include fracture, fatigue, and melting. Due to the complexity of the abrasion process, no single mechanism completely accounts for all the loss [71]. They include ploughing, wedge formation, cutting, microfatigue and microcracking [72-73].

Ploughing results in a series of grooves as a result of the plastic flow of the softer material. In this process, material is displaced from a groove into the sides without removal of material. This process causes surface and subsurface cracks.

When an abrasive tip ploughs a groove, it develops a wedge on its front. It generally occurs when the ratio of shear strength of the interface relative to the shear strength of the bulk is high. In this process, only some of the material displaced from the groove is displaced to the sides and the remaining material shows up as a wedge. In the cutting form of abrasive wear, an abrasive tip with large attack angle ploughs a groove and removes the material in the form of discontinuous or ribbon-shaped debris particles similar to that produced in a metal cutting operation. This process results in significant removal of material and the displaced material relative to the size of the groove is very little. During cutting operations, the hard particle is embedded in the softer material and dragged, potentially leading to intense plastic deformation and material displacement around the edge of the hard particles. Microcracking is a mechanism that removes material from a brittle specimen. Microfatigue is when the abrading mediums continuously slide on the specimen and occasionally causes deformation. [74-75].

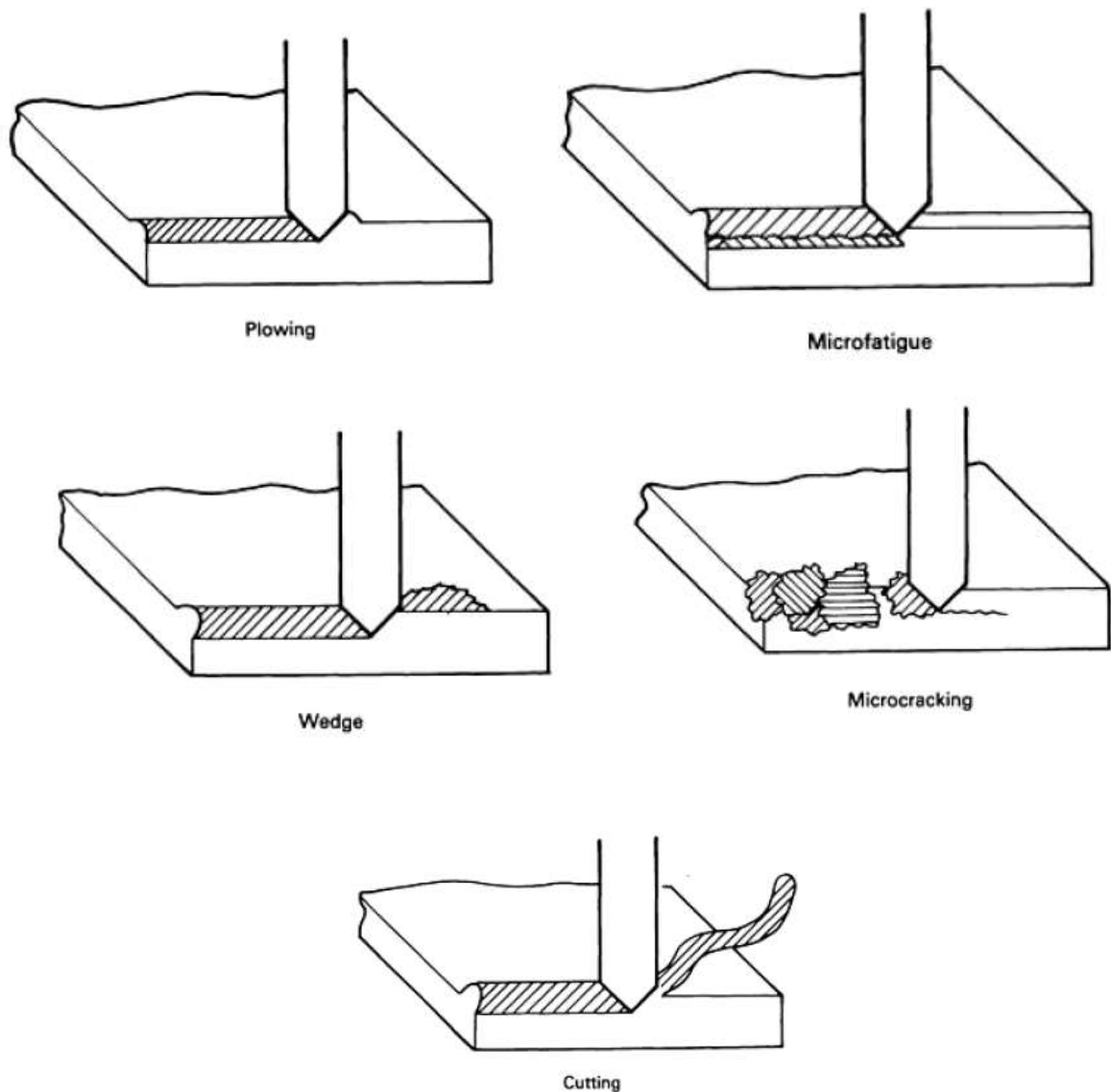


**Figure 2.14 Different abrasion mechanism**

### 2.9.2 Adhesive Wear

Adhesion wear occurs when two solid surfaces are in sliding or in rolling contact with each other. It is often called galling or scuffing, where tips of the highest asperities lock together as two surfaces slide across each other under pressure. It is assumed that, these asperities welded together, deformed plastically by high local pressure and form asperity junctions [76-78]. This sharing results in detachment of a fragment from one surface and attachment to the other surface (Figure 2.15). As the sliding process continues, the transferred fragments may eventually come off the surface on which they are transferred

and be transferred back to the original surface, or they could potentially form loose wear particles. Moreover, some of these transferred fragments could be fractured by fatigue as a result of repeated loading and unloading action resulting in formation of loose particles or wear debris.

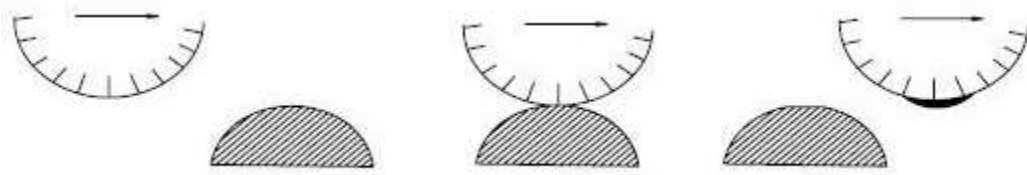


**Figure 2.15 Schematic representation of adhesive wear**

If the initial condition is boundary lubrication (only tribochemical wear), a transition to adhesive wear may take place. Under conditions of increased contact severity, protective surface layers will not withstand and metal metal contact will occur. First, with increasing normal force or sliding velocity, mild material transfer will take place at a microscopic scale. This condition is called incipient or micro scuffing. At even more serious conditions, severe adhesion wear will occur. This condition is commonly referred to as scuffing.

Adhesive wear can be explained by Archard’s law of wear [79].

$$W = K \frac{F_N}{H_S}$$

Where,  $W$  is the volume worn per unit sliding distance,  $F_N$  is the applied load,  $H_S$  is the hardness of the softer materials in contact and  $K$  is the wear coefficient. Moreover, the adhesion component of friction is due to the formation and rupture of interfacial bonds. These bonds are the result of interfacial interatomic forces developing between two surfaces in contact. If sliding is to take place, a friction force is needed to shear the weakest tangential planes at the area of contact.

### 2.9.3 Surface Fatigue

The term ‘fatigue’ is broadly applied to the failure phenomenon where a solid is subjected to cyclic loading involving tension and compression above a certain critical stress. Due to repeated loading and unloading cyclic stresses surface and subsurface cracks are generated which lead to failure of the component. These

cracks initiate from the point where the shear stress is maximum, and propagate to the surface as shown in Figure 2.16. Once the crack reaches the critical size, it changes its direction to emerge at the surface. After repeated stress by the bearing load, these cracks spread even without additional particulate damage and eventually the surface fails, producing a spall. In this phenomenon, wear is mainly determined by the mechanics of crack initiation, crack growth and fracture. This process can occur only in systems where abrasive and adhesive wear are not present, such as in systems with high surface contact loads. Erosion, fretting and cavitations are typical examples of fatigue failure. Bearing surfaces are subjected to this type of wear as a result of repeated stress caused by particles trapped between two moving surfaces [80]. Vibration is a common cause of fatigue wear.

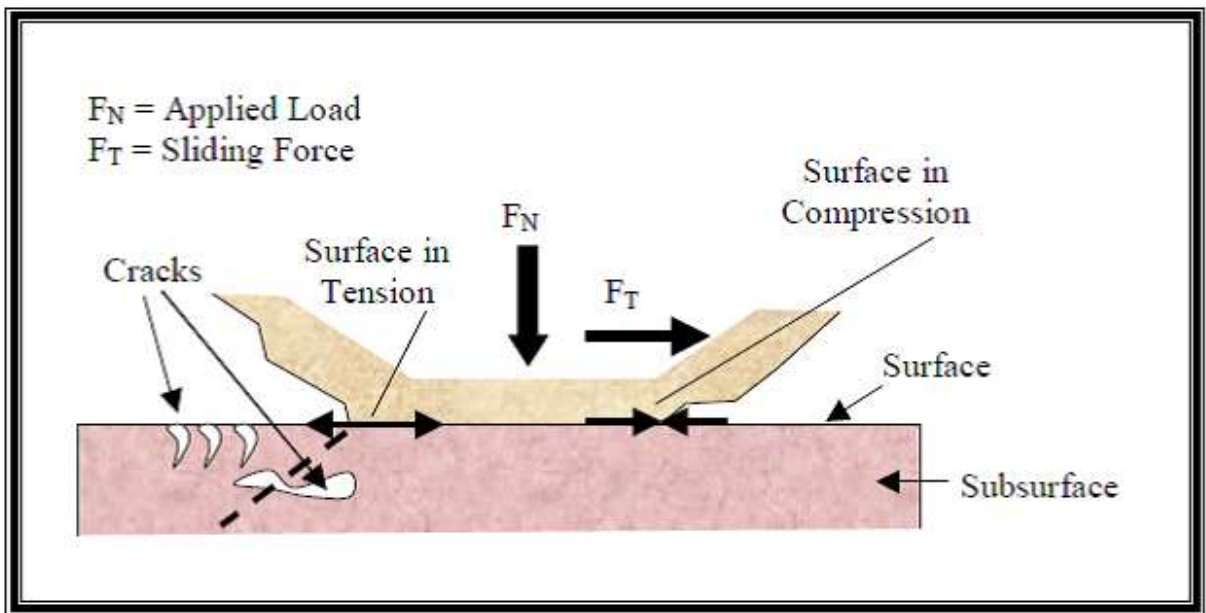


**Figure 2.16 Schematic of fatigue wear due to formation of surface and subsurface cracks**

#### 2.9.4 Erosive Wear

Erosive wear can be defined as the process of metal removal due to impingement of solid particles, small drops of liquid or gas on a surface. Solid particle impact erosion has been receiving increasing attention, especially in the aerospace industry [81]. Examples include the ingestion of sand and erosion of jet engines and of helicopter blades. As shown in Figure 2.17, the erosion mechanism is simple. Solid particle erosion is a result of the impact of a solid particle A, with the solid surface B, resulting in part of the surface B

been removed. The impinging particle may vary in composition as well as in form. The response of engineering materials to the impingement of solid particles or liquid drops varies greatly depending on the class of material, materials properties (dependent on thermal history, exposure to previous stresses or surface tensions) and the environmental parameters associated with the erosion process, such as impact velocity, impact angle, and particle size / type. Movement of the particle stream relative to the surface and angle of impingement both have a significant effect on the rate of material removal [82]. The erosive effects on materials at high temperatures is important for the selection of turbine engine materials in the aerospace industry [83]. Cavitation erosion occurs when a solid and a fluid are in relative motion, due to the fluid becoming unstable and bubbling up and imploding against the surface of the solid, as shown in Figure 2.18. Cavitation damage generally occurs in fluid-handling machines such as marine propellers, hydrofoils, dam slipways, gates and all other hydraulic turbines. Cavitation erosion roughens a surface much like an etchant would.

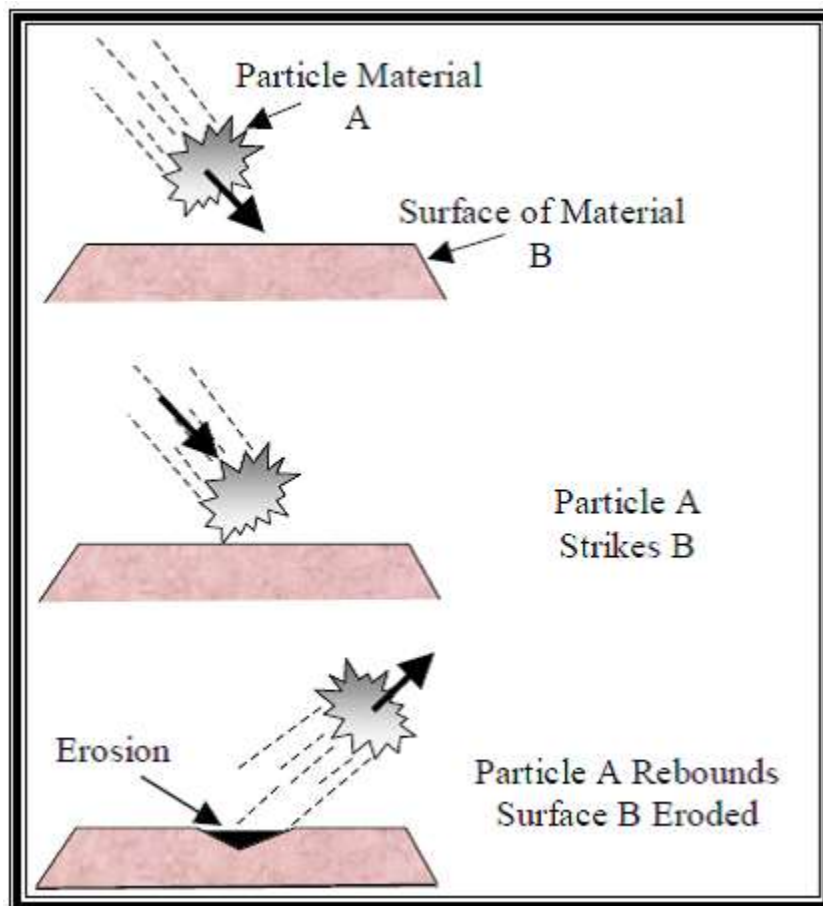


**Figure 2.17 Schematic of erosive wear**

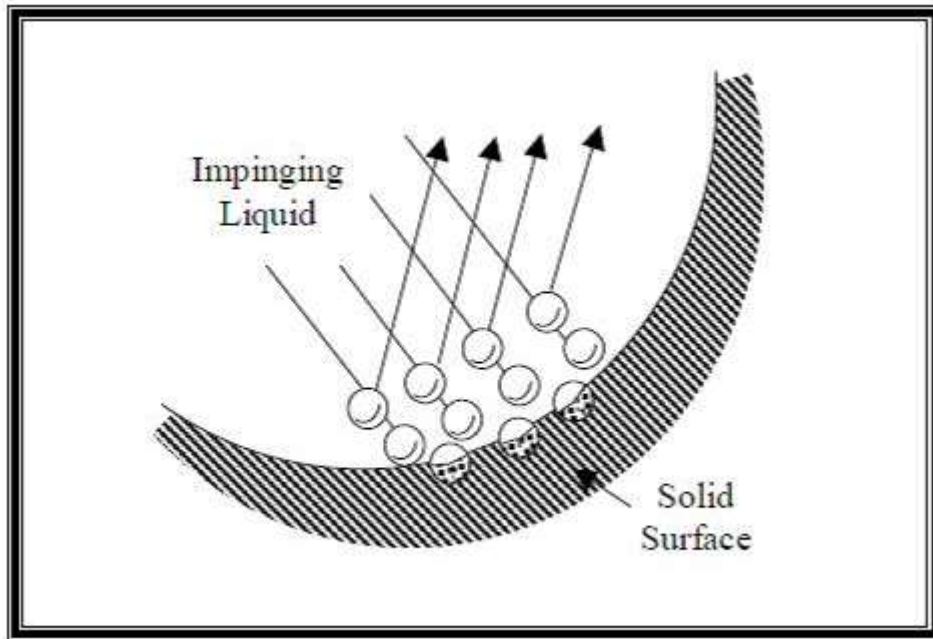


**Figure 2.18 Schematic of cavitation erosion due to impingement of liquid bubbles**

The distinction between erosion and abrasion should be clarified, because the term erosion has often been used in connection with situations that might be better classed as abrasion. Solid particle erosion refers to a series of particles striking and rebounding from the surface, while abrasion results from the sliding of abrasive particles across a surface under the action of an externally applied force. The clearest distinction is that, in erosion, the force exerted by the particles on the material is due to their deceleration, while in abrasion it is externally applied and approximately constant [84].

### **2.9.5 Fretting Wear**

Fretting occurs when two contacting surfaces rub during low amplitude oscillatory motion. The motion is usually the result of external vibration, but in many cases, it is the consequence of one of the members of the contact being subjected to a cyclic stress (that is, fatigue), which gives rise to another and usually more damaging aspect of fretting, namely the early initiation of fatigue cracks. This is termed as "fretting fatigue" or "contact fatigue." Fatigue cracks can be initiated where the contacting surfaces are under a heavy normal load or where there is a static tensile stress in one of the surfaces [85]. Although fretting

does not cause rapid loss of material, it generally occurs in situations where no wear is anticipated and, as a result, can initiate serious damage and failure. For example, flywheels that are force-fit onto crankshafts will sometimes fret, with the loss of material eventually causing the wheel to loosen on the shaft. The fretting process induces surface defects, which, under cyclic loading, reduces the fatigue life and strength of a part. Thus, a part designed for safe life under known fatigue loading can fail if exposed to fretting. Fatigue failure of turbine blades at the point of attachment to the wheel is the most common example of fretting fatigue. The contact fatigue process that results in pitting involves the high contact stress field developed during rolling contact. This stress field interacts with surface and subsurface defects and hard inclusions to initiate cracking. The cracks propagate below the surface and finally turn and emerge at the surface, producing a pit.

### **2.9.6 Delamination**

Delamination is a process of wear, that is based on the concept of accumulation of near surface plastic strain. The delamination theory of sliding wear was first proposed by Suh [86] in 1973 to explain observations of thin flake-like wear particles. The theory is based on the behavior of dislocations at the surface, sub-surface crack and void formation, and subsequent joining of cracks by shear deformation of the surface. His concept stimulated a great deal of research, which has resulted in changes to and further updates of the theory [87]. The formation of loose wear sheets is described by the following sequence. In the early stages of sliding a relatively smooth surface is initiated by the fracture or deformation of initial surface asperities. The surface traction acting at the contact points induces incremental plastic deformation which accumulates with repeated loading. As the subsurface deformation continues, cracks nucleate below the surface and propagate parallel to the surface. Finally the cracks shear to the surface and a long thin wear sheet delaminates.

Three mechanisms are associated with delamination theory. There is the initial asperity deformation and fracture, which is associated with the “running-in” of sliding surfaces. Suh stated that asperity interactions would also occur in the steady-state, since asperities will be generated by the uneven delamination of wear sheets. However, the wear particles formed will be much smaller than the sheet-like particles formed by the delamination process. Hence the delamination mechanisms of crack nucleation and propagation will control the steady-state wear process. In materials with pre-existing cracks or in which cracks readily nucleate, crack propagation will determine the wear rate. Conversely, in materials with rapid crack

propagation rates, crack nucleation will be the wear rate determining mechanism. Fracture mechanics treatments of crack nucleation and propagation have produced analytical models of these two mechanisms.

Suh showed that for microstructures containing second-phase particles, if sufficient plastic deformation occurred during sliding wear, crack nucleation was favoured by these particles. In this situation, inter-particle spacing is an important variable that controlled the wear rate. Void formation is primarily attributed to plastic flow of the matrix around these hard particles. Void formation occurred very readily around the hard particles but crack propagation occurs very slowly. The depth at which the void nucleation was initiated and the void size tended to increase with increased friction coefficient and applied load. The material which delaminates is not merely the deformed base material but instead a mechanically mixed layer of transfer material, which can include material from both sliding surfaces as well as the sliding environment, such as oxygen [88]. The transfer layer resides on the surface and is composed of fine particulate matter produced by asperity adhesion and wear debris.

Delamination wear, in which subsurface cracks propagate to the surface, is not observed in pure metals and simple alloys like bronze and carbon steel. Its occurrence is more likely in hardened alloys containing hard, non-metallic inclusions.

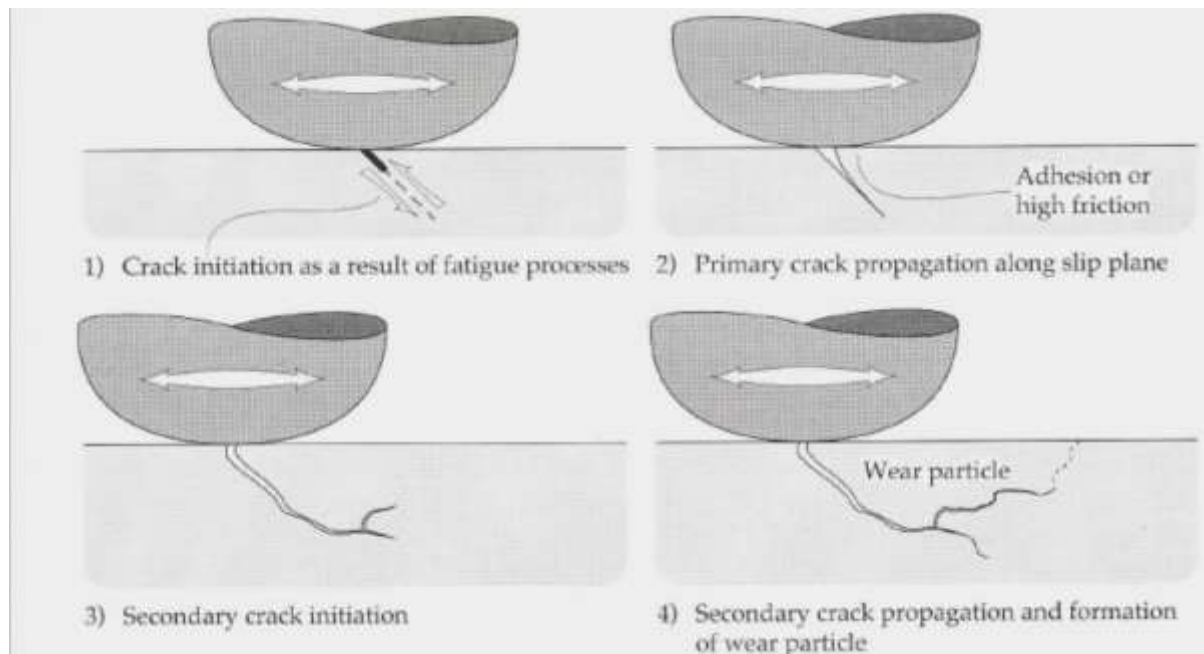


**Figure 2.19 Delamination wear**

## 2.10 Wear Behavior of Aluminium

The dominant factors that affect the sliding wear behavior of aluminium include: sliding distance, sliding speed, applied load, atmospheric condition, etc. [89]. Some other intrinsic factors such as reinforcement type, shape, size, volume fraction and distribution, interface between the reinforcement particles and matrix, porosity also affect the sliding wear behavior of aluminium [90]. A strong interaction between normal load and sliding speed in causing the wear of a material was clearly demonstrated by Wilson and Alpas [91]. Increase in wear rate with an increase in normal load and sliding speed has been investigated by several researchers [92-94]. Wear of aluminium occurs by several mechanisms such as oxidation-dominated wear, abrasive wear, adhesive wear, delamination, melt lubrication wear and seizure. At very low sliding speeds and loads an oxidative mechanism can control the wear process. At relatively higher speed, metal-metal contact leads to severe wear when the surface temperature of the contact area exceeds the recrystallization temperature of the material [95]. Damage accumulation and plastic deformation below contact surfaces play an important role in sliding wear of ductile materials and wear rate depends on the properties of the generated skin rather than the original materials [96-97].

Subramanian (1991) [98] suggested that the wear rate of Al-Si alloy decreases with an increase in sliding speed. He observed the decreasing trend of wear rate to a reduction in the number and size of the transferred fragments. Jasim et al. (1993) [99] found that the depth of the subsurface damage decreases with increase in sliding speed, indicating that the decrease in wear rate is a consequence of shallower subsurface damage as sliding speed increases. Archard and Hirst (1957) [100,101] suggested that a mild wear process can be divided into three different stages. In the early stage, as the surfaces first rub together, the load is borne by a relatively small number of contact areas and wear occurs by the transfer of materials to the counter-face. As the experiment continues, the surfaces in contact achieve greater conformity, and the load becomes supported by a larger number of contact areas. In the final stage, most of the load is borne by the loose wear debris and an increase in wear rate is observed due to the abrasion of the surfaces by these particles. Other researchers have observed that wear rate initially decreases and then increases as sliding speed is steadily increased [102]. It is relevant to point out that wear resistance depends not only on the properties of the materials involved but also on the geometry of the contact [103]. Strain hardening may also play an important role since the density of dislocations would increase during wear, which could influence the hardness and thus wear resistance.

## 2.11 Wear Regime Maps in Al-Si Alloys

When observing the wear behavior of Al-Si alloys, it is evident that different regimes occur based on varying sliding conditions. Lim and Ashby (1987) [104] constructed the first wear mechanism maps (Figure 2.20) based on physical modeling in order to systematize empirical wear data on steels. These maps allowed to predict the dominant wear mechanisms under a given set of test conditions in terms of a few key dimensionless parameters. Liu et al. [105] compiled various experimental results to develop a physical model similar to what was initially developed by Lim and Ashby [104]. By modifying the models, an empirical wear map for Al-Si alloy was generated as shown in Figure 2.21. The significance of the particular map is that allows for a broad presentation of the different wear regimes and mechanisms which exist for a given condition. It is essential to realize that within each regime, the dominant wear mechanism is different and can be altered by varying parameters such as speed, load and atmospheric conditions.

Using wear map principles, Zhang and Alpas [106] investigated the working mechanism of delamination wear by conducting dry sliding wear tests on Al-7% Si alloy; this is particularly important for determining the stress and strain distributions as a function of sliding distance and applied loads. The authors reported that both the magnitude of the strains and the depth of the deformed zones increase with sliding distance and applied load. By applying the Voce equation, the strain hardening of the material was calculated and is illustrated to show that hardening capacity of the material was exhausted and exponentially decreased towards the contacting surface when moved further away from the surface. Void nucleation sites initiated at Al-Si interfaces and linked together to form subsurface cracks below the surface as shown in Figure 2.22. When the subsurface cracks reach the surface, delamination of the material occurred. Zhang and Alpas [107] continued to study the transition point from one regime to another on Al-Si (6061) by changing the load, sliding velocity, and sliding distance, allowing the understanding of how each condition effects the transition point. They suggested that wear rates were mild at low loads and increased gradually until the material experienced a transition from mild to severe wear. Transition from mild to severe wear was observed when the bulk surface temperature exceeded a critical temperature limit when the load or sliding speeds were increased. The temperature increase affects the hardness of the matrix, which was made evident by the recrystallization of the matrix. This indicated that the transition point was not a single influencing factor but a combination of systems acting together. The most commonly reported wear

regimes for an Al-Si system in contact with a steel counterface are mild wear (MW) and severe wear (SW).

Figure 2.23 shows a wear rate versus load map for an Al-Si binary system and various Al-Si systems with Cu, Fe, and Ni as the alloying elements [108]. The binary Al-Si system contains a transition point at 30N where the regime changes from mild wear to severe wear. This transition indicates a change in the mechanisms. Alloying with 2% Cu increased the transition point from 30N to 80N and similarly when Ni and Fe were added, the transition point increased slightly. Yen and Ishihara [109] and Goto et al. [110] suggested that testing conditions such as humidity, atmosphere, and counterface materials were factors which can all change the tribological behavior of any system under observation. An important observation was made by Elmadagli et al. [111] when studying the sliding behavior of Al-18.5%Si, Al-8% Si, and Al-25% Si in a controlled dry environment containing 5% relative humidity. The authors described that the transition from mild to severe wear exists for all the alloys tested; however, two new sub-regions of wear were observed. The state of ultra-mild wear (UMW) was observed when loads of 10N were used during contact with 52100 bearing steel counterface in an argon atmosphere. When the counterface was changed to a diamond like carbon (DLC)-coated steel counterface running in dry air (RH 5%) atmosphere, the same condition of UMW was achieved.

Antoniou and Subramanian (1988) [112] developed a qualitative map to present wear data on aluminum and its alloys, as shown in Figure 2.24. Within the wear mechanism map for aluminum alloys five wear mechanisms have been identified by Antoniou. The method of identification relies heavily on the topography and microstructure of the wear debris and associated worn surface. These five mechanisms are: (a) formation of fine equiaxed particles, (b) delamination of compacted equiaxed particles, (c) delamination of deformed aluminum alloy, (d) gross material transfer and (e) melt wear.

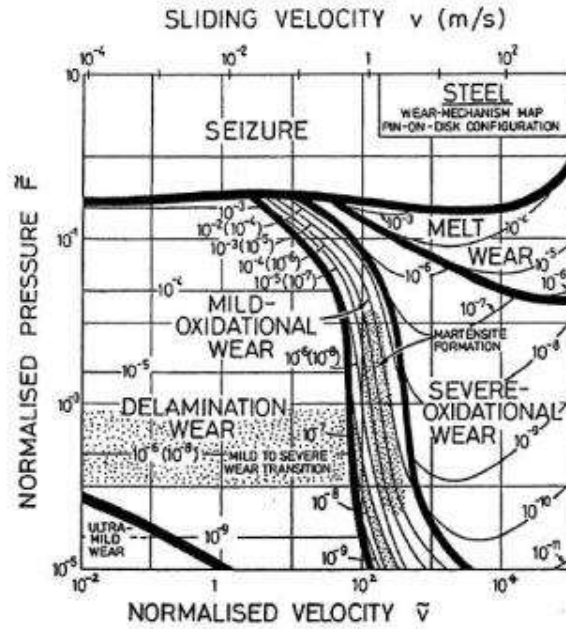


Figure 2.20 Wear map for steel-on-steel during dry sliding [89]

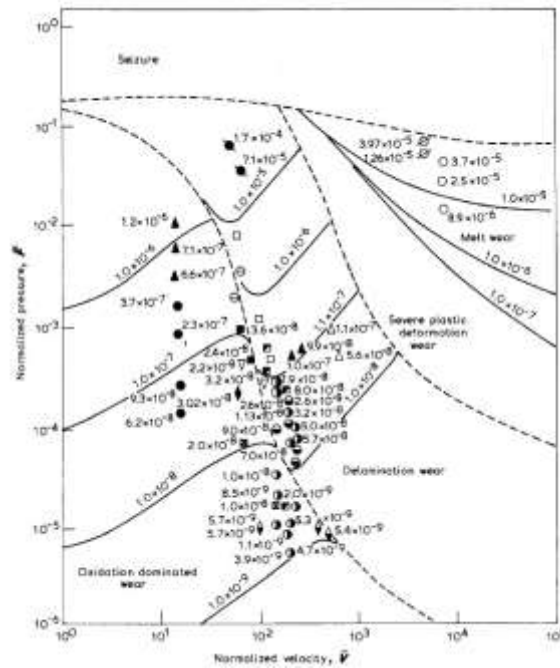


Figure 2.21 Wear map of aluminum alloy outlining the boundaries for each wear mechanism [90]

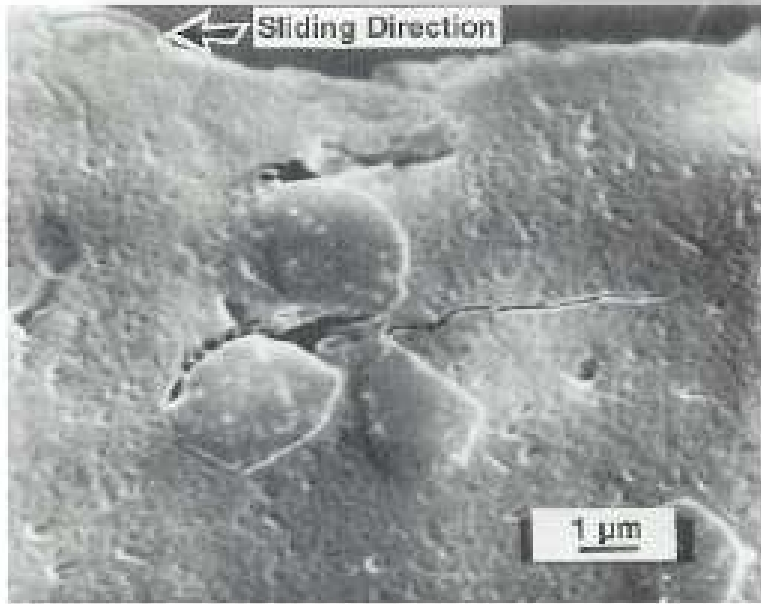


Figure 2.22 Void and crack nucleation around the silicon particles under the contact surface

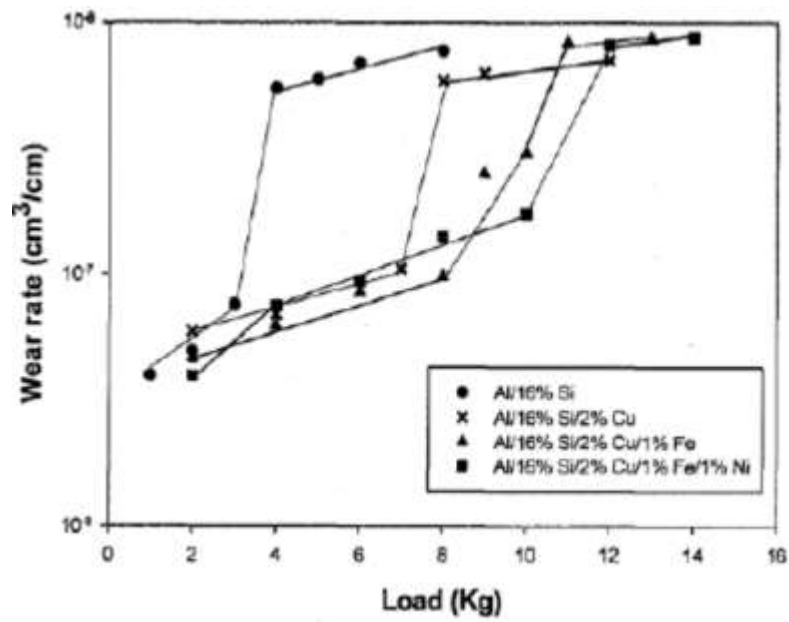
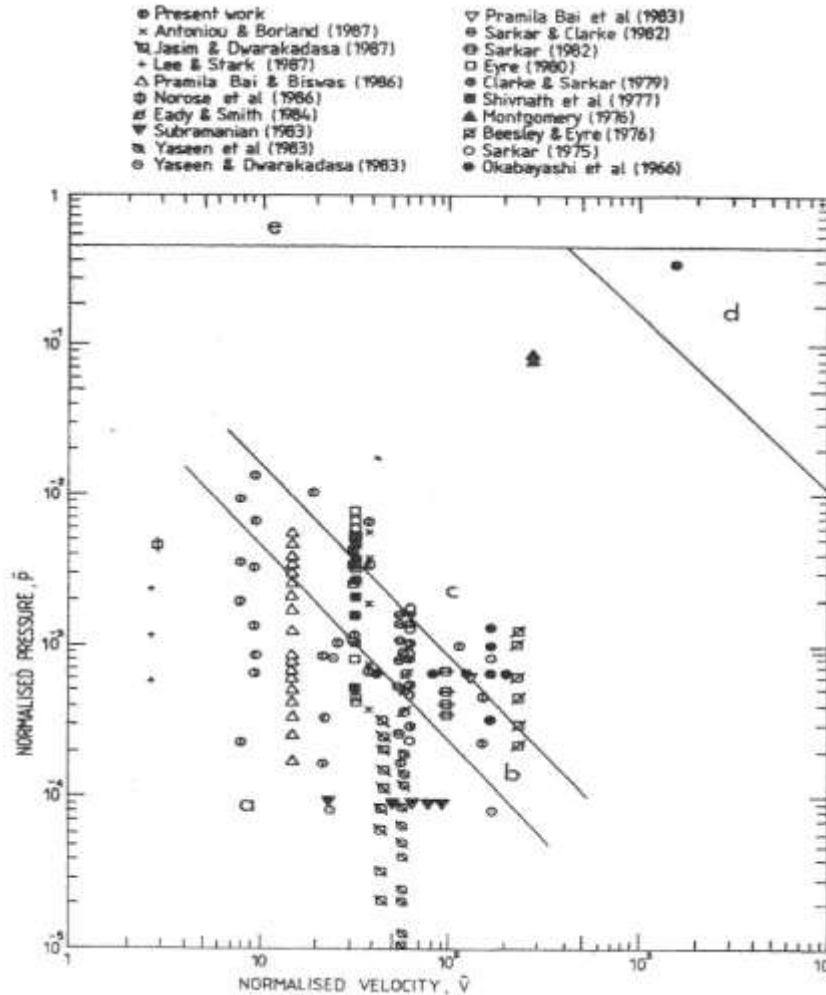


Figure 2.23 Wear rate versus load for four different Al-Si alloy systems



**Figure 2.24 Wear mechanism map for aluminum alloy [97]**

### 2.12 Effect of Silicon Content on Wear

The amount and distribution of Si particles play an important role on the wear behavior of aluminium alloy. There are contradicting findings in the literature on the effect of silicon.

Shivanath et al. [113] studied the wear behavior of binary Al-Si alloys with silicon content varying from 4 to 20% using a pin-on disc wear tester against steel disc. The authors conducted the tests at a constant speed of 1 m/s up to a load of 24 kg and observed that the amount of silicon had a significant effect on the transition load from mild wear to severe wear with the exception of Al-11% Si alloy, which showed a discontinuity in the linear relation between transition load and the silicon content. The authors also found that within the mild wear or oxidative wear region, the wear rates were independent of the silicon content or the particle size of the silicon. Clarke and Sarkar [114] also conducted similar wear studies using a pin-

on-bush wear tester on binary Al-Si alloys with silicon content varying from 2 to 22% Si against a hard EN31 steel disc. Wear rate as a function of silicon content from this study revealed that the beneficial effects of silicon on wear resistance increased up to 11% Si, after which the wear resistance decreased and the higher silicon content had no beneficial effect.

In fact, silicon particles in hypereutectic alloys caused wear on the steel counterface. The authors also reported that the only benefit in hypereutectic alloys was that the seizure load in those alloys was higher than the hypoeutectic alloys. Andrews et al. [115] studied the effect of silicon content on the wear behavior of hypereutectic alloys containing 17, 20, 23 and 26% silicon using pin-on-disk wear tester against M2 tool steel disk. The alloys had other alloying elements such as 4.5%-3.2% Cu, 0.5%- 0.3% Mn, 0.1% Zn, 0.2% Ti, 0.05% P, and 0.4% Fe. The authors in this study showed that an increase in silicon content resulted in a reduction in wear rates and an increase in the transitional load from mild wear to severe wear. Later Pramila Bai and Biswas [116] studied the wear behavior of binary Al-Si alloys with silicon content varying from 4%-24% in a POD wear tester against EN 24 steel disc. Using variance analysis, the authors concluded that the silicon content had no significant effect on the wear rates and the coefficient of friction of the alloys studied in the range of 4%-24%. However, the wear rate of these alloys was much lower compared to commercial pure aluminum. Torabian et al. [117] also examined the effect of silicon content on the wear behavior of binary Al-Si alloys with silicon content varying from 2 to 20% and found that the wear rate decreases with increase in silicon content. However the decrease in wear rate was not significant after 15% silicon content. The transitional load from mild wear to severe wear was also decreased with increase in silicon content, and the wear process changed with alloy composition and the experimental conditions; wear debris were generated by cracking and spalling of oxide particles and by delamination of surface layers.

In general, the high wear resistance of Al-Si alloy is attributed to the presence of hard Si particles distributed uniformly throughout the matrix. The distribution and size of the Si particles determine the wear behavior of material.

### **2.13 Effect of Grain Size on Wear**

The effect of grain size on the tribological behavior of Al alloy is an important topic and has received much attention. In general, finer grain size Al alloy has better wear resistance. Hisakado [118] reported that larger grain sizes are associated with larger flaw sizes, which in turn leads to a decrease in the critical stress needed for failure. He et al. [119] also reported that the wear resistance of alloy increases with decreasing grain size. Korshunov et al. [120] reported an increase of 2-5 times in the wear resistance of a quenched and tempered steel when the grain size was reduced from 100 to 10  $\mu\text{m}$ . They have also observed a slight (15%) reduction in the average value of the coefficient of friction within this grain size range.

There have been few reports however, where the opposite was found. For example, Xiong et al. [121], using a pin-on-flat type wear test where the apparent contact area was maintained constant, reported that larger Al grains exhibited better wear resistance. They also suggested that the fine grains ( $\approx 4\mu\text{m}$ ) entrapped wear debris, increased the real area of contact between the pin and the disc and induced an increased wear rate from third body abrasion. The large grains ( $\approx 14\mu\text{m}$ ) were not as easily pulled out.

Generally, smaller matrix grain size leads to several benefits such as improved mechanical properties, reduced porosity and improved surface finish [122-124].

### **2.14 Effect of Porosity on Wear**

Porosity is a very common microstructural defect in cast or sintered products. The influence of porosity on the wear behavior of materials has been reported as sometimes beneficial or detrimental in several studies [125-138].

Porosity has a significant influence on wear rate when the applied load is large enough to render the pores beneath the worn surface unstable. Fracture and plastic deformation are considered to be the main causes of severe wear. If the strain-induced shear stress is larger than the shear strength of the material itself in the subsurface, wear resistance will decrease severely. Thus the occurrence of severe wear depends on strain-induced shear stress and the shear strength of the material. The presence of pores decreases the shear strength of material since shear fracture takes place directly through these pores. In addition, the increase of applied load can promote the enlargement of the size of the deformation zone beneath the worn surface, so that more pores can influence the wear process.

Sub-surface pores usually elongate in the direction of sliding and in some cases close locally. During the period of repeated sliding, elongated pores near the surface eventually propagate up to the sliding surface and form flake-like debris. In another sense, the formation of surface cracks and attendant debris may be a consequence of pore deformation and pore coalescence in the sub-surface layers or micro crack nucleation at the subsurface pores. If pore closing occurs, it is predictable that the wear rate will decrease considerably and the compact behaves similarly to a material of lower porosity. This behavior was reported in previous investigations [139-141].

Hardness may be the main factor determining the abrasive wear behavior. An increase in hardness gives rise to a decrease in wear rate [142], but is often altered by porosity [143]. Wang et al. [144] showed that, under the same wear test conditions, and owing to high hardness and low porosity, the wear coefficient becomes much smaller. This indicates that low porosity and high hardness are mainly responsible for low wear coefficient in the running-in process.

## **CHAPTER 3    EXPERIMENTAL METHODS**

### **3.1 Materials**

Three materials are used in this study; high pressure die cast A380M aluminium alloy, 6061 and pure aluminium powders. The high-pressure die cast A380M aluminum alloy was obtained from Magna Powertrain, while 6061 and pure Al powders were obtained from Ecka granuels.

### **3.2 Powder Metallurgy Specimens Preparation**

#### **3.2.1 Powder Blending**

The powders were weighed using a Denver Instrument APX-1502 scale and placed in Nalgene bottle. A total of 0%, 1.5%, 10.5% and 14.5% lubricant (Lico wax C) was added to the powders separately and then blended in a Turbula Model T2M mixer for 40 minutes to ensure homogeneity. Figure 3.1 shows the Turbula Model powder mixer.



**Figure 3.1 Turbula Model T2M mixer used for homogenizing the powder**

### 3.2.2 Powder Compaction

Rubber molds were filled with the blended powders and sealed with electrical tape. The sealed molds were then transferred to a cold isostatic press chamber for wet bag pressing. The chamber was then filled with a mixture of water and water soluble oil (20:1). Using a high pressure air-operated piston type pump, the pressure within the pressure chamber was increased to 200MPa and maintained for a dwell time of 5 minutes. Using the decompression valve, the pressure was then reduced at a rate of 1ksi/s to atmospheric pressure and molds removed. The net result was that the loose powder was pressed into a single coherent body of the same shape (but not dimensions) as the rubber mold. This material a “green body” was very porous, brittle and friable. To increase density, green bodies were subsequently sintered. Figure 3.2 is the cold isostatic pressing machine used for compacting powders.



**Figure 3.2 Cold isostatic pressing machine**

### 3.2.3 Sintering

The sintering of compacted samples was conducted in a Lindberg Blue 3-Zone Tube Furnace Model STF55666C-1 (Fig. 3.3). Here, samples were set on a tray that was then placed in the furnace at a location optimized for minimal temperature deviation. Once the samples were placed in the furnace a vacuum pressure in the tube was reduced to a value less than  $9.9 \times 10^{-2}$  Torr and then backfilled with nitrogen. This was then repeated to minimize oxygen contamination in the atmosphere. Nitrogen was then allowed to flow continuously at a rate of 9.4 L/min. Heating of samples then progressed in three stages: de-lubrication, sintering, and post-sinter cooling.



**Figure 3.3 Lindberg tube furnace used to sinter green compacts**

After ensuring that all the oxygen had been evacuated and that the nitrogen was flowing properly, the temperature was quickly ramped to  $400^{\circ}\text{C}$  and held for 20 minutes. After the 20 minutes dewax stage, the furnace was then ramped to the final sintering temperature of  $620^{\circ}\text{C}$  and held for a time period of 30 minutes. The power to the furnace was then turned off and the samples allowed to cool to  $580^{\circ}\text{C}$ . The temperature profile during sintering is shown in Figure 3.4.

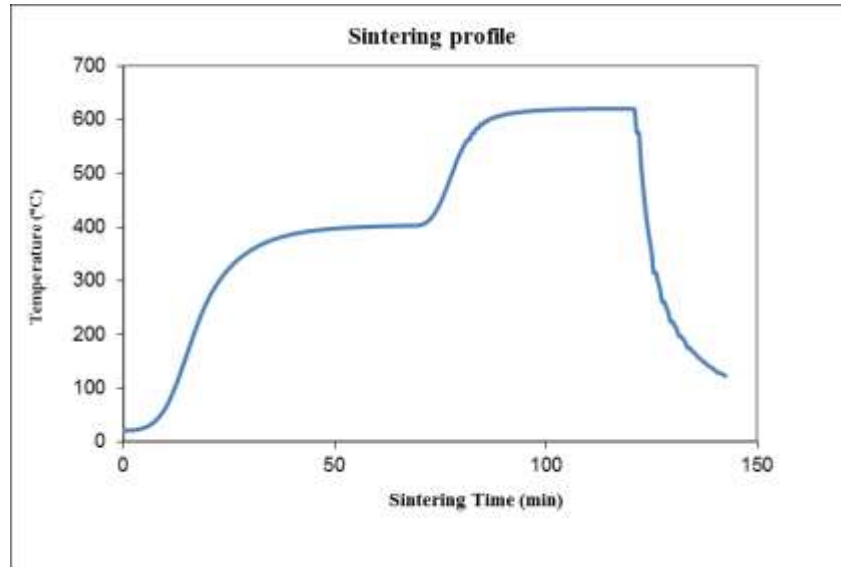


**Figure 3.4 Temperature profile during sintering of pure Al and Al 6061 powders**

### **3.3 Materials Microstructural Characterization**

#### **3.3.1 Optical Microscopy**

The specimens were carefully prepared to produce acceptable quality surfaces for image analysis. Specimens were cut (20 mm × 10 mm × 5 mm), mounted and ground using 240, 320, 400 and 600 grit SiC abrasive papers and then polished using 1 μm, 0.3 μm and 0.05 μm gamma alumina suspension. Keller's solution (1vol% HF + 1.5 vol% HCl + 2.5 vol% HNO<sub>3</sub> + 95 vol% H<sub>2</sub>O) was used as etching reagent and the specimens were emerged in the solution for 15-20 seconds. Olympus BX51 research microscope (Figure 3.5), equipped with bright-field objectives was used to analyze the microstructure at high resolution.



**Figure 3.5 Olympus BX51 research microscope**

### 3.3.2 Porosity Measurement

The green and sintered densities of samples were determined in accordance with MPIF (Metal powder industries federation) Standard 42 (2002). In order to measure the un-sintered (green) density of the compact, the weight of the samples were taken in air ( $w_{air}$ ) and after immersion in water ( $w_{water}$ ). The temperature of the water was also recorded. The green density was then calculated using the following equation,

$$\rho_{Green} = \frac{W_{air} \times \rho_{water}}{W_{air} - W_{water}} \quad \text{Equation 3.1}$$

where,  $\rho_{water}$  is the density of water measured using,

$$\rho_{water} = 7 \times 10^{-8}T^3 - 1 \times 10^{-4}T + 0.9996 \quad \text{Equation 3.2}$$

where T is the measured temperature of the water in degree Celsius. In order to seal the surface-connected porosity the parts/test pieces are oil impregnated or the pores are filled with a suitable material. The sintered density was performed by weighing the samples in air, prior to infiltrating them with ESSO-NUTO H46 hydraulic oil under vacuum for 30 min. The vacuum was released and the specimens were placed on a screen to drip dry for 5-7 minutes before continuing. Specimens were then lightly wiped, cleaned and weighed in air (with oil impregnation). Finally, oil-impregnated samples were weighed in water and the sintered density was calculated as follows:

$$\rho_{sintered} = \frac{W_{air} \times \rho_{water}}{W_{ao} - W_{wo}} \quad \text{Equation 3.3}$$

where,  $W_{ao}$  is the weight of the oil infiltrated specimen in air and  $W_{wo}$  is the weight of the oil infiltrated specimen in water.

$$\text{Vol \% porosity} = 100 - \left( \frac{\text{sintered density}}{\text{theoretical density}} \times 100 \right) \quad \text{Equation 3.4}$$

Here, the theoretical density of pure Al and Al 6061 was calculated to be 2.69 g/cc and 2.70g/cc according to the rule of mixture. Calculated green and sintered densities and % porosity for pure and 6061 Al as a function of the amount of wax used are given in Tables 3.1 and 3.2, respectively.

**Table 3.1 Basic properties of sintered pure Al**

	Green density (g/cc)	Sintered density (g/cc)	Volume porosity (%)
No wax	2.51	2.62	2.7
1.5% wax	2.32	2.40	11
10.5% wax	1.98	2.05	24
14.5% wax	1.56	1.78	34

**Table 3.2 Basic properties of sintered Al 6061**

	Green density (g/cc)	Sintered density (g/cc)	Volume porosity (%)
No wax	2.49	2.52	6.6
1.5% wax	2.24	2.32	14
10.5% wax	1.75	1.86	31
14.5% wax	1.48	1.57	41

### 3.3.3 Area Percent Porosity

Surface porosity of samples was calculated using image analysis software (Image-Pro Plus, version 6.3.0.512). A series of images were taken to cover the whole surface area of the sample. Porosity was identified based on pores gray-level intensity differences compared to the matrix. Gray-level threshold settings were selected to permit independent detection of porosity, using the flicker method of switching back and forth between porosity and the matrix. Second-phase particles and dendrite may be counted as porosity because their gray-level range is similar to that of porosity. The grey-level thresholds as well as boundary conditions (i.e., aspect ratio, min radius and area) were carefully controlled in order to avoid the identification of second-phase particles and dendrite as porosity. A counting protocol was chosen to correct for edge effects so that a porosity lying across a field boundary is counted only once (Standard Practice for Determining the Inclusion or Second-Phase Constituent Content of Metals by Automatic Image Analysis, 2008).

For each field, the area fraction of the detected area of porosity was measured by dividing the detected area of porosity by the area of the measurement field. The area fraction of the porosity of  $i^{\text{th}}$  field ( $A_{Ai}$ ) was calculated using the following equation:

$$A_{A_i} = \frac{\sum_{j=1}^{j=m} A_j}{A_T} \quad \text{Equation 3.5}$$

Where,  $A_T$  is the total field area ( $\mu\text{m}^2$ ) and  $A_j$  is the area of the detected  $j^{\text{th}}$  pore ( $\mu\text{m}^2$ ) of total 'm' pore present in the  $i^{\text{th}}$  field. The average area fraction of porosity of the total 'n' field ( $\overline{A_A}$ ) was calculated by:

$$\overline{A_A} = \frac{\sum_{i=1}^{i=n} A_{A_i}}{n} \quad \text{Equation 3.6}$$

Where, n is the number of field's measured or total number of images taken to cover the surface area of the sample. The standard deviation (S), 95% confidence interval (95% CI) and percent relative accuracy (% RA) was calculated using the following equations:

$$S = \left[ \frac{\sum (A_{A_i} - \overline{A_A})^2}{n-1} \right]^{1/2} \quad \text{Equation 3.7}$$

$$95\% \text{ CI} = \frac{st}{\sqrt{n}} \quad \text{Equation 3.8}$$

$$\% \text{ RA} = \frac{95\% \text{ CI}}{A_A} \times 100 \quad \text{Equation 3.9}$$

The value of percent porosity is expressed as the mean value plus or minus the 95% CI. Here, 't' is a constant, the value of which is expressed as a function of n. Over n = 30, the value may be defaulted to a value of 2. The percent relative accuracy (% RA) is an estimate of the percent of error of each measurement as influenced by the field-to-field variability of the values.

### 3.3.4 X-ray Diffraction

X-ray diffraction was conducted on as received Al A380M, pure Al and Al 6061 alloy. The Al A380M specimen was cut (20 mm × 10 mm × 5 mm) ground and polished down to 0.05 μm, as described in section 3.2.1. The samples were then cleaned in methanol in an ultrasonic bath and mounted in a specimen holder. The raw powders were placed in shallow sample holders. X-ray diffraction (XRD) was carried out employing a high-speed Bruker D8 Advance XRD system. The XRD system uses a high-speed Lynx Eye™ detector and CuKα radiation having a wave length of 1.54 Å, tube voltage of 40 kV and tube current of 40mA. Samples were scanned from a 2θ angle of 20° to 140° with a step size of 0.049°. Diffraction patterns were analyzed using Bruker's EVA software and compared to known diffraction patterns present in the International Centre for Diffraction Data (ICDD) powder diffraction file (PDF) database. Al and Si peaks were matched to those in the Powder Diffraction Files and identified as having FCC crystal structures. The XRD system is shown in Figure 3.6.



**Figure 3.6 Bruker D8-Advance XRD system**

### **3.4 Macro and Micro Mechanical Properties**

The macro and micro mechanical properties of the samples were investigated using Rockwell hardness testing and nanoindentation.

#### **3.4.1 Rockwell Hardness Testing**

Rockwell hardness tests were carried out on all specimens; Al A380M, pure Al and Al 6061 alloys. Tests were performed on a Leco R600 Rockwell hardness tester (Figure 3.7) using the “A” scale under a load of 60 Kg with a diamond indenter. Prior to testing, specimens were ground and polished as above. The Rockwell hardness test device was calibrated prior to operation using standard calibration blocks. Six indentations were made at random locations on all the samples.



**Figure 3.7 Rockwell hardness tester (Leco R600)**

### **3.4.2 Nanoindentation**

Nanoindentation experiments were conducted using a nanoindentation system (developed by Bruker, USA) having a nanohardness head and a controller attached to a Bruker multifunctional system. The instrument uses a Berkovich diamond pyramid (Figure 3.8) with an angle of  $65.3^\circ$  between the tip axis and the faces of the triangular pyramid. The displacement of the indentation and the load could be measured independently with a resolution of 0.03 nm and 0.1  $\mu\text{N}$ , respectively. Twelve measurements at twelve different locations on the polished surface were produced on a given specimen using maximum load range from 50 mN to 400 mN in order to ensure that any irregularities in the surface will not affect the hardness values significantly. The test generates a depth versus load curves that can be used to calculate hardness and elastic modulus of the materials. The total penetration depth consists of a plastic component and an elastic recovery component which occurs during the unloading. Maximum indentation depth ( $h_{\text{max}}$ ) can be expressed as:

$$h_{\max} = h_c + \left[ \frac{(\pi-2)}{\pi} \right] \left( \frac{2P_{\max}}{dp/dx} \right) \quad \text{Equation 3.10}$$

where  $p$  and  $h$  are load and indentation depth, respectively.  $h_{\max}$ ,  $P_{\max}$ , and slope at maximum load  $dp/dh$  are determined from the load versus displacement profile. Hardness ( $H$ ) at the maximum applied load was calculated using Oliver and Pharr method [150]. The relationship between  $H$  and the maximum applied load ( $P_{\max}$ ) is as follows:

$$H = \frac{P_{\max}}{A} \quad \text{Equation 3.11}$$

where  $A$  is the area of contact and for Berkovich indenter is given by,

$$A = 24.5h_c^2 \quad \text{Equation 3.12}$$

where  $h_c$  is the contact depth. The elastic modulus can be expressed as

$$E^* = \frac{1}{2} \frac{dp}{dh} \frac{\sqrt{\pi}}{\sqrt{A}} \quad \text{Equation 3.13}$$

where

$$\frac{1}{E^*} = \frac{1-v_1^2}{E_1} + \frac{1-v_2^2}{E_2} \quad \text{Equation 3.14}$$

Here,  $E_2$  and  $v_2$  are elastic modulus and Poisson's ratio of the test material, and  $E_1$  and  $v_1$  are the same parameters for Berkovich indenter. In the current analysis  $E_1$  and  $v_1$  were taken as 1141 GPa and 0.07, respectively.

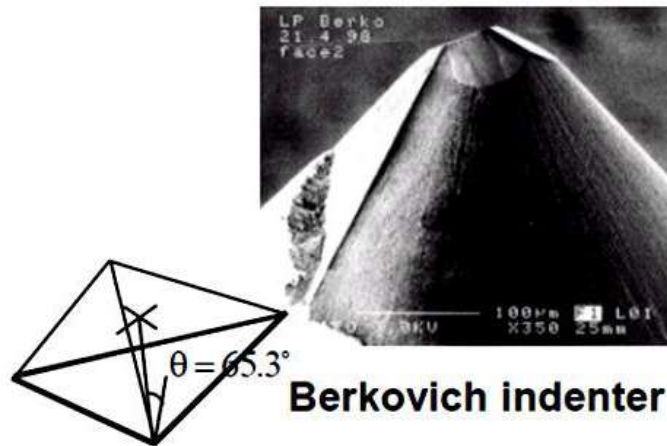


**Figure 3.8 Berkovich diamond indenter**

### **3.5 Tribological Characterization**

#### **3.5.1 Reciprocating Wear Test**

Dry reciprocating wear tests were employed using a Universal Micro-Tribometer (UMT) (manufactured by Bruker, USA). This test method involves a ball upper specimen that slides against a flat lower specimen in a linear, back and forth, sliding motion, having a stroke length of 5.03 mm. All tests were performed at room temperature and at a relative humidity of 40-55%. The load is applied downward through the ball specimen against the flat specimen mounted on a reciprocating drive. The specimens were securely fastened inside the wear chamber. The tester allows for monitoring the dynamic normal load, friction force and depth of the wear track during the test. Figure 3.9 depicts an image of the wear chamber and the sliding ball of the UMT tribometer.

A 6.3 mm diameter AISI 52100 bearing steel ball having a hardness of HRA 83 was used as a counter-face material. The ball was mounted inside a ball holder which was attached directly to a suspension system which, in turn, is attached to a load sensor that controls and records forces during the test. The instantaneous values of calibrated normal load ( $F_z$ ), tangential load ( $F_x$ ), and depth of wear track ( $Z$ ) were measured and continuously recorded using a data acquisition system. The data automatically calculates the variation of the coefficient of friction, COF ( $\mu = F_x/F_z$ ), with time. The weight of the specimen was measured before and after each wear test to determine individual weight-loss at selected time intervals. The test condition for the reciprocating test is given in Table 3.3.

Al A380M, Al 6061 and pure Al specimens were tested under six different loads (1.5 N, 2 N, 2.5N, 3N, 4N and 5N), a frequency of 10 Hz and total time interval of 120 min.

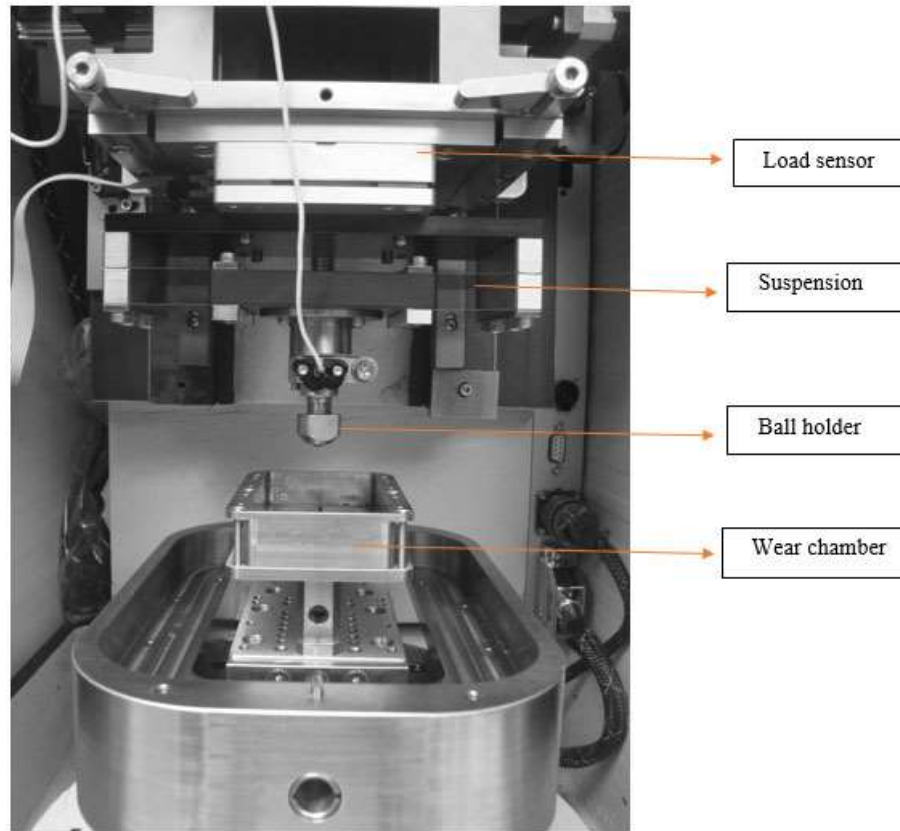


**Figure 3.9 Reciprocating wear tester**

**Table 3.3 Operating conditions for reciprocating wear test**

	<b>Test conditions</b>
<b>Lubricant</b>	None
<b>Temperature</b>	Ambient
<b>Pressure</b>	1atm
<b>Relative humidity</b>	40-55%
<b>Stroke length</b>	5.03mm

Following wear testing, wear debris generated from the tested samples were collected for further analysis.

### **3.6 Scratch Testing**

Scratch tests were performed using a Universal Micro-Tribometer (UMT). This test method utilizes a diamond indenter that slides in a linear sliding motion, having a scratch length of 5 mm. All tests were conducted at room temperature and at a relative humidity of 40-50%. The load is applied downward against the flat specimen. The tester allows for monitoring the dynamic load and friction force. Figure 3.10 represents a schematic diagram of a scratch tester.

A Rockwell diamond indenter tip of radius 200 microns was used in the test. The instantaneous values of calibrated normal load ( $F_z$ ), tangential load ( $F_x$ ) were measured and recorded using a data acquisition system. Various positions were selected on the samples and a single pass scratch test was performed using constant 1N load and a 0.166mm/s indenter velocity.

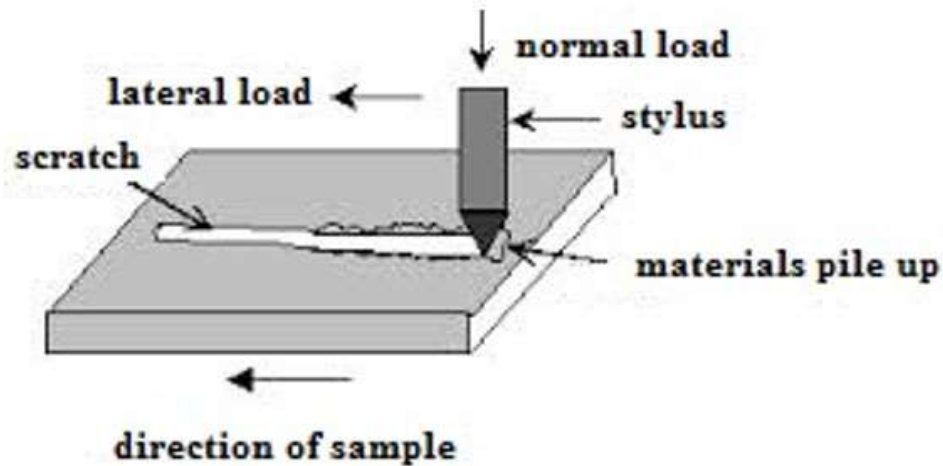


**Figure 3.10 Schematic diagram of scratch tester**

### **3.7 Scanning Electron Microscopy (SEM)**

Hitachi S-4700 cold field scanning electron microscope was used to examine worn surfaces of Al A380M, pure Al, Al 6061 alloy samples and wear debris collected during wear tests. The samples were mounted to aluminum sample stubs using hot glue and copper tape for good conductivity. Wear debris were secured by ultra-smooth carbon adhesive tabs on 15 mm diameter aluminum sample stubs. The SEM was operated at an accelerating voltage of 10 kV, beam current of 15  $\mu$ A, and working distance of 12mm. An Oxford® X-Sight 7200 Energy Dispersive Spectroscopy (EDS) system was also used for chemical analysis of wear tracks and wear debris. INCA software was then used for analyzing the acquired spectra.

### **3.8 Optical Profilometer**

The optical profilometer is a powerful tool for examining both the general features of the wear tracks and determining the volume of the individual wear tracks. The wear tracks may also be examined as pseudo three-dimensional images, allowing for a comparison of track depths. Following reciprocating wear tests, wear tracks were scanned using a non-contact white light optical profilometer. The optical profilometer was built, assembled and programmed at the Advance Tribology Laboratory at Dalhousie University. The optical profilometer uses a high resolution Chromatic Confocal Sensor optical pen attached to STIL Initial controller (STIL, France) and two stepper motors with 3.175  $\mu$ m step size (Figure 3.11). The measuring

range of the optical pen is 4.0 mm. with working distance of 16.4 mm and maximum slope angle of +/- 21°. Software integration for optical pen and stepper motors was performed using Visual Basic.

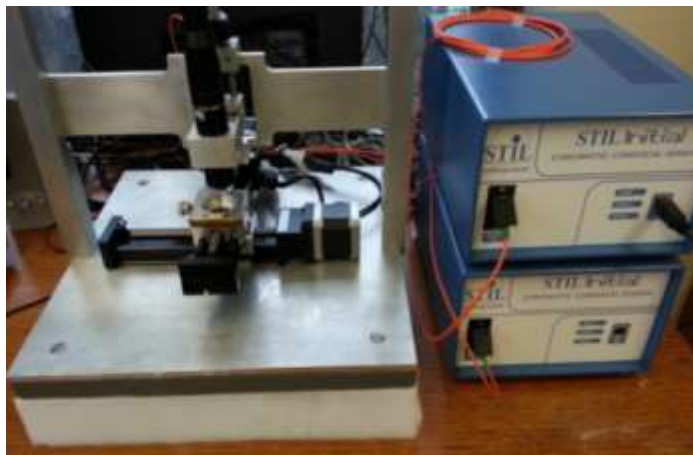


**Figure 3.11 Optical profilometer**

## CHAPTER 4 RESULTS AND DISCUSSION

### 4.1 Materials Characterization

#### 4.1.1 Al A380M Alloy

The chemical composition of Al A380M was determined using inductively coupled plasma mass spectrometry and is summarized in Table 4.1. The letter “M” in A380M indicates higher manganese content. High silicon content helps to increase fluidity and improve corrosion resistance [145-147]. Furthermore, the presence of silicon as an alloying element in these alloys improves wear resistance significantly. However, there is no universal trend in wear behavior of Al-Si alloys with respect to silicon content [148]. In other words, increasing the Si content in the alloy does not always increase the wear resistance. The presence of magnesium improves hardenability, while copper is added to increase low-temperature strength [149].

**Table 4.1 Composition of Al A380M aluminium alloy**

Composition (weight %)						
Al	Si	Cu	Fe	Mn	Mg	Zn
85.2	8.35	3.06	0.87	0.31	0.06	2.15

X-ray diffraction (XRD) was carried out on Al A380M aluminum alloy. Al and Si peaks were matched to those in the Powder Diffraction Files and the alloy is identified as having FCC crystal structure. The XRD pattern for the Al A380M is shown in Figure 4.1.

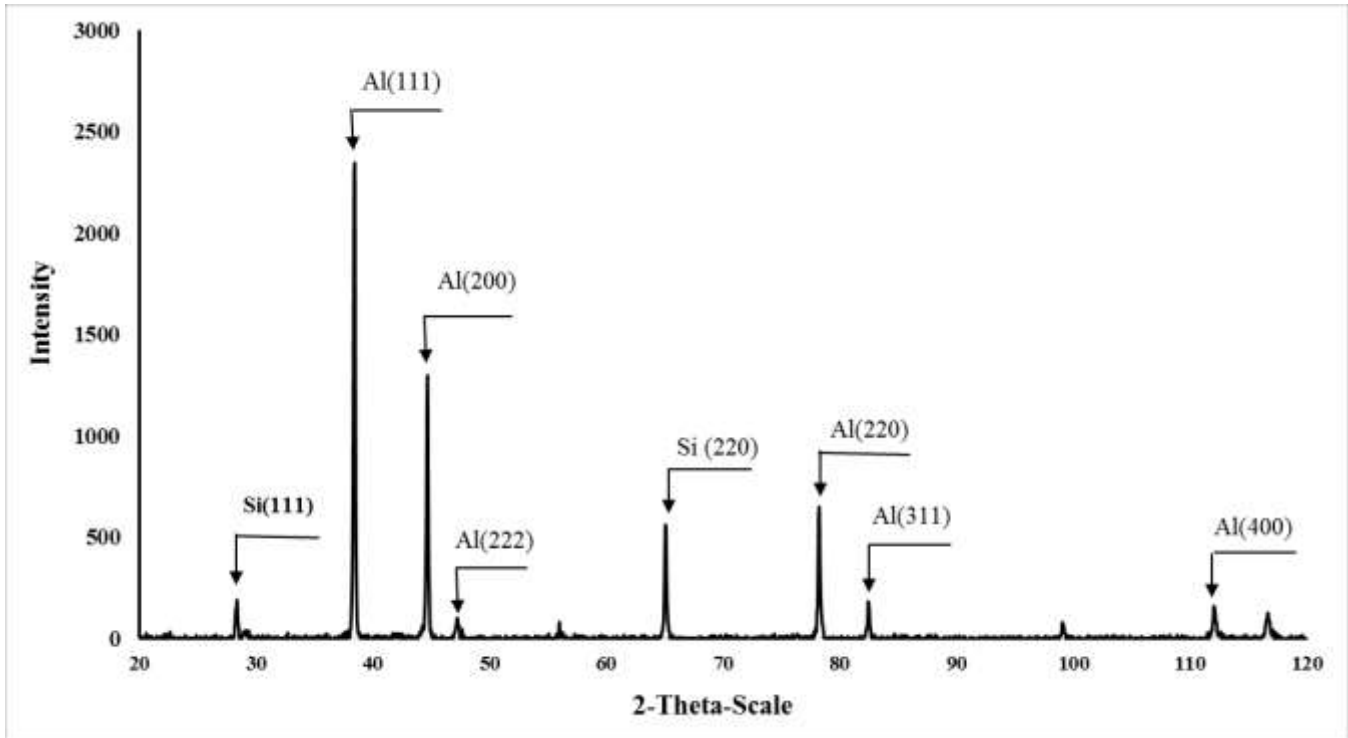


**Figure 4.1 XRD pattern of Al A380M alloy**

Porosity in high pressure die cast aluminium component is caused by the combined effects of solidification shrinkage and gas entrapment. Shrinkage takes place when the metal is solidifying inside the die. This shrinkage may form voids, known as shrinkage porosity. Gas porosity is caused by the entrapment of air during the casting process. Shrinkage porosity tends to be large and irregular in shape while gas porosity is small and spherical in shape. The as received high pressure die cast Al A380M alloy exhibits 0.6% gas porosity and 1.5% shrinkage porosity. These two types of porosity are combined to give a total porosity content of 2.1%. An optical micrograph of Al A380M is shown in Figure 4.2. It was also observed that, the distribution of pores was non-uniform and the pore shape was somewhat irregular. Details of microstructural characteristics are shown in Table 4.2.

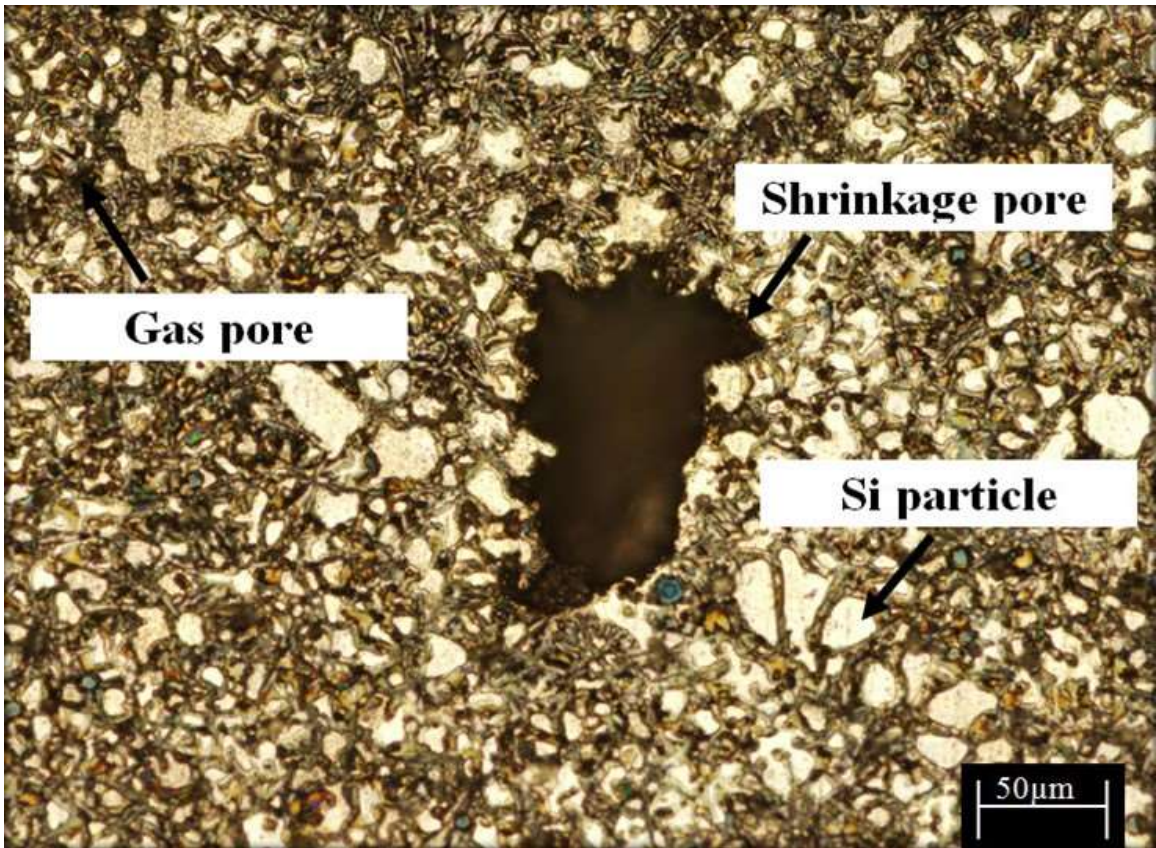


Figure 4.2 Optical micrograph of HPDC A380M Al

Table 4.2 Microstructural characteristics of Al A380M

Specimen	Al grain size (μm)	Pore size (μm)	Pore shape	Surface porosity (%)	Pore distribution
Al A380M	25	31	irregular	2.1	non-uniform

## 4.1.2 Pure Al and Al 6061

### 4.1.2.1 Powder Characterization

SEM analysis of pure Al and Al 6061 powders were conducted to observe particle morphology. The appearance of these powders are shown in Figure 4.3. Both powders exhibit a somewhat spherical shape. The measured chemistries of each powder is summarized in Table 4.3.

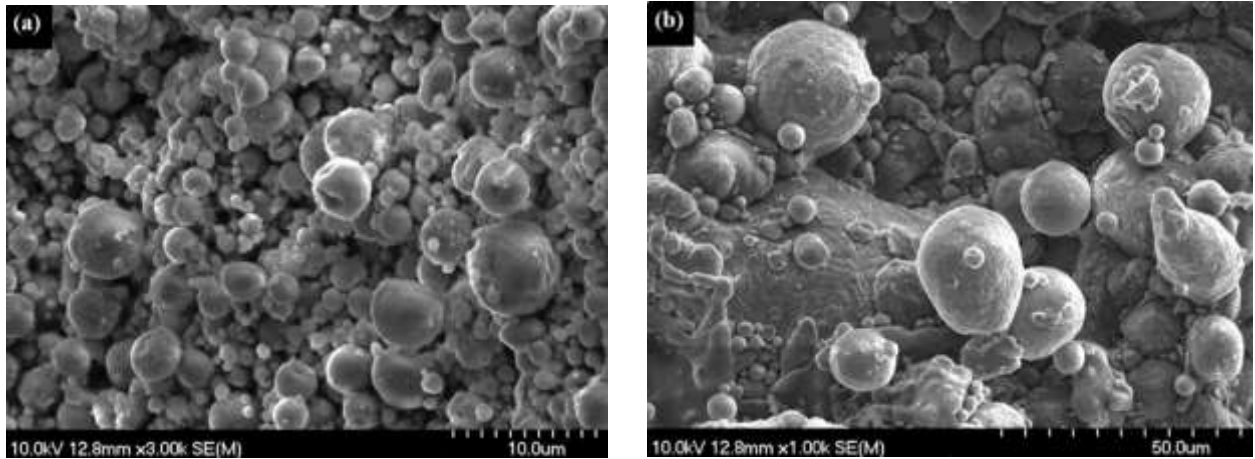


**Figure 4.3 SEM images of raw powders (a) pure Al (b) Al 6061**

**Table 4.3 Chemical composition of pure Al and Al 6061 powders**

Elements (%)	Al	Mg	Si	Fe	Cu	Zn
Pure Al	99.9	0.03	0.03	0.01	0.01	0.02
Al 6061	97.5	1	0.6	0.5	0.2	0.2

X-ray diffraction (XRD) was also carried out on pure Al and Al 6061 powders. Al peaks were matched to those in the Powder Diffraction Files and both powders identified as having FCC crystal structure. The XRD patterns for the pure Al and Al 6061 are shown in Figure 4.4 and 4.5.

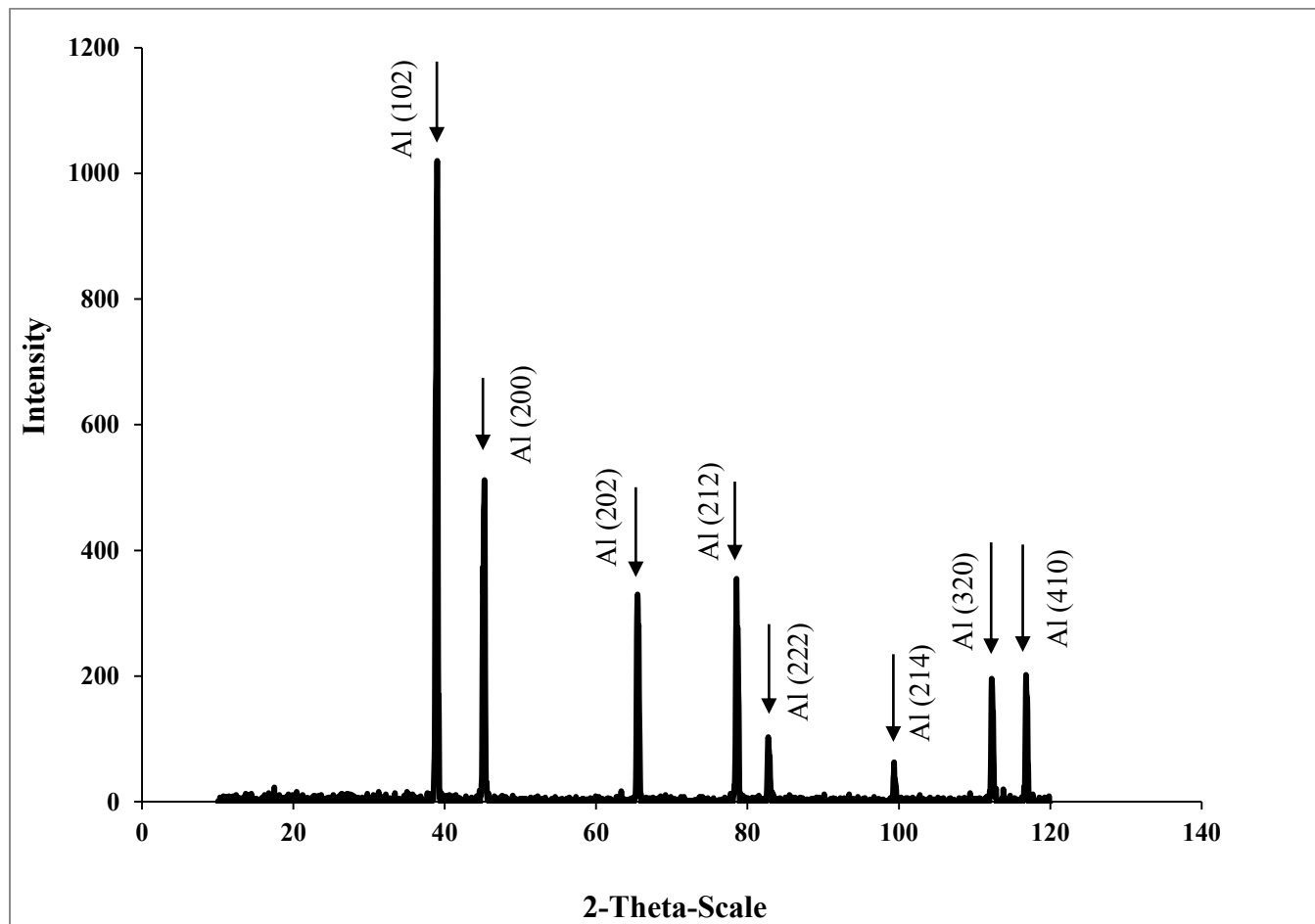


**Figure 4.4 XRD pattern of pure Al**

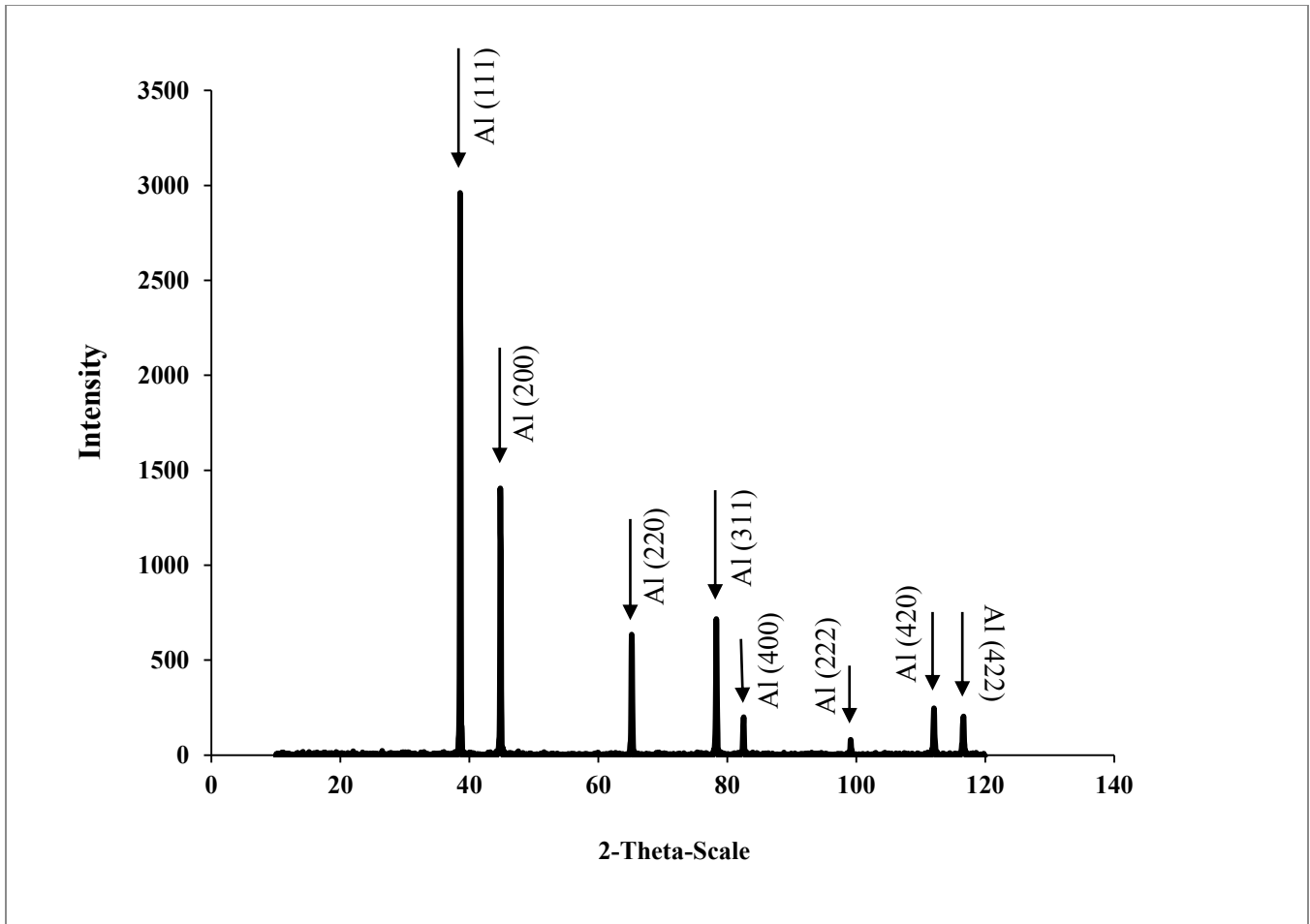


**Figure 4.5 XRD pattern of Al 6061**

Particle size analysis of the raw powders was performed using a Malvern particle size analyzer (model 2600c) equipped with MASTER particle sizer 3.1 analytical software. Tests were conducted using a focal length of 100 mm and a beam length of 300 mm. Particle size distribution data is summarized in Table 4.4. The results of the Malvern examination are shown in Figures 4.6 and 4.7. The  $D_{50}$  line is included in those figures to show the average particle size.

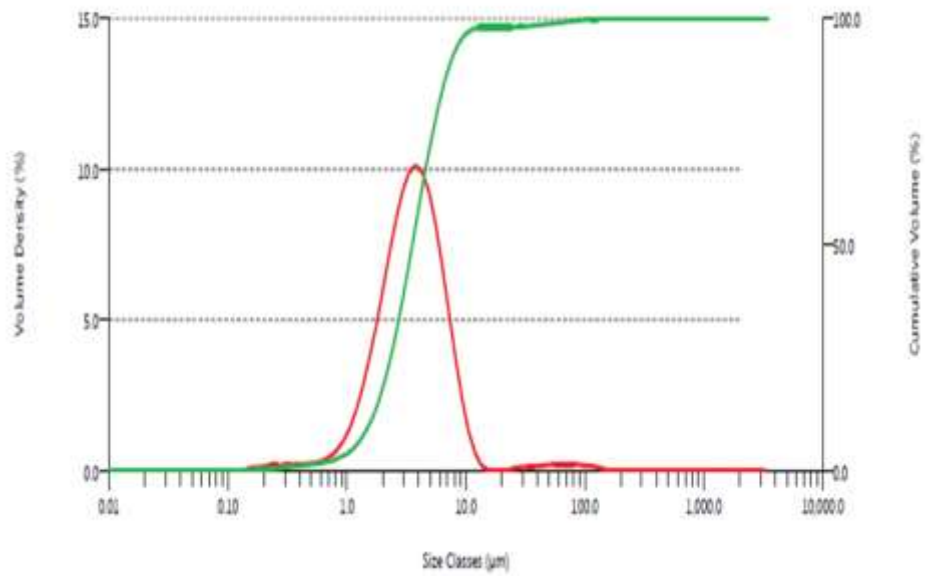


**Figure 4.6 Particle size distribution curve for pure Al powder**

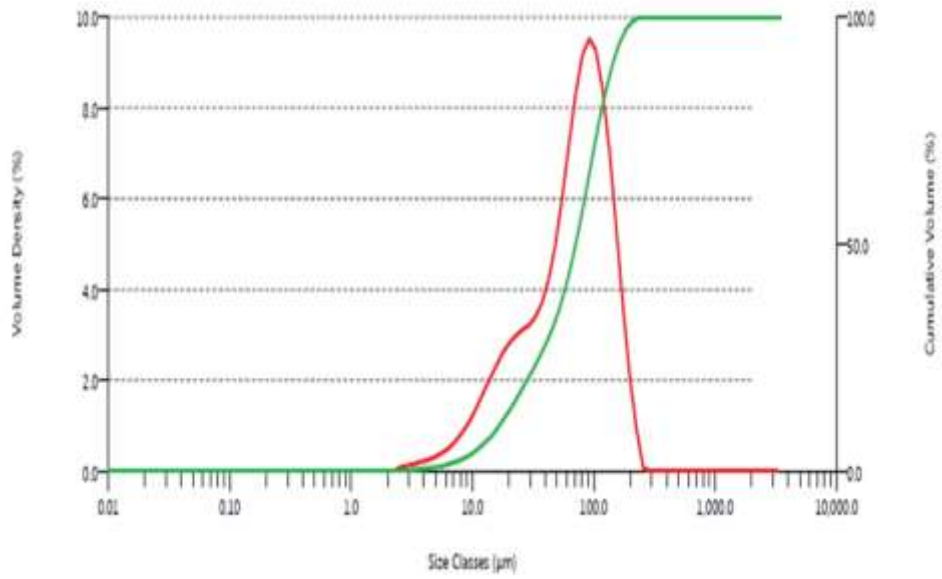


**Figure 4.7 Particle size distribution curve for Al 6061 powder**

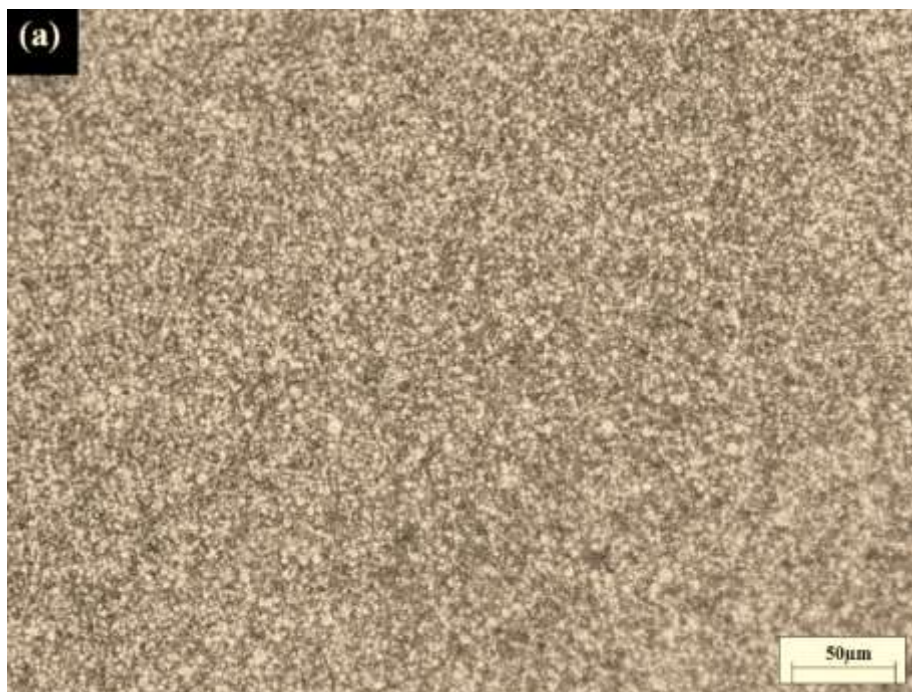
**Table 4.4 Particle size distribution of pure Al and Al 6061**

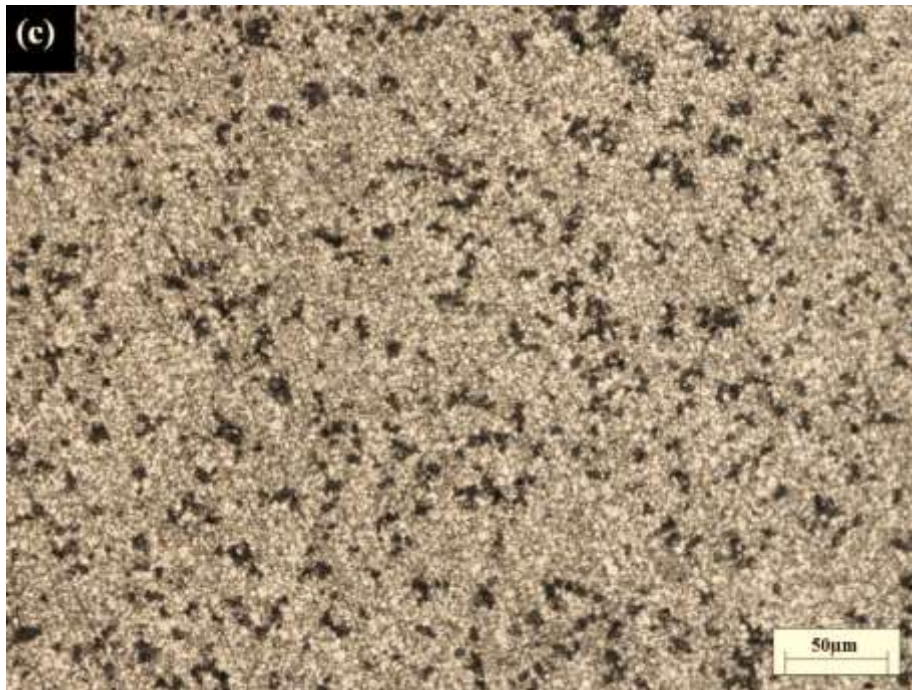
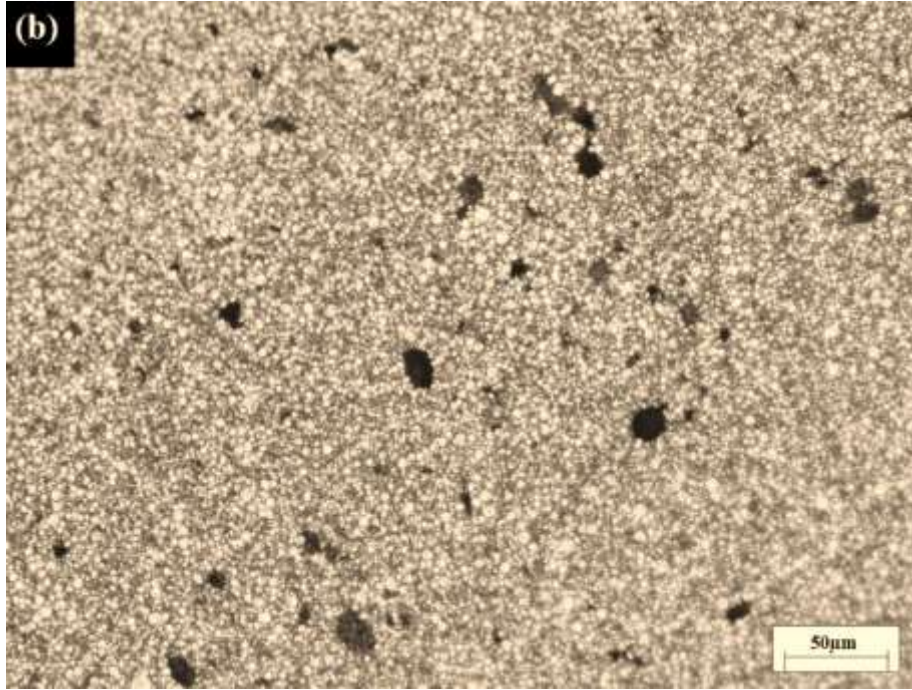
<b>Powders</b>	<b>D<sub>10</sub>(<math>\mu\text{m}</math>)</b>	<b>D<sub>50</sub>(<math>\mu\text{m}</math>)</b>	<b>D<sub>80</sub>(<math>\mu\text{m}</math>)</b>	<b>D<sub>90</sub>(<math>\mu\text{m}</math>)</b>
<b>Pure Al</b>	1.53	3.56	5.78	7.35
<b>Al 6061</b>	16.6	70.9	117	143

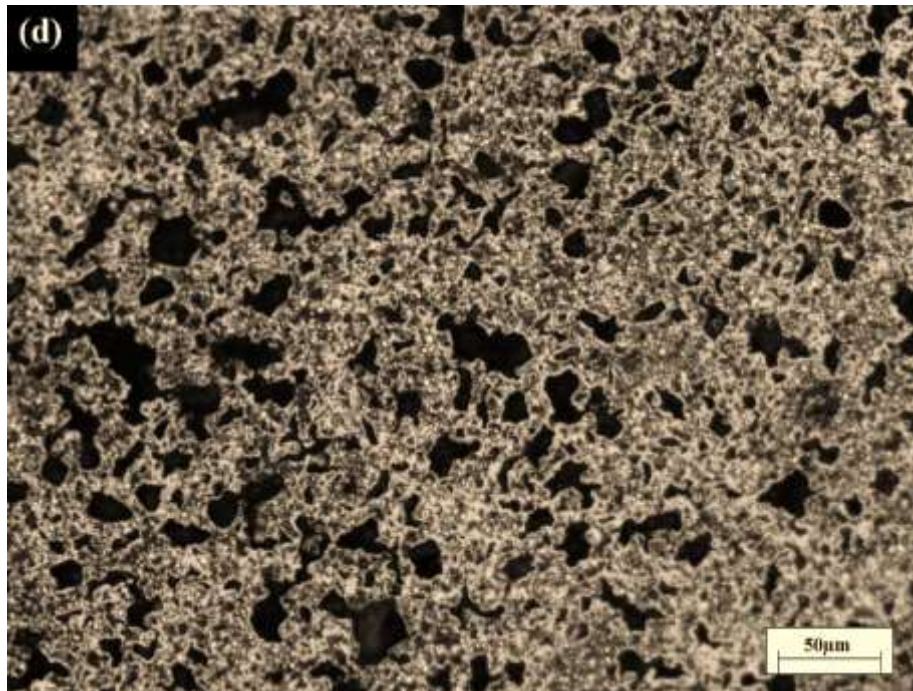
#### 4.1.2.2 Pore Formation in Sintered Pure Al and Al 6061 Alloy

During powder compaction, the size, shape and amount of pores are largely dependent on processing parameters, i.e., amount of lubricant and compaction pressure. During sintering, the lubricant is burned off and as a result material density drops. Also, a lower compaction pressure leads to higher porosity and reduced density of compacts.

Different surface characteristics were observed by varying the amount of lubricant used. Pure Al specimen with no wax has shown less surface porosity than all other specimens. Surface porosity ranges from 1.9% for no wax to 15.1% for 14.5% wax. On the other hand, volume percent porosity ranges from 2.9% to 33.9% respectively. From Figure 4.8 (a, b, c, d) it is clearly observed that with increasing the weight percentage of lubricant, the amount of porosity and the size and shape of the pores change significantly. The dark spots in Figure 4.8 are porosity. Pores became more uniformly distributed and larger in size when using higher amounts of lubricant, which is clearly visible from Figure 4.8 (c, d).



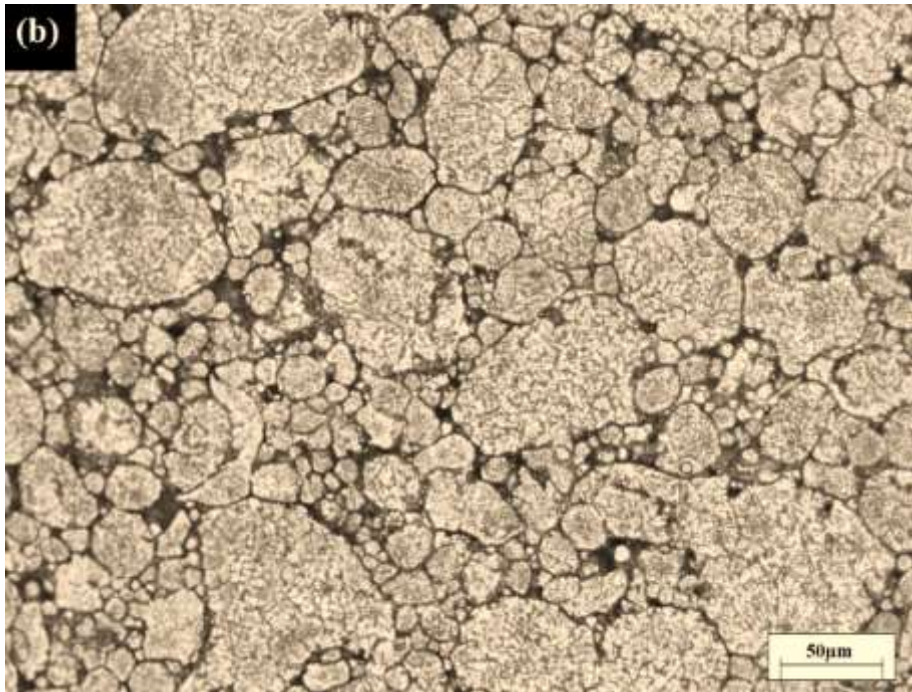
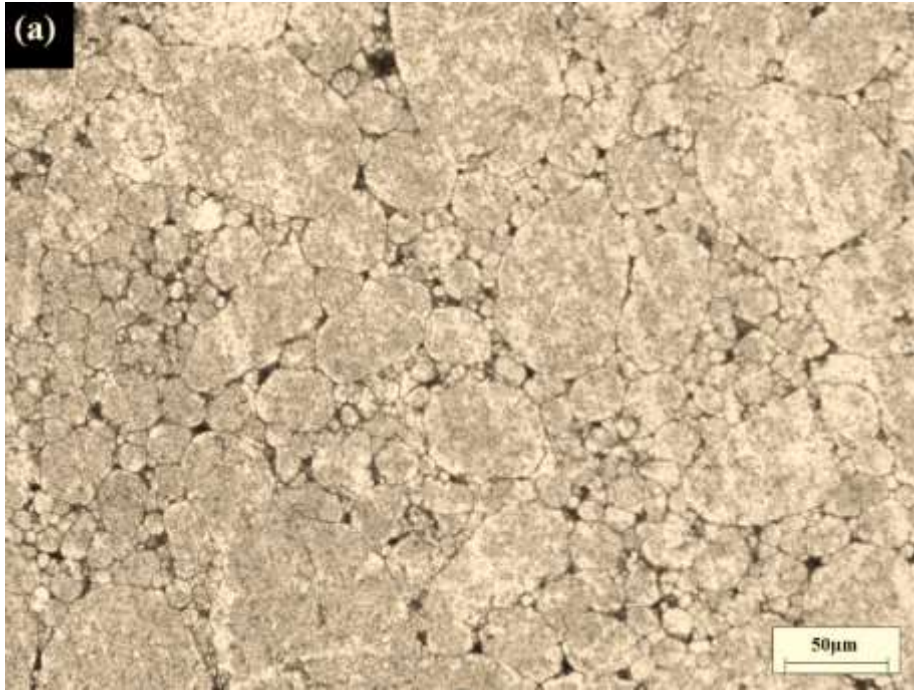




**Figure 4.8 Optical micrographs of pure Al samples mixed with (a) no wax (b) 1.5% wax (c) 10.5 wax (d) 14.5% wax**

In the case of Al 6061, porosity content was higher than that of pure Al for the same amount of lubricant. The surface porosity ranges from 3.5% for no wax to 20.7% for 14.5% wax (Table 4.5). On the other hand, volume percent porosity ranges from 6.5% to 41.7%, respectively. Figure 4.9 (a, b, c, d) shows a significant increase in pore size when the amount of lubricant is increased.

As all the specimens were compacted under the same pressure and sintered under the same sintering conditions, the amount of lubricant plays the most significant role in determining pore size, shape and amount. The added lubricant flows between Al powders and impede pore closure during compaction. Pores that are present in the compact are filled by the lubricant. At the time of sintering, the lubricant is burned off and pores form in those regions of the compact. When more lubricant is added, more spaces are occupied by the lubricant during compaction and subsequently larger pores are formed after sintering and as a result the overall porosity content is increased.



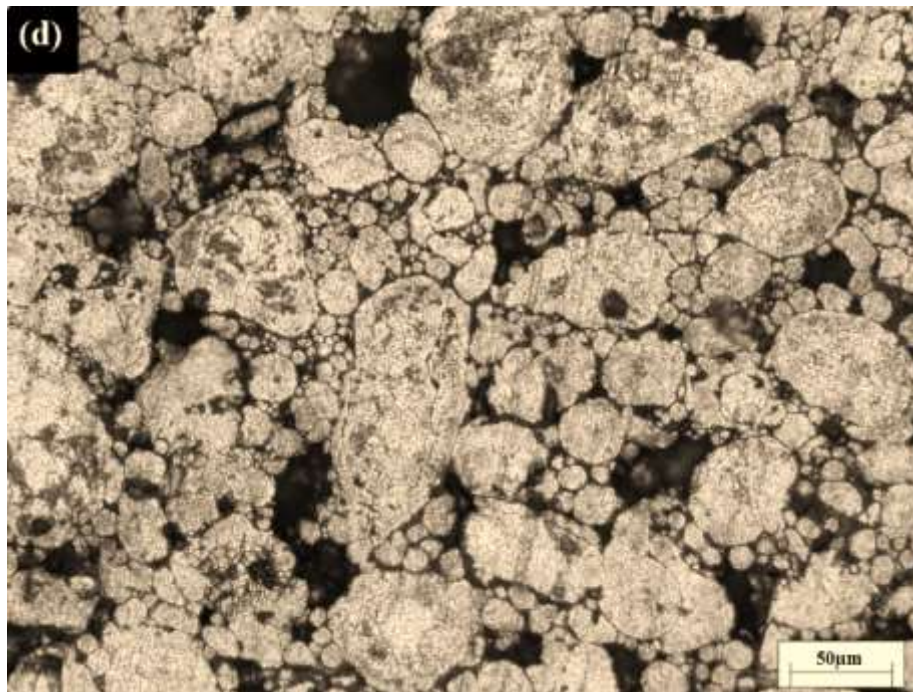
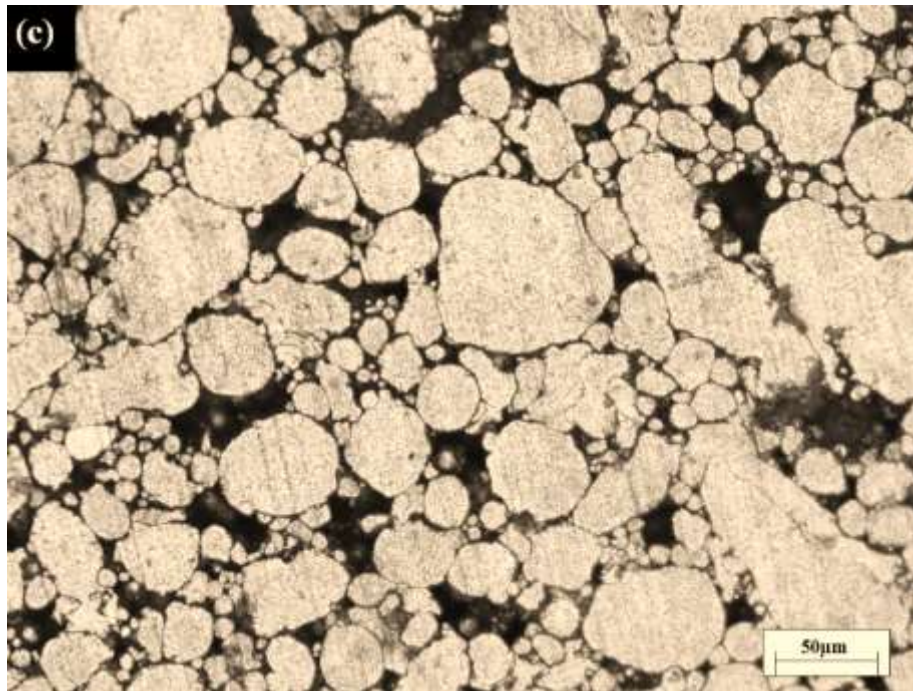


**Figure 4.9 Optical microscopy of Al 6061 samples mixed with (a) no wax (b) 1.5% wax (c) 10.5% wax (d) 14.5% wax**

Detailed descriptions of Al grain size, pore size and pore shape are given in Table 4.5. With increasing the amount of wax, porosity content, pore size, pore shape and porosity distribution vary over a wide

range. For pure Al, the size of pores increased from 2.7  $\mu\text{m}$  at 1.9% surface porosity to about 27  $\mu\text{m}$  for 15.1% porosity. On the other hand, for Al 6061, pore size increased from 12  $\mu\text{m}$  at 3.5% porosity to about 33  $\mu\text{m}$  for 20.7 % porosity. In both cases, surfaces with low porosity content had circular shaped pores, but with increasing porosity content, the pores became irregular. Uniform pore distribution was observed in both pure Al and Al 6061 specimens. It is noticeable from Table 4.5 that, Al (pure and alloy) grain size remained almost constant. For pure Al, the average grain size of all sintered specimens is around 5.5  $\mu\text{m}$  and for Al 6061 is about 45.6  $\mu\text{m}$ .

Generally fine powder particle sizes tend to form smaller grains, while large particles form larger grains. Grain boundaries act as impediments for creating porosity. Due to boundary diffusion, pores that touch grain boundaries are eliminated. The fewer the number of grain boundaries the higher the probability of forming pores. As Al 6061 specimens have larger grain size than pure Al specimens, a higher porosity content was observed in Al 6061 specimens. It can be concluded that smaller initial powder particle size leads to lower sintered porosity.

**Table 4.5 Microstructural characteristics and hardness values of sintered pure Al and Al 6061**

<b>Specimen</b>	<b>Wax (%)</b>	<b>Al grain size (<math>\mu\text{m}</math>)</b>	<b>Pore size (<math>\mu\text{m}</math>)</b>	<b>Pore shape</b>	<b>Volume porosity (%)</b>	<b>Surface Porosity (%)</b>	<b>Rockwell hardness (HRH)</b>
<b>Pure Al</b>	0	5.5	2.7	round	2.9	1.9	80
	1.5	5.5	14.3	round	10.8	5.8	72
	10.5	5.6	19.3	round and irregular	23.8	12.7	61
	14.5	5.5	27.0	irregular	33.9	15.1	48
<b>Al 6061</b>	0	45.6	12.0	round	6.5	3.5	84
	1.5	46.1	20.0	round	13.8	10.3	67
	10.5	45.3	28.0	round and irregular	30.9	16.0	23
	14.5	45.7	33.0	round and irregular	41.7	20.7	8

## 4.2 Effect of Porosity on Mechanical Properties

To investigate the effect of porosity on hardness of pure Al and Al 6061 specimens, a series of Rockwell hardness measurements were conducted and plotted in Figure 4.10. In both cases, hardness decreases with increase in % surface porosity of the specimens. The hardness of pure Al containing 1.9%, 5.8%, 12.7% and 15.1% surface porosity is around 80, 72, 61 and 48 HRH. On the other hand, the hardness of Al 6061 containing 3.5%, 10.3%, 16.0% and 20.7% surface porosity is around 84, 67, 23 and 8 HRH respectively. In the case of pure Al, a reduction in hardness of about 40% is observed as surface porosity increased from 1.9 % to 15.1% and for Al 6061 90 % hardness reduction is observed as porosity increased from 3.5% to 20.7 %. This trend is in agreement with published work [151]. When porosity increases, load bearing area decreases. Moreover, increased porosity in the subsurface raises the chances for crack nucleation and link-up of pores. This results in weakening of the materials and dropping strength. With increasing porosity reduction in hardness in 6061 Al is faster than pure Al because of larger pores. Hardness observed in Al A380M is 102 HRH. The high hardness exhibited by HPDC Al A380M may be contributed to both lower amount of porosity and higher Si content.

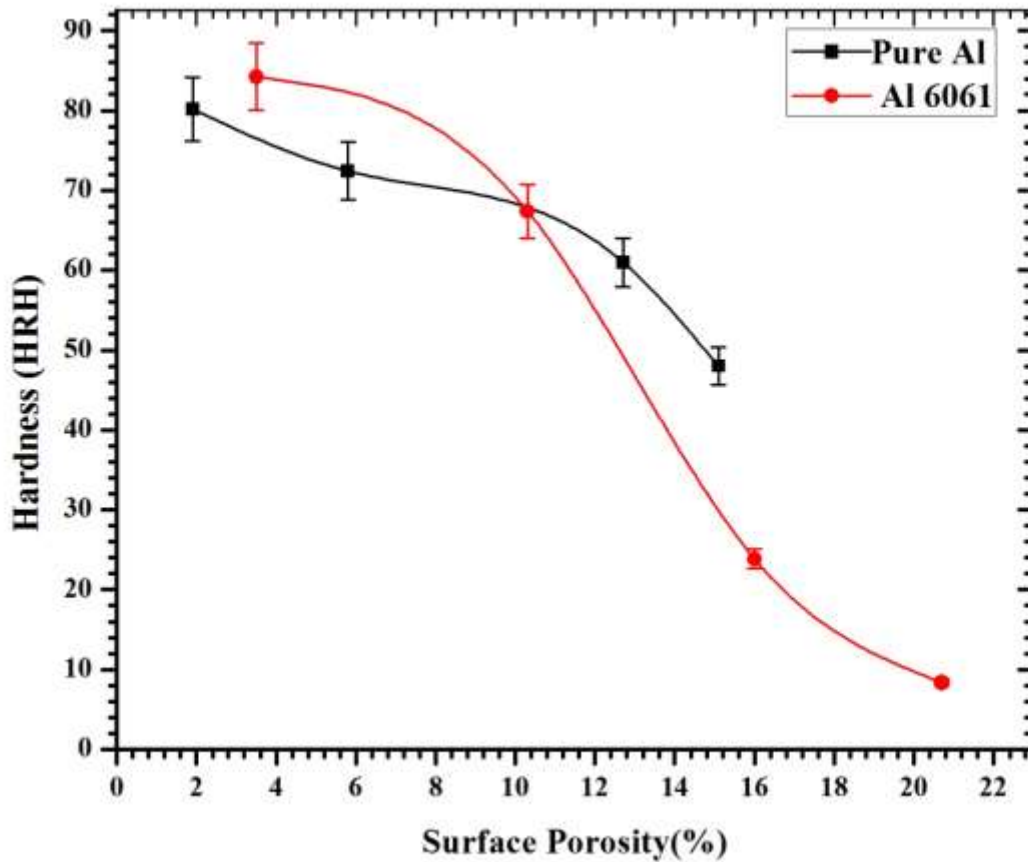


**Figure 4.10 Variation in hardness with surface porosity for pure Al and Al 6061**

Indentation data was collected for various max loads for Al A380M. Each indentation test involves 7 separate indentations on different locations on the specimen surface to compensate for any variations in surface characteristics (i.e., surface pores, defects, grain orientations, etc.). The curves in Fig 4.11 reveal a typical load versus indentation depth patterns. As expected, all curves generated using different maximum loads overlap. The curves exhibit high recoverable deformation and relatively small permanent deformation upon unloading. It is also evident that indentation tests performed under the load range of 50 mN-350mN show residual plastic deformation. The curves show varying hysteresis size as a function of maximum load. Calculated mechanical properties of Al A380M are given in Table 4.6.

Table 4.6 Nanoindentation test data for Al A380M

Physical Properties	
Young's modulus (GPa)	48.90
Hardness (GPa)	1.01

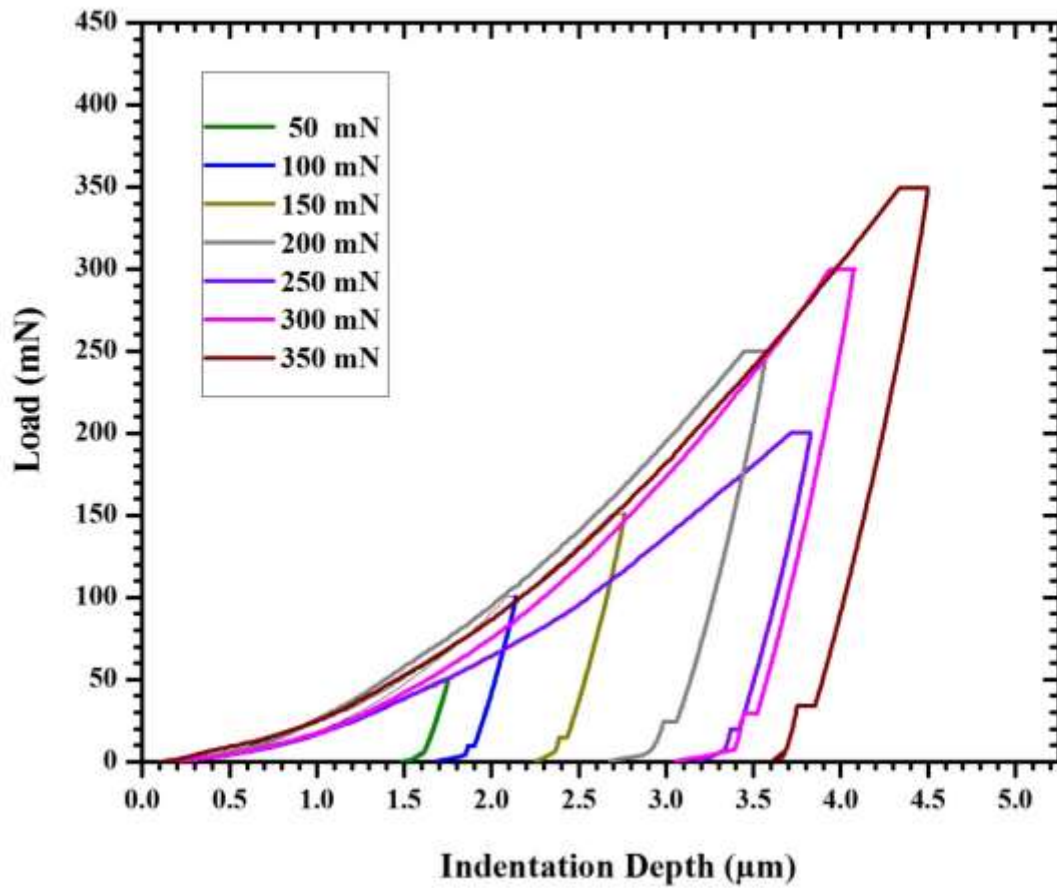
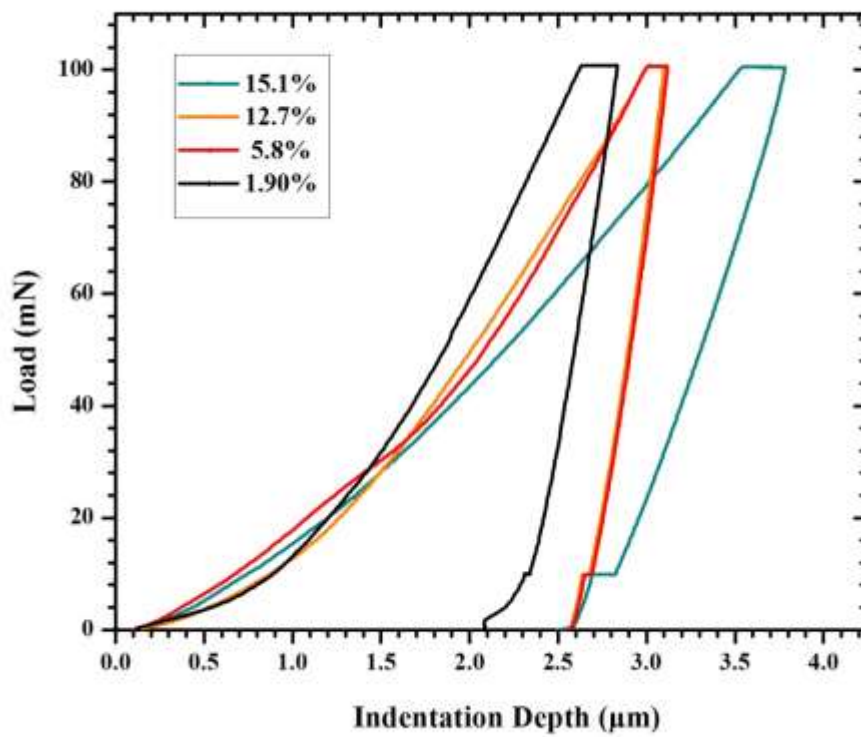


Figure 4.11 Load vs indentation depth profile for Al A380M alloy

Nanoindentation tests were also performed on pure Al and Al 6061 as a function of porosity. Nanohardness and Young's modulus were calculated using Oliver and Pherr method [150]. Figures 4.12 (a) and 4.12 (b) show typical load-depth curves obtained from nanoindentation experiments for pure Al and 6061 Al alloys. The influence of porosity on Young's modulus and nanohardness of pure Al and Al 6061 specimens are given in Table 4.7.



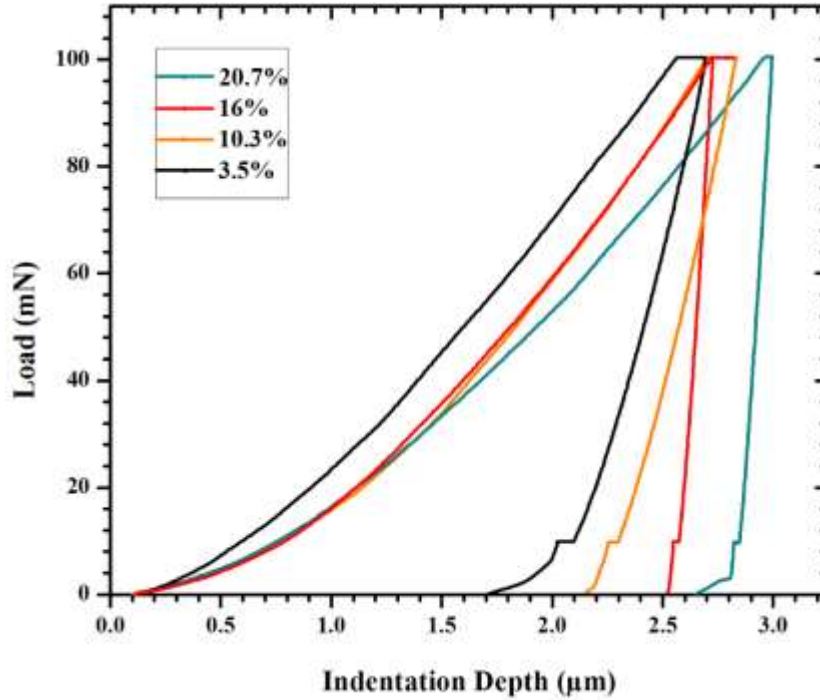


Figure 4.12 Load vs depth profile for (a) pure Al and (b) Al 6061 using 100 mN load

Table 4.7 Nanoindentation test data for sintered pure Al and Al 6061 alloy

Pure Al surface porosity (%)	Young's modulus (GPa)	Hardness (GPa)	Al 6061 surface porosity (%)	Young's modulus (GPa)	Hardness (GPa)
1.9	31.49	0.56	3.5	57.32	0.67
5.8	24.94	0.52	10.2	51.22	0.64
12.5	22.01	0.42	16.0	19.70	0.48
15.1	16.63	0.37	20.7	10.11	0.39

From the above table, it is clear that Young's modulus and nanohardness both decrease with increasing surface porosity. In case of pure Al, a reduction in Young's modulus of about 47% is observed as surface porosity increased from 1.9 % to 15.1% and for Al 6061, 82 % reduction is observed as porosity increased from 3.5% to 20.7 %. In case of nanohardness this reduction is about 34% for pure Al and 42% for Al 6061 with the same amount of porosity increase. The morphology of the pores immediately beneath the Al matrix or within the zone of influence has a significant effect on the response of the indenter and

measured nanohardness and Young's modulus. The resistance that the indenter experience, as it becomes in contact with a solid phase in the Al specimen, depends on whether or not pores are present beneath the surface. As the amount of porosity increases, the resistance to deformation drops. Similarly, the maximum depth ( $h_{\max}$ ) of penetration of the indenter, for a given maximum load, increases with the amount of porosity. In this work, for pure Al, indentation depth increased from 2.5  $\mu\text{m}$  to 3.5  $\mu\text{m}$  for the same constant load 100 mN as the total amount of porosity increased from 1.9% to 15.1%. And for Al 6061, this depth increase was from 2.4  $\mu\text{m}$  to 3.0  $\mu\text{m}$  as surface porosity increased from 3.5% to 20.7%. As outlined in the experimental section, there is an inverse relationship between contact depth ( $h_c$ ) and nanohardness and Young's modulus. Furthermore, the relationship between maximum indentation depth ( $h_{\max}$ ) and the contact depth ( $h_c$ ) is given by the following equation:

$$h_{\max} = h_c + \frac{\pi-2}{\pi} h_e \quad \text{Equation 4.1}$$

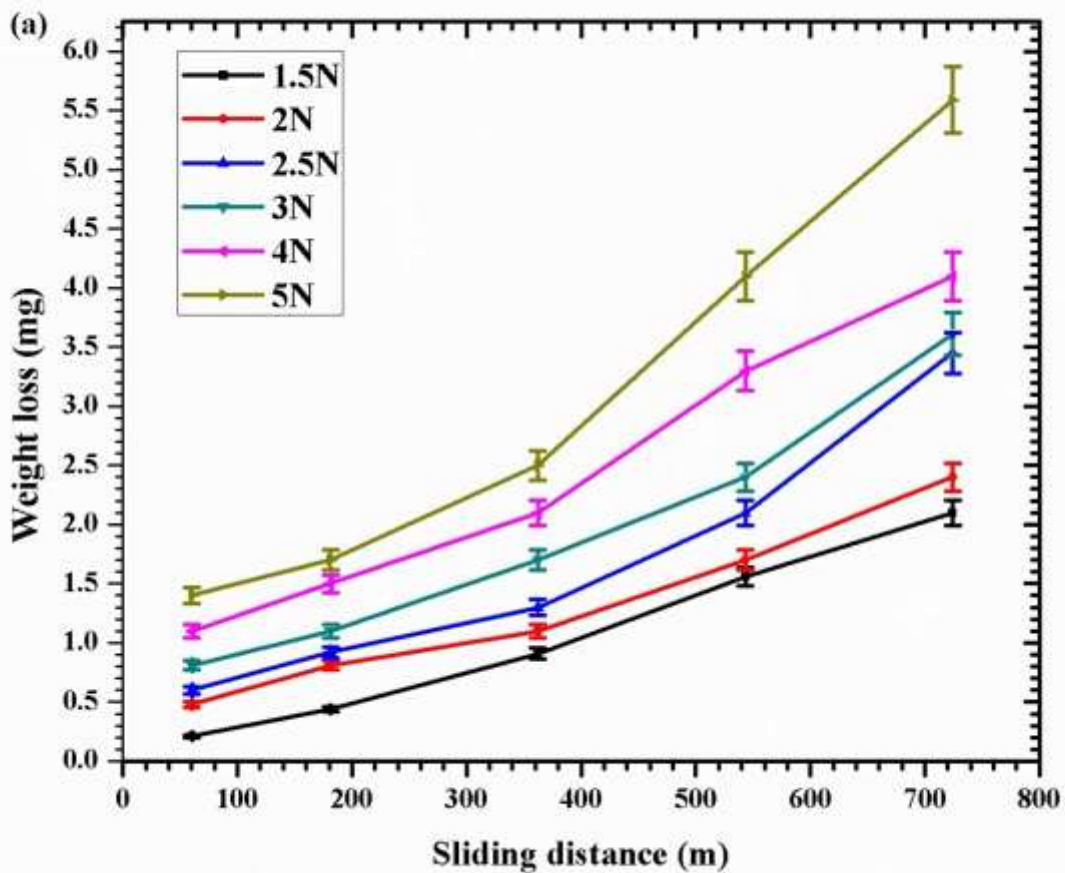
Where  $h_e$  is the elastic depth upon unloading. It can be concluded from this argument that, as the contact depth increases, contact area also increases (Equation 4.1) and accordingly nanohardness and Young's modulus decrease (Equation 3.11 and Equation 3.13). Fleck et al. [152] also studied the effect of porosity on indentation using both finite elemental analysis and cavity expansion model. They suggested that, resistance to indentation decreases with increasing porosity. Similar conclusion has been reached by others [153-155] regarding the relationship between nanohardness, Young's modulus and porosity.

### 4.3 Effect of Surface Porosity on Wear Rate

Figure 4.13 (a,b) represent the correlation between weight loss and sliding distance for pure Al (1.9% porosity) and Al 6061(3.5% porosity) specimens. The plots reveal a somewhat linear increase in weight loss with sliding distance. As expected, it is observed that at any given sliding distance, weight loss increases with applied load as is evident by the upward shift in the weight loss versus sliding distance curve. This trend is in agreement with other researchers [156-164]. To investigate the effect of porosity on wear, wear rate, calculated from the slopes of the weight loss versus sliding distance, is plotted as a function of % surface porosity. The wear rate of pure Al containing 1.9%, 5.8%, 12.7% and 15.1% porosity and of Al 6061 containing 3.5%, 10.3%, 16.0% and 20.7% porosity is plotted in Figures 4.14 and 4.15 respectively. It can be seen from the Figures that the wear rate increases with an increase in surface porosity in both cases. For pure Al, wear rate doubles as surface porosity increases from 1.9% to 15.1% under 2.5N load. A similar trend is also found under other loads. On the other hand, for Al 6061, wear

rate increases two and half times when surface porosity increases from 7.5% to 20.7% under 2.5N load. At high porosity, the surface roughness of the material increases, consequently the possibility of the generation of wear debris increases as a result of asperity-asperity contact. Also, a rise in porosity leads to drop in hardness of the material and therefore affects the rate of wear of the material.

Furthermore, the stress intensity is particularly high near pores which act as sources for cracks during wear. The stress intensity increases with increasing normal load. At low load, the pores beneath the worn surface remain stable and cannot propagate significantly. As a result, subsurface deformation and strain are relatively low. However, with increasing load, pores beneath the worn surface become unstable and cracks originated from these pores can propagate significantly. Consequently, areas surrounding pores become failure-prone.



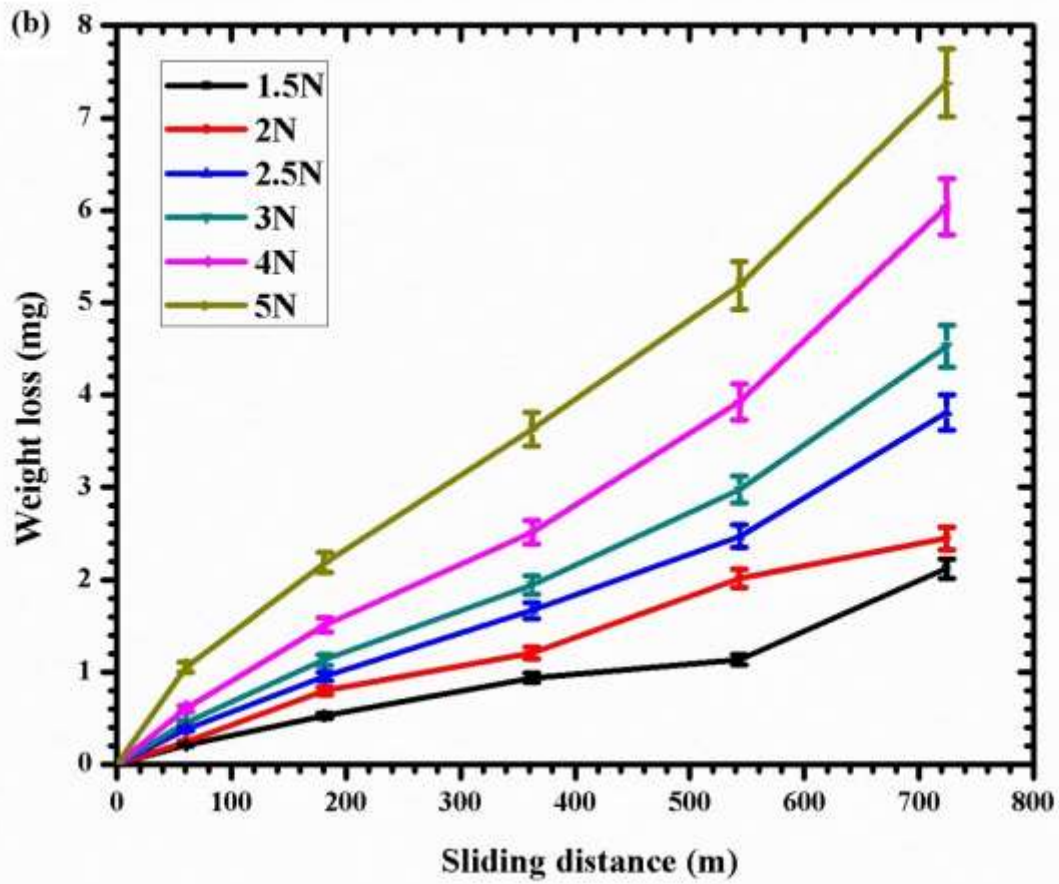


Figure 4.13 Weight loss versus sliding distance curve for (a) pure Al (1.9% porosity) and (b) Al 6061(3.5% porosity)

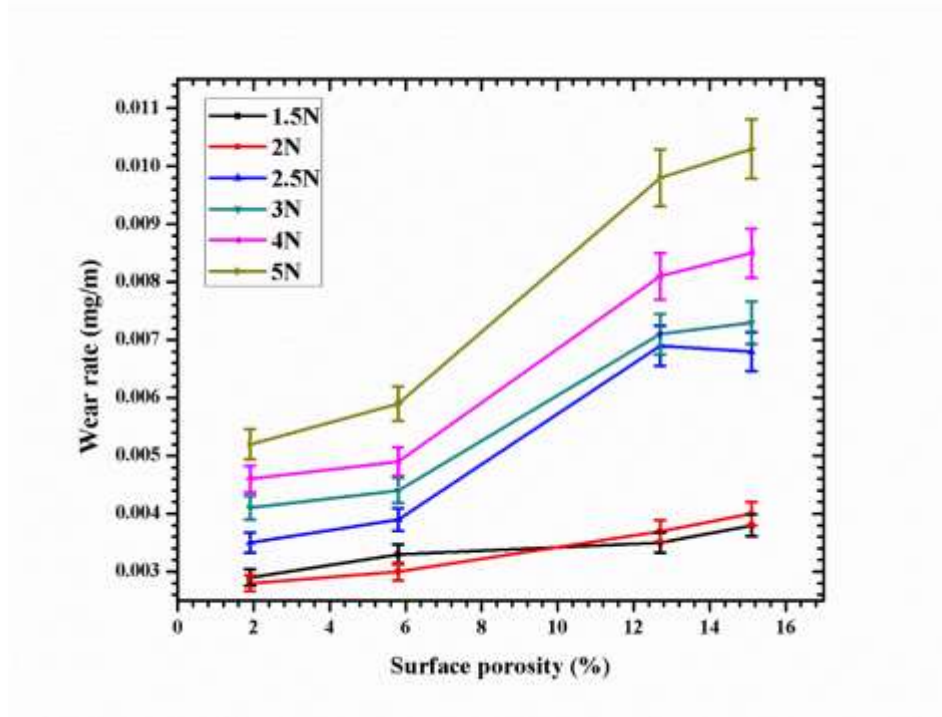


Figure 4.14 Wear rate versus surface porosity for pure Al under 10 Hz frequency

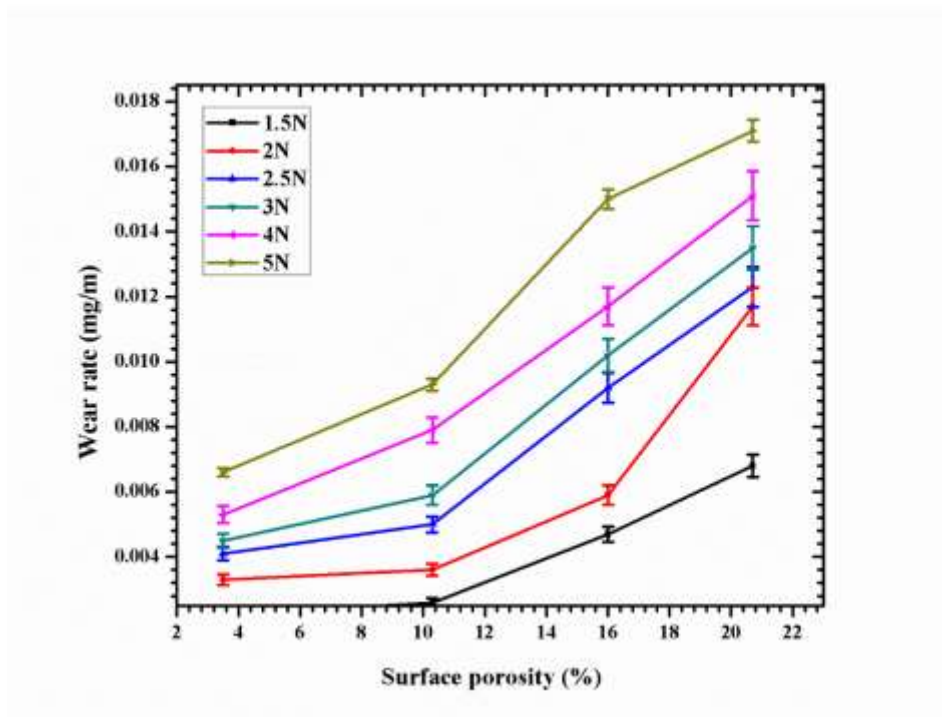
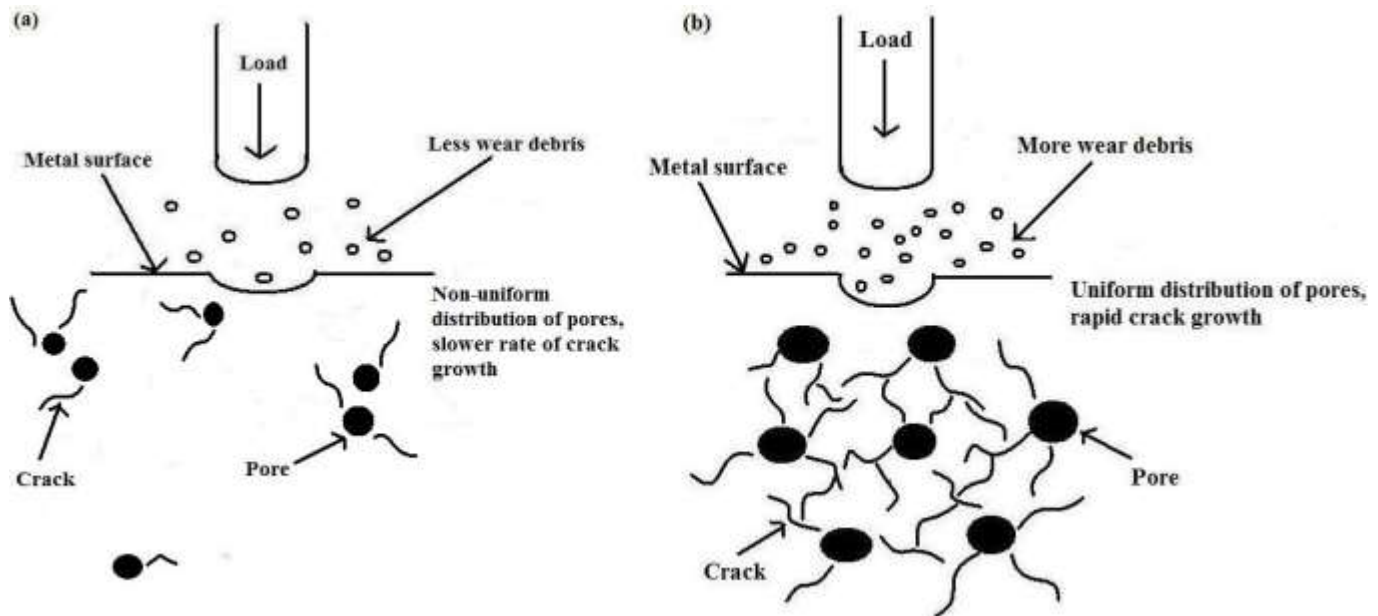


Figure 4.15 Wear rate versus surface porosity for Al 6061 under 10 Hz frequency

The effect of porosity on wear resistance depends not only on total porosity content, but also on pore distribution and connectivity. When the pores are uniformly distributed, cracks can propagate at a high rate as pores can easily link up with each other and form a wide network of cracks. This effect ultimately contributes to the fracturing of material and increasing wear rate. Pores in 6061 Al and pure Al are more uniformly distributed than A380M Al (see Figure 4.1), which may also contribute to the higher wear resistance exhibited by A380M Al. For Al 6061, wear rate increased about 30% as the surface porosity increased from 3.5% to 10.3%. Similar results (increase in wear rate with increasing porosity) were reported in the open literature [165-166]. Furthermore, with an increase in the amount of porosity, the link up of pores and the distance cracks need to travel before meeting another pore is shorter. Thus, increasing fracturing and wear. Figure 4.16 is a schematic diagram showing the effect of pore distribution on wear rate.



**Figure 4.16 Schematic diagram depicting the effect of (a) non-uniform and (b) uniform pore distribution on wear rate**

#### **4.4 Effect of Normal Load and Coefficient of Friction on Wear Behavior**

Normal load is also regarded as input weight. Two representative curves are plotted here to study the effect of normal load on wear rate. From Figures (4.17 (a), (b)), we observe that with increasing load weight loss is increased. Due to in contact area and rise in the coefficient of friction, the harder material (steel ball) will grind the softer material at a higher rate. Increasing the load also tends to cause extensive subsurface plastic deformation and crack nucleation, thus, accelerates wear rate.

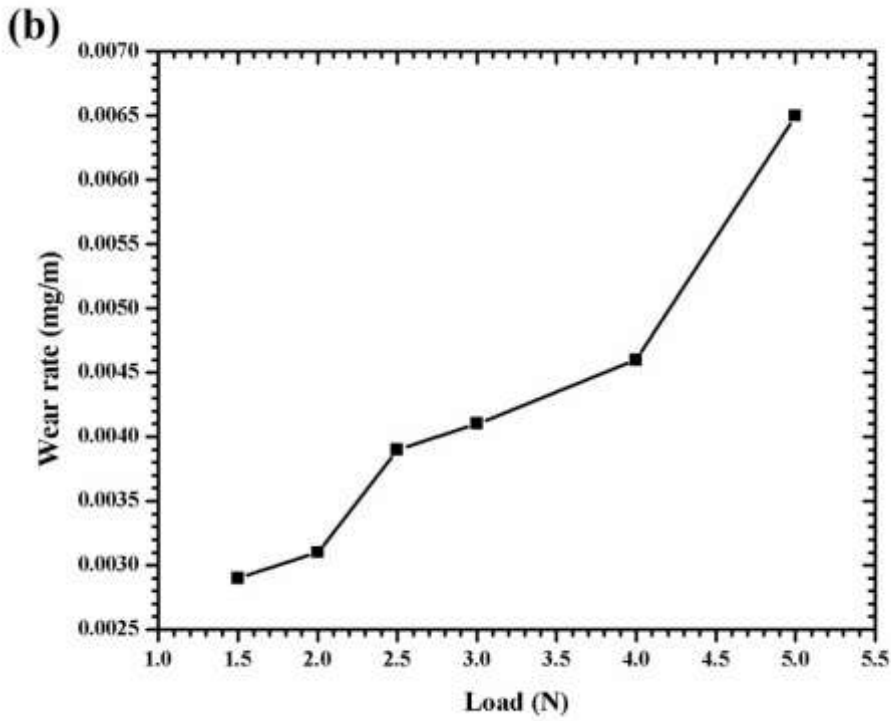
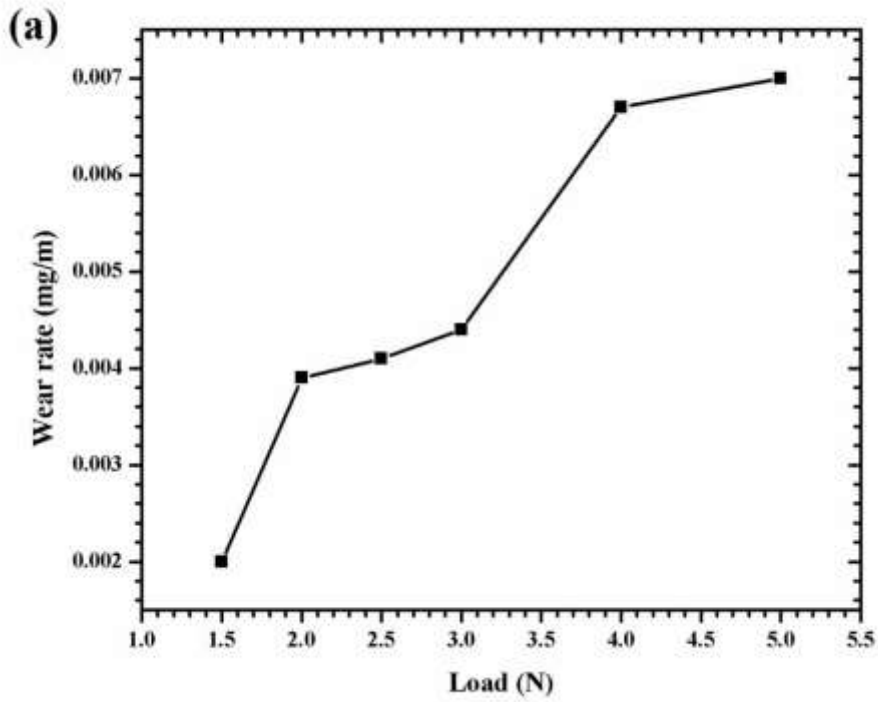
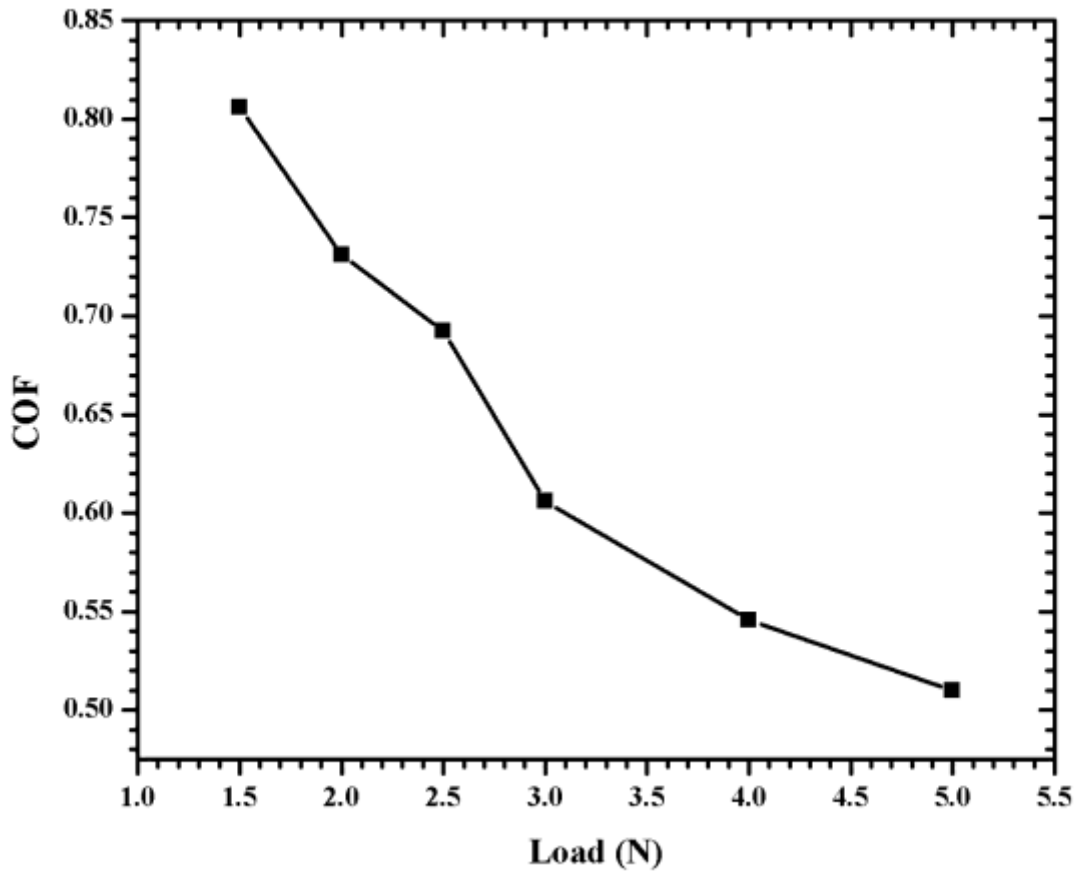


Figure 4.17 Normal load vs wear rate for (a) Al A380M alloy (b) Pure Al (1.9% porosity)

The coefficient of friction is plotted as a function of porosity in Fig.4.18. As shown in the Figure, the coefficient of friction decreases with increasing normal load. Under dry sliding conditions, the generation of frictional heat between two sliding surfaces raises the temperature at the interface. This temperature rise promotes softening of the aluminium, which in turn, lowers the coefficient of friction with increasing load.



**Figure 4.18 COF vs load for Al A380M alloy**

The coefficient of friction of the pure Al specimens containing 1.9%, 5.8%, 12.7% and 15.1% porosity were determined to be 0.41, 0.44, 0.57, and 0.63 respectively. And for Al 6061, the coefficient of friction

of the specimens containing 3.5%, 10.3%, 16.0% and 20.7% was determined to be 0.43, 0.52, 0.60 and 0.66, respectively. The correlation between coefficient of friction and surface porosity is plotted in Figure 4.19 .

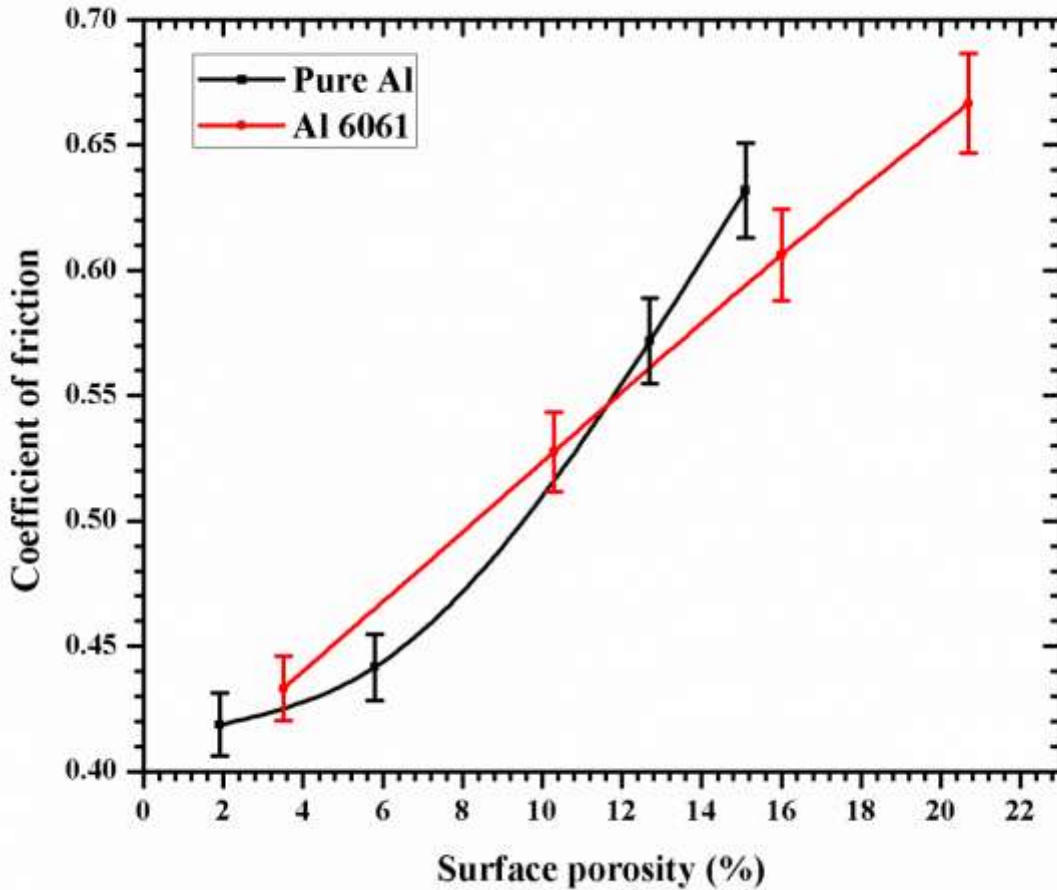


**Figure 4.19 COF vs surface porosity for pure Al and Al 6061 at 3N load**

At high porosity, the surface roughness of the material increases and consequently the possibility of the generation of wear debris increases as a consequence of asperity-asperity contact. Therefore, the rise in the coefficient of friction with increasing porosity might be attributed to the formation of more asperity-asperity contact during sliding. Yalcin [167] found similar results (increase in coefficient of friction with

increasing porosity). He further suggested that, under dry friction conditions, a decrease in the coefficient of friction results in a decrease in the mass loss of the porous material.

#### **4.5 Worn Surface Evolution**

Worn surfaces of Al A380M, pure Al and Al 6061 specimens were analyzed using optical profilometer and scanning electron microscopy. Figures 4.20, 4.21 and 4.22 represent optical profilometer scans of wear tracks of all three different materials at 3, 4 and 5N load (starting from the left) and 10 Hz frequency. It is important to underline here that the depth of the wear tracks varied significantly in each sample with increasing load. At 5N load and 10 Hz frequency, the depth of the Al A380M alloy was 110 $\mu$ m which is 22% higher than 3N load with same frequency. Due to low weight loss in pure Al in comparison to Al 6061, wear track depths were shallower than those of Al 6061 specimens. At 5N load and 10 Hz frequency, the wear track depth of pure Al having higher amount surface porosity (15.1%) show 83% increase in depth as compared to lower porosity (1.9%). On the other hand, for Al 6061, having higher amount of surface porosity (20.7%) exhibits 90% increase in depth compared to lower porosity (20.7%).

The variation in volume loss with applied normal load (calculated from profilometry scans) is plotted in Figure 4.23 (a) and (b). The curve shows a somewhat linear relation between normal load and volume loss for a given porosity level. The volume loss increased with increasing porosity as expected. As discussed earlier wear resistance increases as hardness increases. At low load (1.5N) for Al 6061, the volume loss increases by 42% as porosity increases from 3.5% to 10.3%. However, at high load (5N) the difference in percent volume loss (46%) is over 2 times higher than low load.

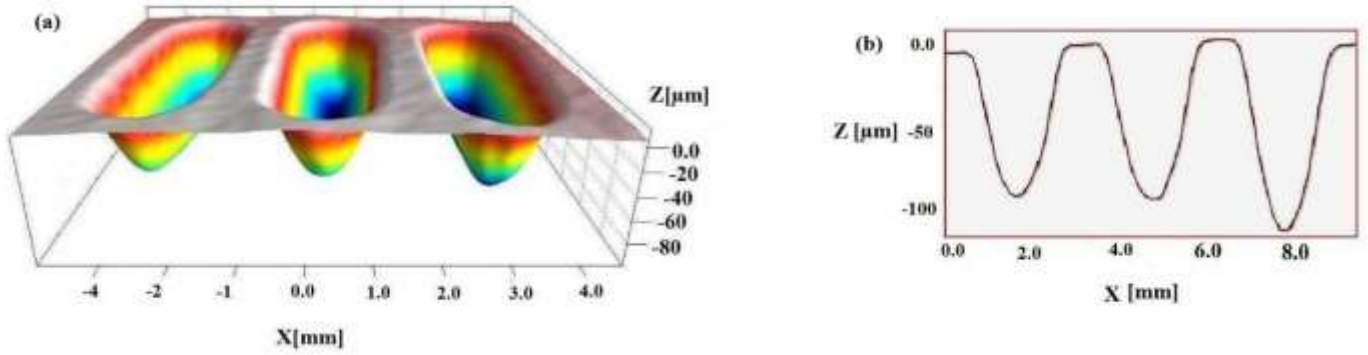


Figure 4.20 Optical profilometry scans of wear tracks; (a, b) Al A380M at 3, 4 and 5N load and 10 Hz frequency.

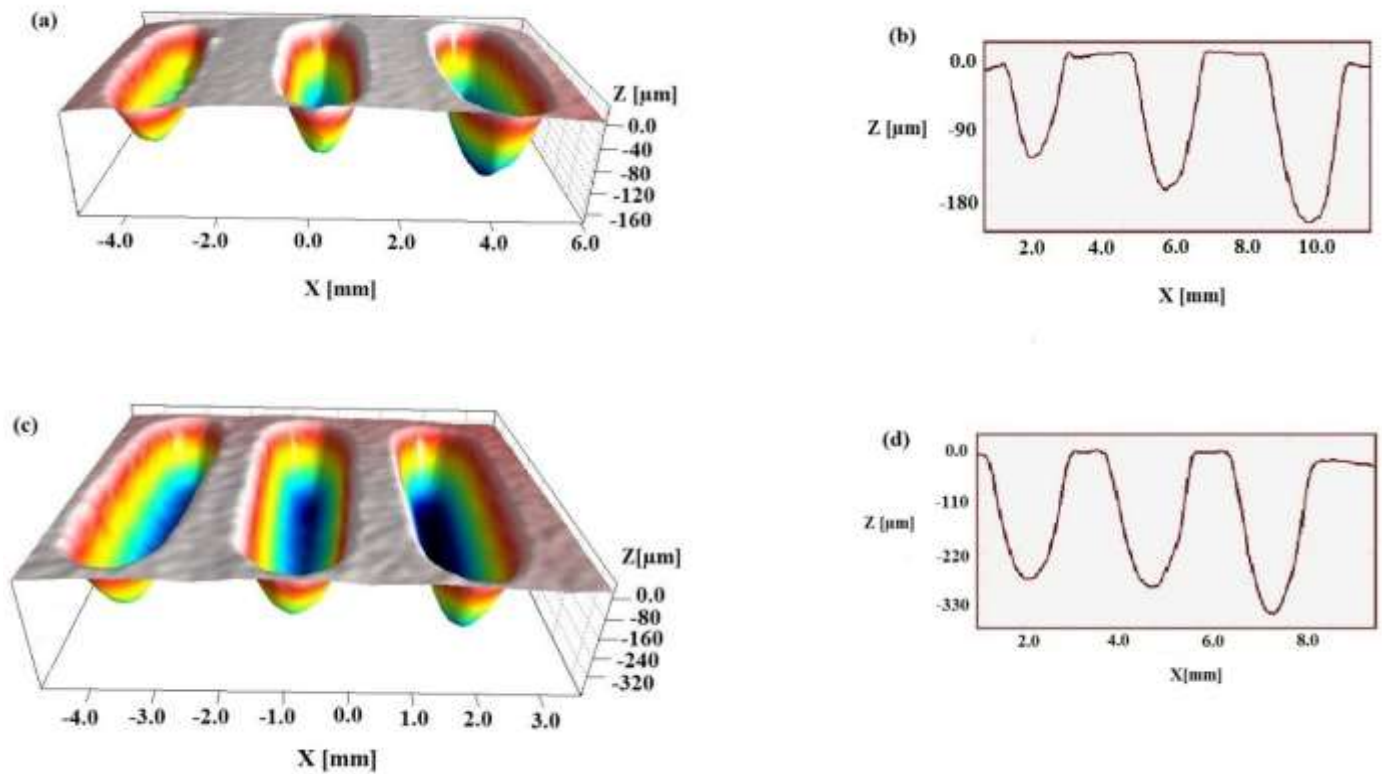


Figure 4.21 Optical profilometry scans of wear tracks; (a, b) pure Al (1.9% porosity) and (c, d) (15.1% porosity) at 3, 4 and 5N load and 10 Hz frequency.

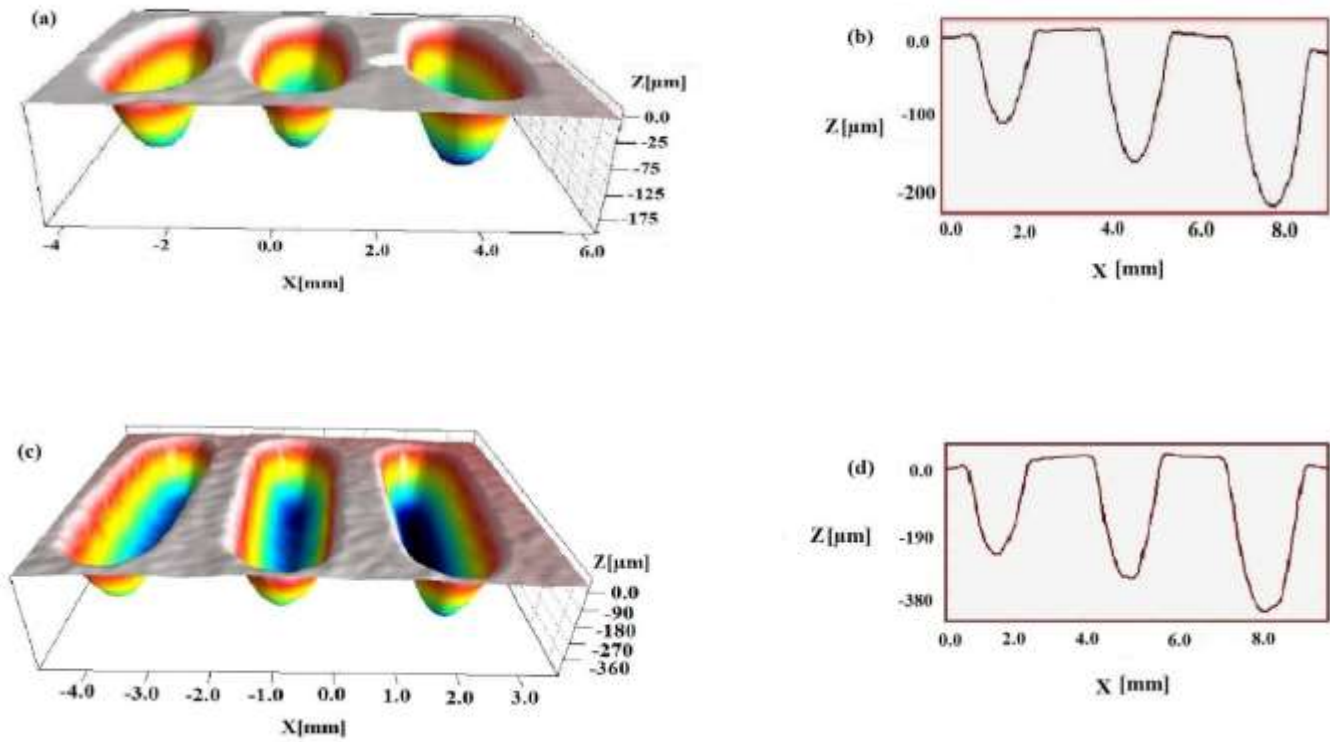


Figure 4.22 Optical profilometry scans of wear tracks; (a, b) Al 6061 (3.5% porosity) and (c, d) (20.7% porosity) at 3, 4 and 5N load and 10 Hz frequency.

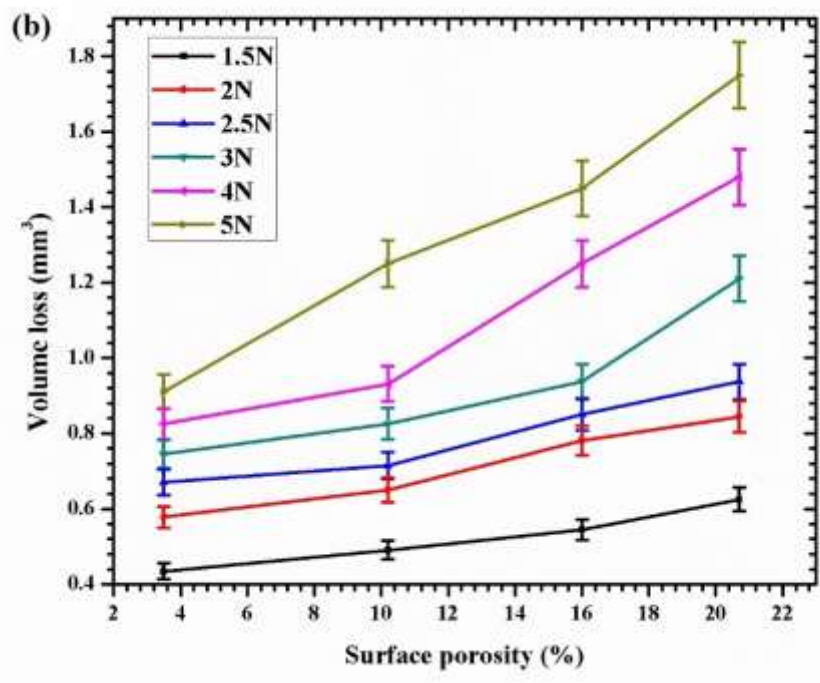
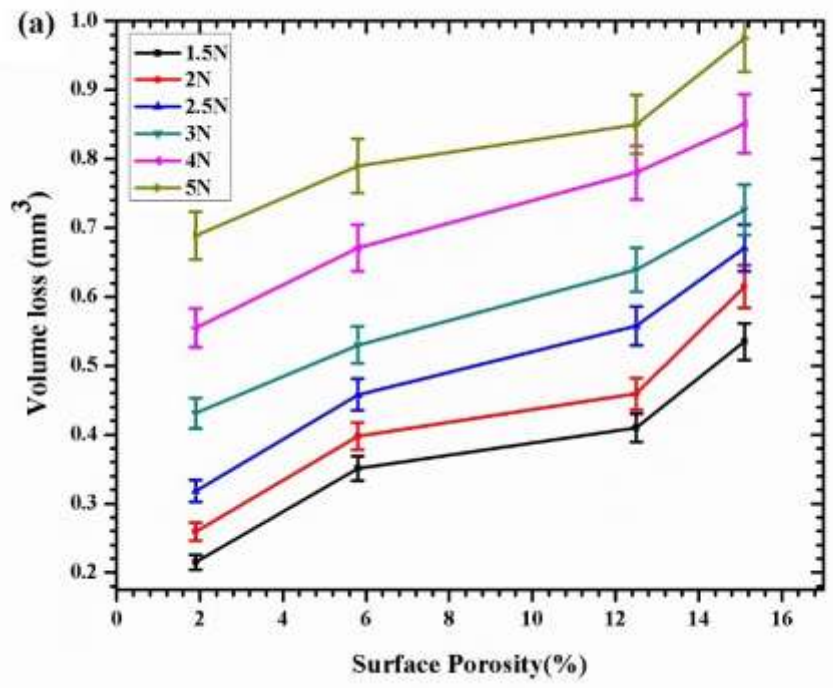
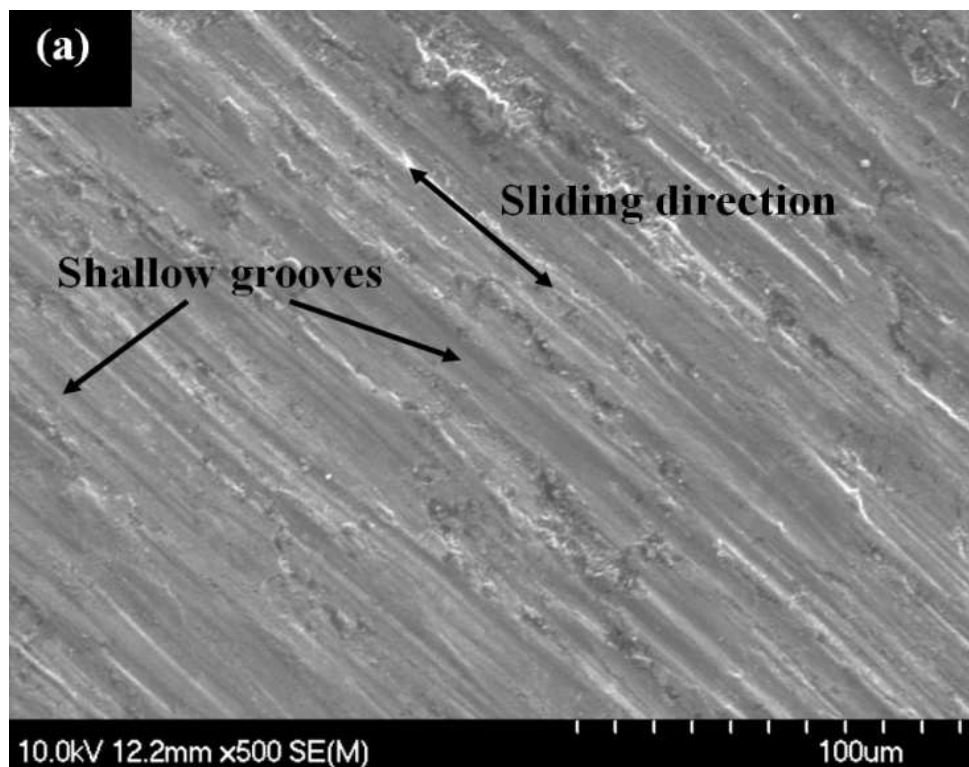
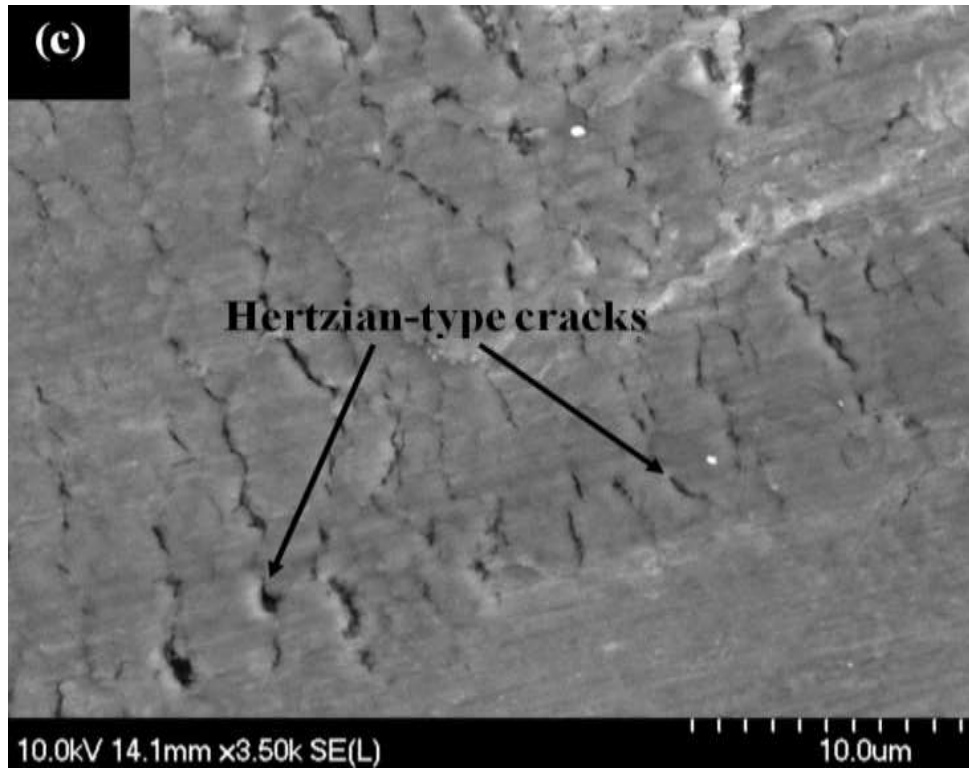
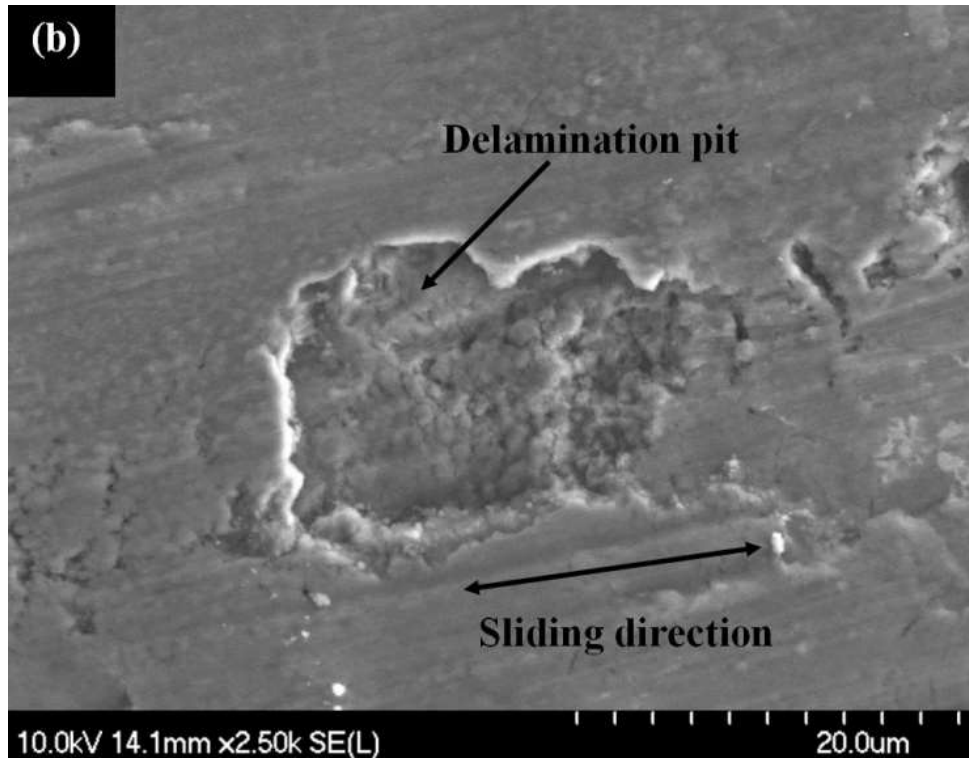


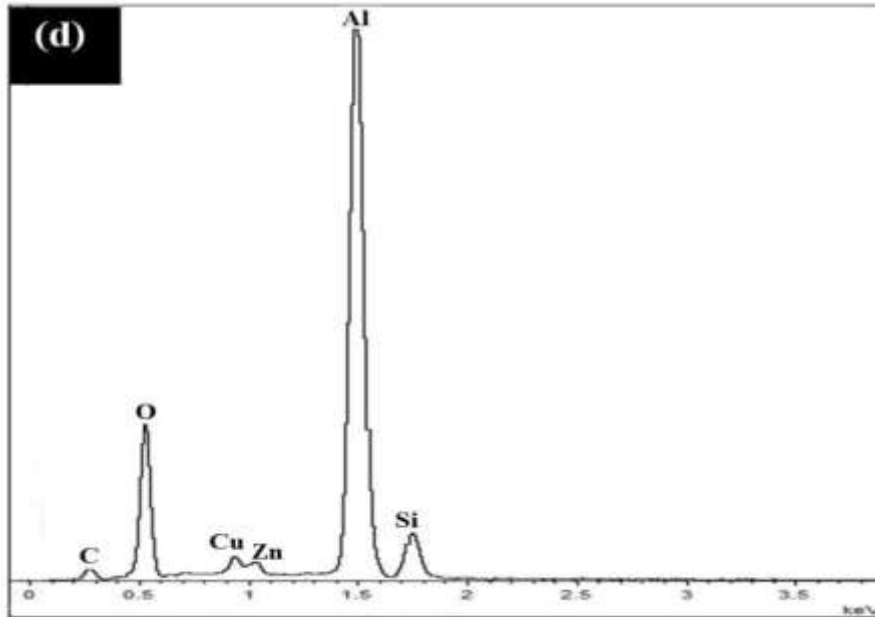
Figure 4.23 Volume loss vs surface porosity for (a) pure Al and (b) Al 6061

Figure 4.24 represents the worn surface of as received Al A380M specimen at 2.5N load and 10 Hz frequency. Two wear mechanisms have been identified from SEM as dominant mechanisms during dry sliding wear of Al A380M aluminium alloy, namely, abrasion and delamination. Abrasion plays a significant role in the process as depicted by the shallow grooves along the wear track (Figure 4.24 (a)). These grooves extend parallel to the sliding direction. Such features are characteristics of abrasion, in which hard asperities of the steel counterface plough through the Al specimens.

A second mechanism contributing to the observed wear is delamination. Plastic deformation leads to changes in the microstructure of the subsurface, making the material unstable to local shearing causing delamination [168]. Delamination wear occurs as a result of subsurface nucleation of cracks at pores and propagation of these cracks. Pores serve as the origin and end of crack propagation, hence reducing the required length of crack propagation. Figure 4.24 (b) shows evidence of delamination as a result of plastic deformation of the surface. Hertzian-type cracks were also observed on the worn surface as a result of surface tensile stresses that evolve during Hertzian contact (Figure 4.24 (c)). These types of cracks normally extend perpendicular to the sliding direction.



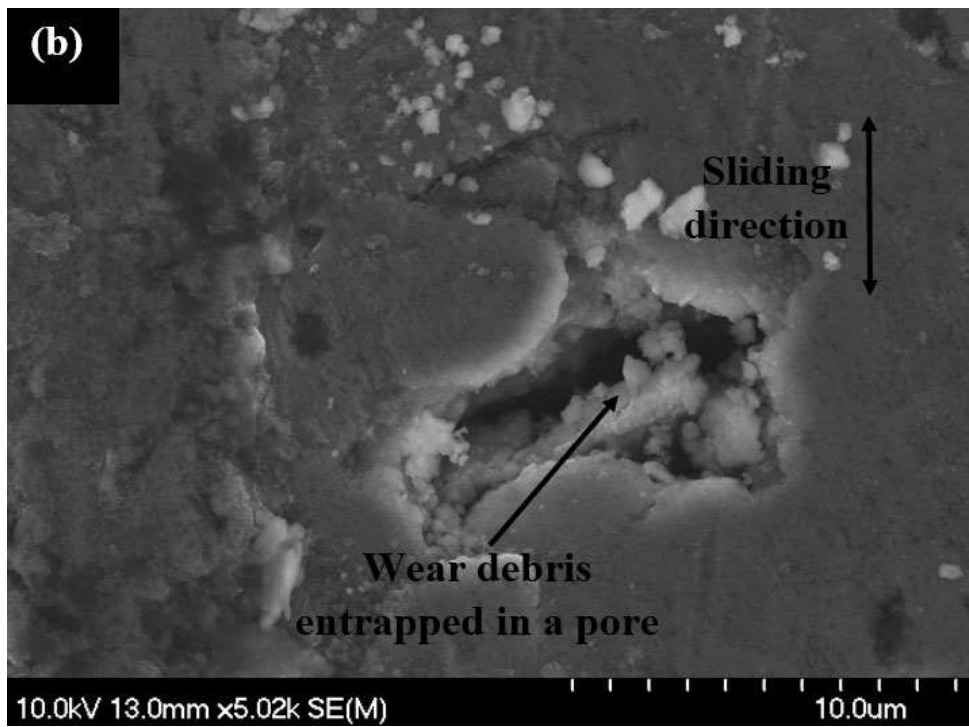
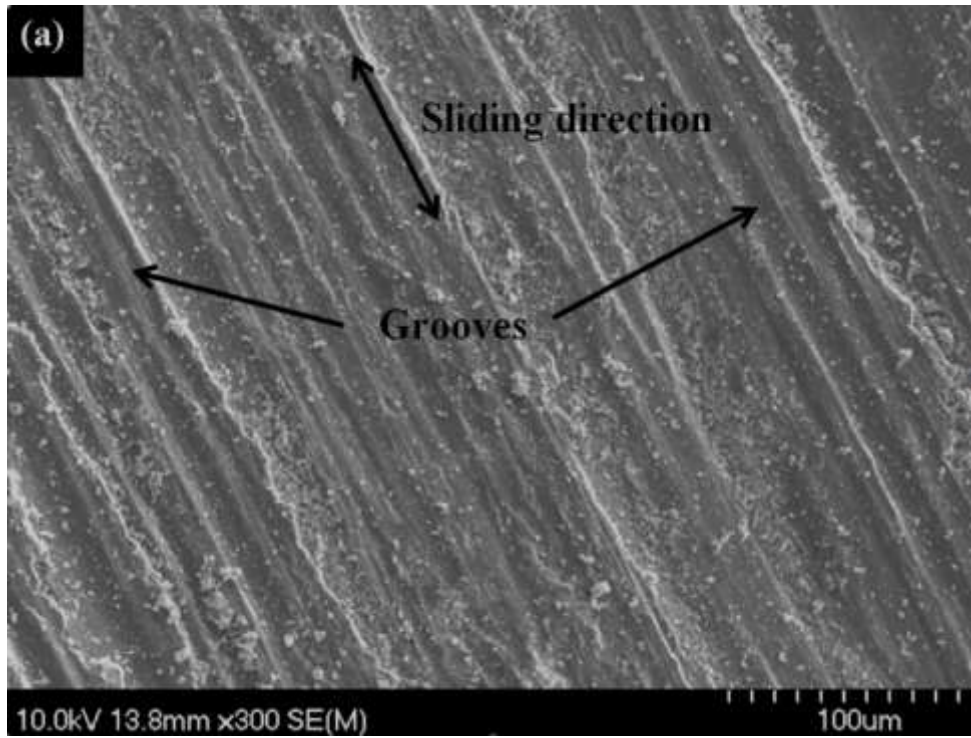




**Figure 4.24 SEM micrographs of worn surface (a,b,c) and (d) EDS analysis of wear track for Al A380M alloy**

EDS analysis was conducted on the worn surface of Al A380M alloy and is shown in Figure 4.24 (d). EDS confirmed that the worn surface contained a considerable amount of oxygen. The presence of oxygen on the worn surface is indicative of oxidative wear. As sliding takes place, the increase in temperature at the interface promotes the formation of oxides. Absence of Fe implies that, there is no material transfer from the counterface (AISI 52100 bearing steel ball). As a result, mechanical mixing of materials did not take place between the two sliding surfaces. Figures 4.25 and 4.26 show wear surface morphologies of pure Al and Al 6061 specimen containing 15.1% and 20.7% porosity, respectively, under 2.5N load and 10 Hz. The wear tracks of the samples were characterized by surface deformation and heavy damage in the form of longitudinal grooves extending parallel to the sliding direction which are clearly observed in Fig.4.25 (a) and Fig.4.26 (a) as evidence of abrasion. This process of material removal from the surface via plastic deformation during abrasion occurs by ploughing. As a result of plastic flow of the soft Al matrix, ploughing results in a series of grooves [169]. The material loss caused by this damage resulted in deepening and widening of wear tracks [170]. In the ploughing process, Al is displaced from a groove to the sides. During ploughing, ridges form along the sides of the ploughed grooves regardless of whether or not wear particles are formed. These ridges become flattened and eventually fracture after repeated loading and unloading cycles.

Based on the experimental observations in this study, several factors can be identified that affect wear resistance of the sintered Al specimens, namely the amount of porosity, pore size, shape, hardness and operating conditions (load and frequency). As pore edges represent stress concentration areas they tend to rupture with the reciprocating motion of the slider [171]. This is apparent from the cracks extending near the pores shown in Fig.4.25 (d) and Fig.4.26 (b). Hertzian-type cracks were also observed on the worn surface of pure Al specimens which is clearly visible from Figure 4.25(c). The pores in the Al specimens act as the preferential sites for the wear debris to agglomerate. At the same time, grooves are generated in the surface along the sliding direction. The debris generated between the sliding surfaces will be pushed into the grooves and pores. As the wear tests were conducted under low loading condition, the amount of wear debris formed were very low. Some of the debris were entrapped into the grooves and pores and some were remained between the sliding surfaces which is clearly visible from Figure 4.23 (b). Some of the wear debris particles which were entangled between the sliding surfaces were repeatedly fractured and oxidized. The fracture of debris continuously exposed more fresh metal to the environment, which promotes oxidation reaction.



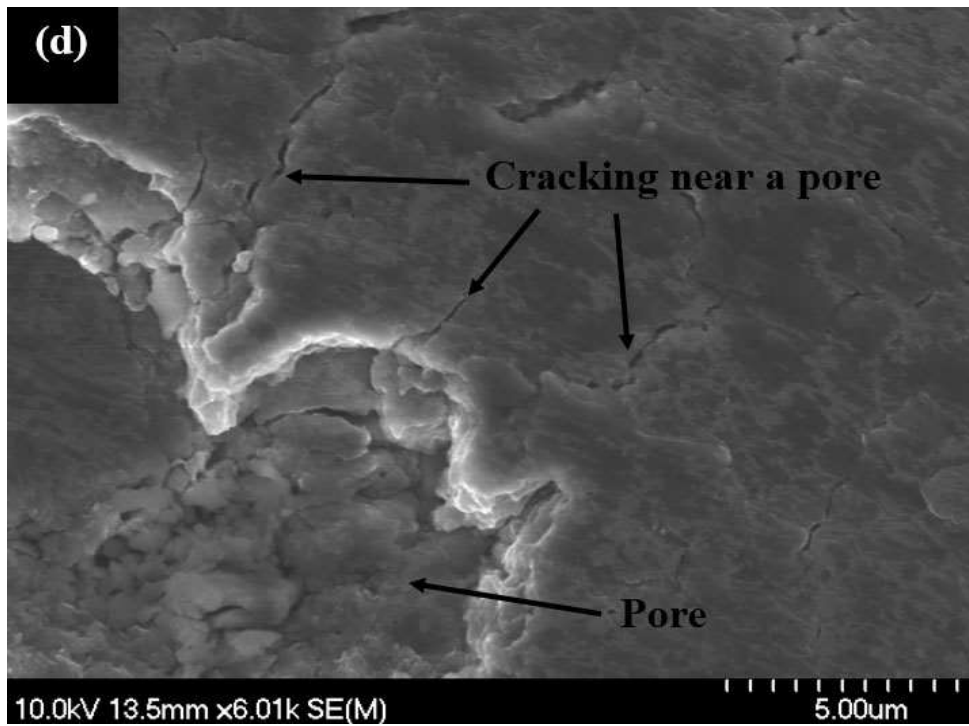
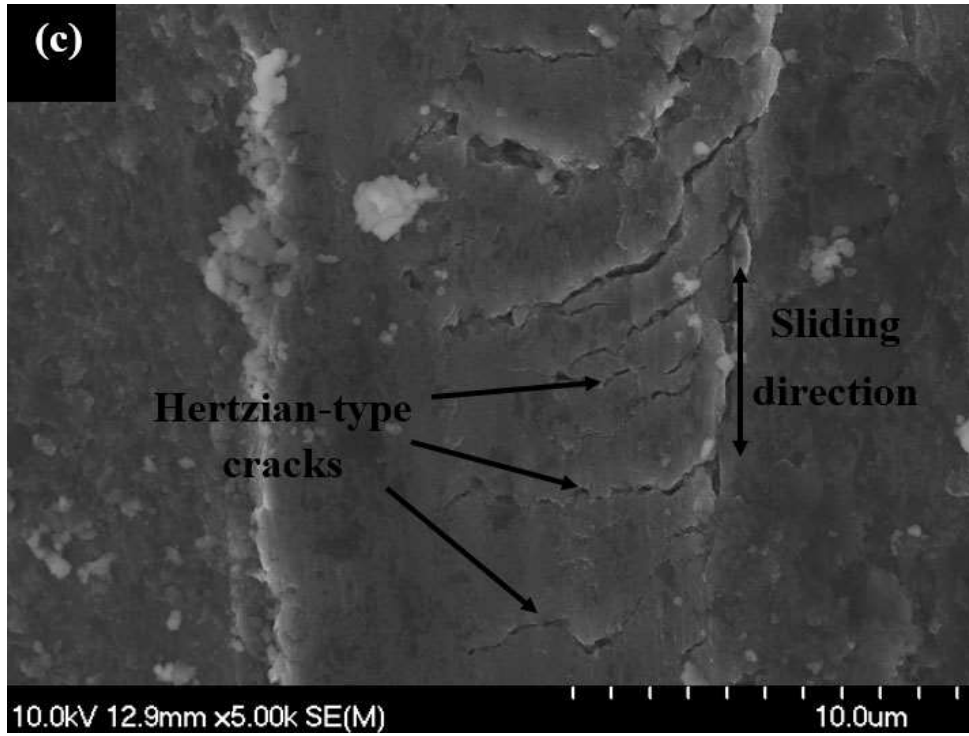
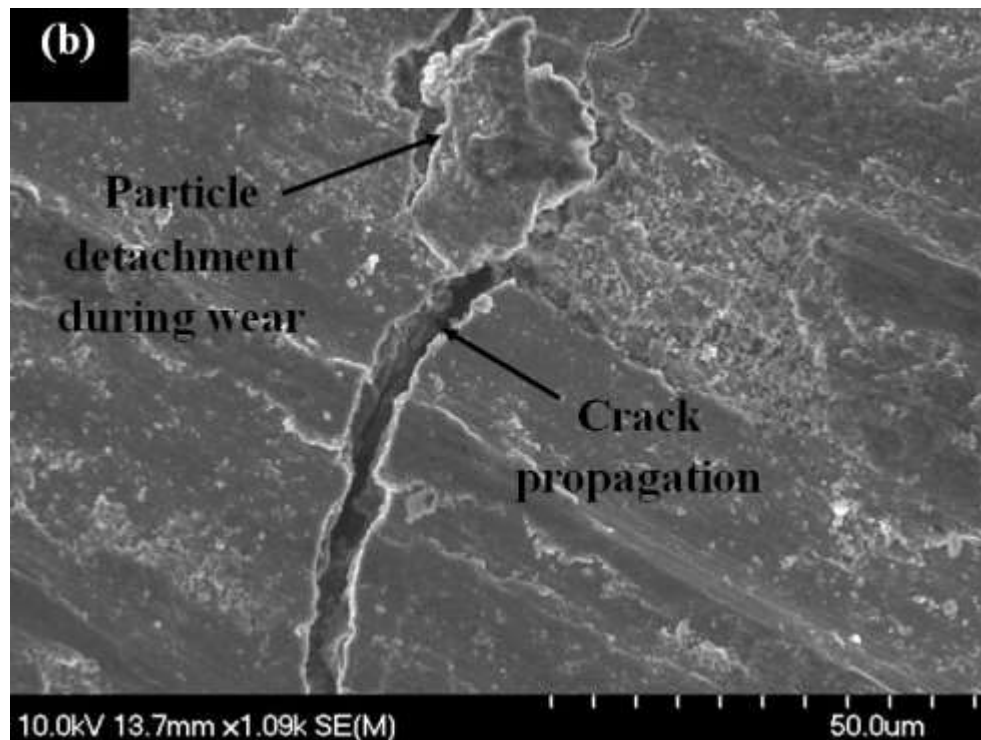
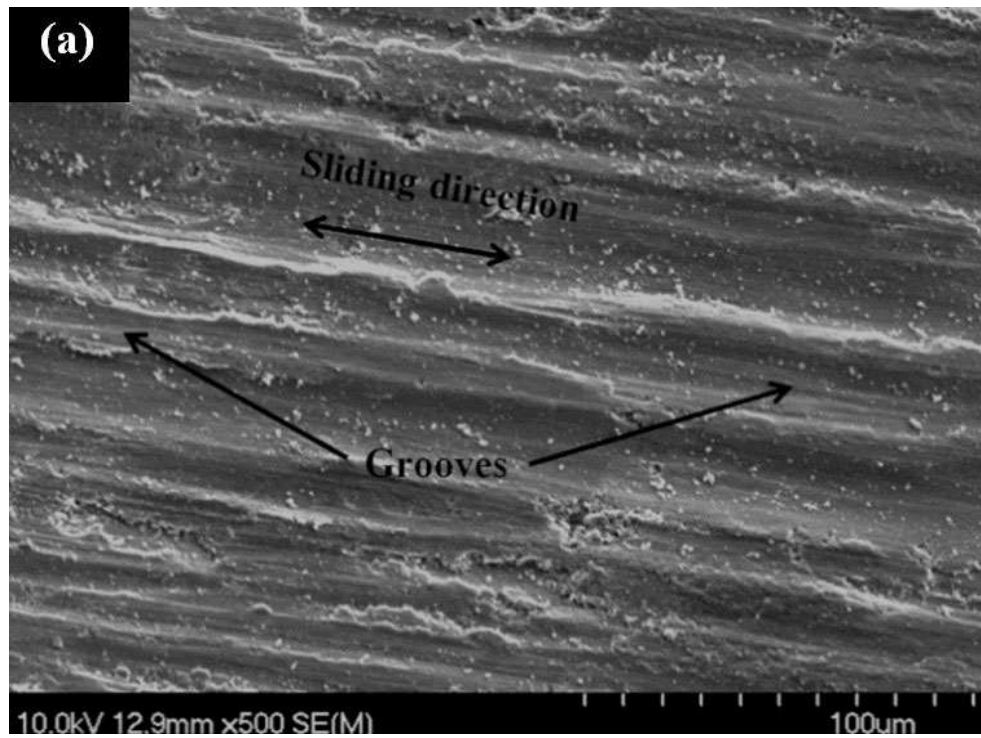


Figure 4.25 SEM images of worn surface (a,b,c,d) for porous pure Al



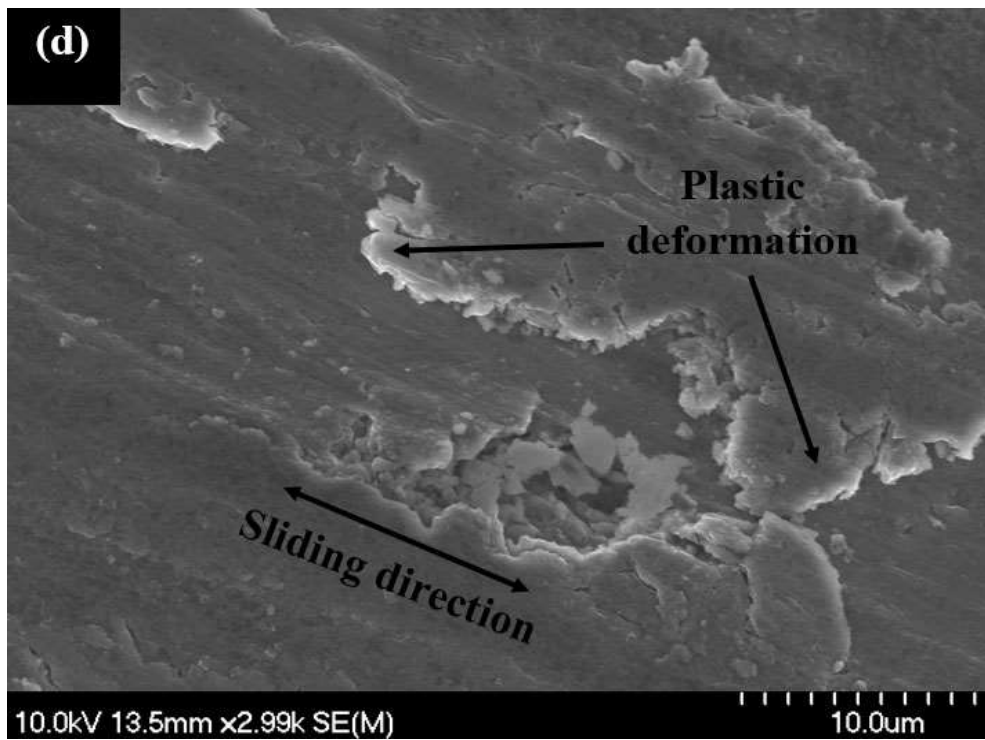
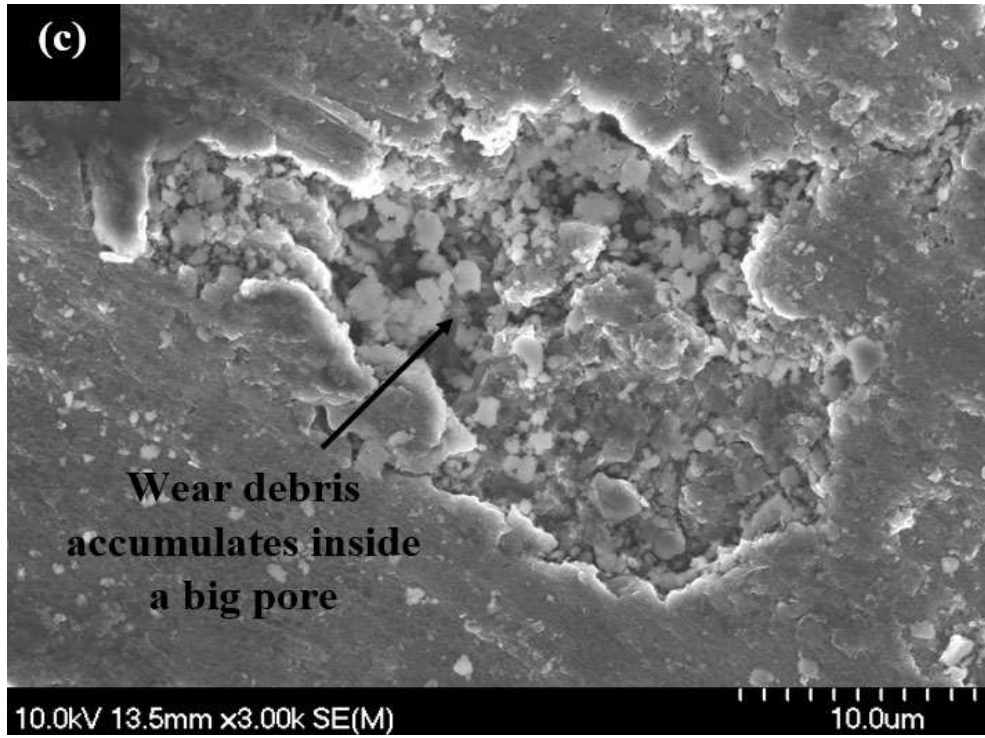
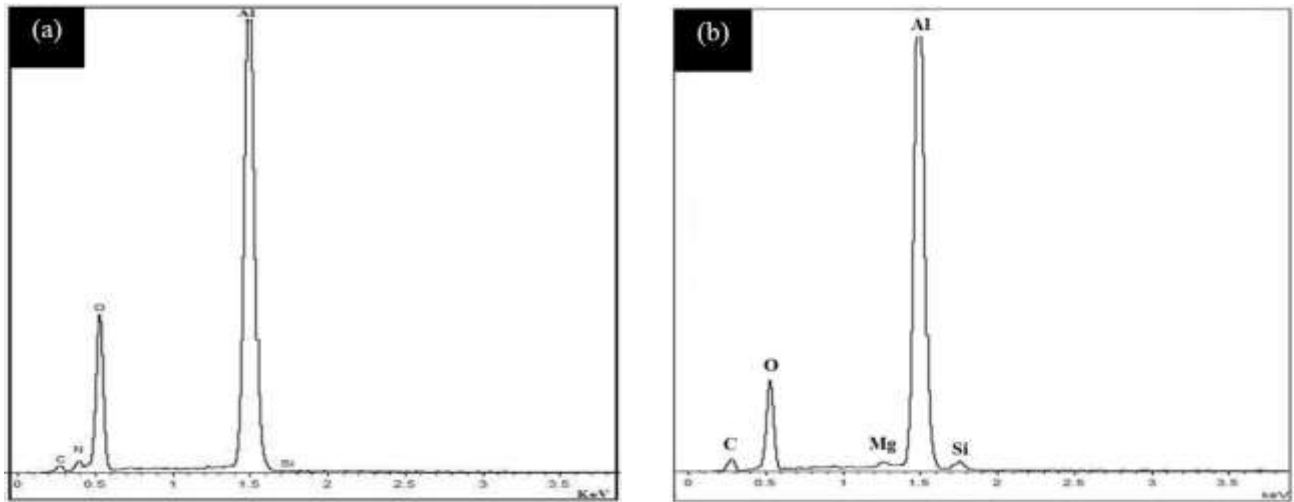


Figure 4.26 SEM images of worn surface (a,b,c,d) for porous Al 6061 alloy



**Figure 4.27 EDS analysis of wear tracks for (a) pure Al and (b) Al 6061 alloy**

EDS analysis was also performed on the worn surface of pure Al and Al 6061 specimens and is shown in Figure 4.27. This analysis shows signs of oxidative wear as in Al A380M alloy and no indication of material transfer from the steel counterbody. The size and shape of wear debris were analyzed using scanning electron microscopy and is shown in Figure 4.28. It is clearly seen that wear debris generated from pure Al are smaller in size than those generated from Al 6061. This might be due to the fact that pure Al exhibits smaller pore size and smaller initial pre-sintering particle size. The difference in wear debris size between pure Al and Al 6061 explains why the grooves on the wear track of pure Al are narrower than those of Al 6061 (Figures 4.25(a), 4.26(a)) as wear debris of different sizes slide on the surface of the Al specimens. Abrasive wear seems to be the contributing wear mechanism operating under the current conditions. That is, as porosity increases, surface roughness increases which gives rise to generation of large number of wear debris which in turn accelerates third body abrasion.

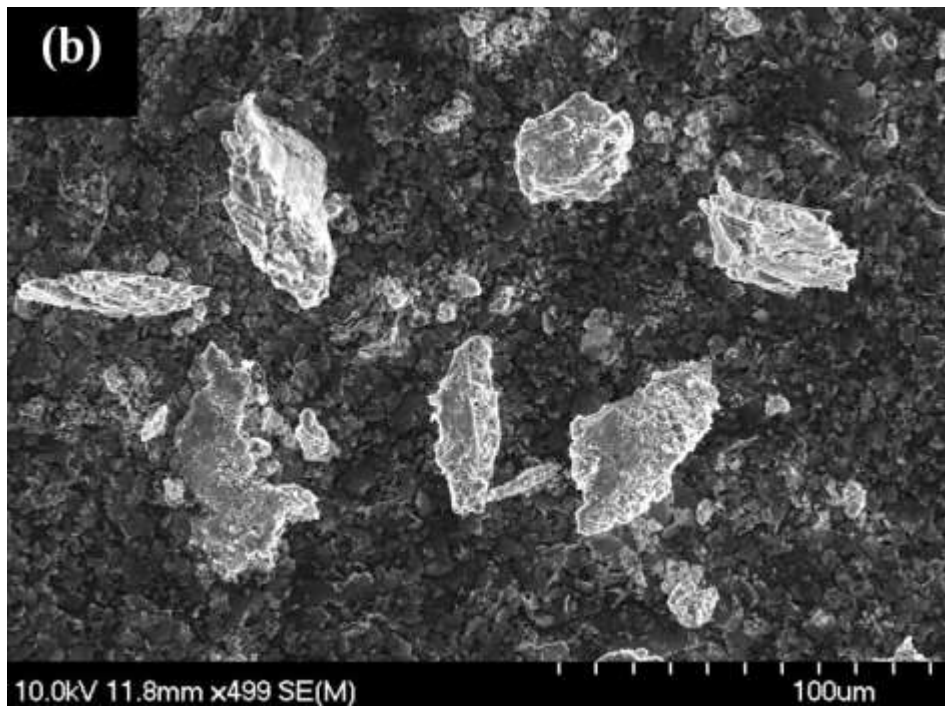
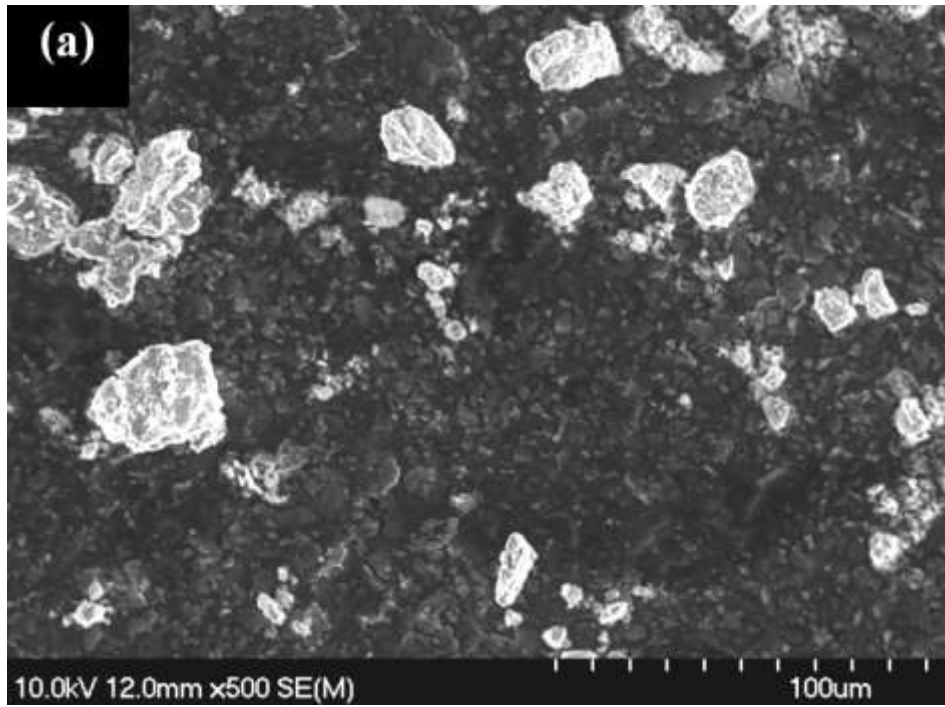


Figure 4.28 Wear debris at 2.5N load and 10 Hz a) pure Al b) Al 6061

#### 4.6 Scratch Behavior of Porous Pure Al and Al 6061

Scratch profile examination under the SEM provide much insight into the scratching behavior of the porous Al samples. Scratch width was measured from the SEM micrographs in order to compute the scratch hardness. It was observed that, scratch width was different for Pure Al and Al 6061 specimens along the length of the scratch. The scratch hardness is calculated using simple equation [172],

$H_s = 8W/\pi b^2$ , where W is the normal load, b is the scratch width. This equation can be converted into a convenient scratch hardness number (GPa) given as [173]:

$$H_s = 24.98m/x^2 \quad \text{Equation 4.2}$$

Where m is the normal load in grams and x is the width in  $\mu\text{m}$ . We can observe that the scratch width is the remarkable indicator for investigating the material resistance against the scratch deformation. As the scratch width of porous Al 6061 specimen is larger than porous pure Al specimen, the scratch hardness was lower in Al 6061 (Table 4.8).

**Table 4.8 Scratch test data for porous pure Al and Al 6061**

% Surface porosity	Scratch width ( $\mu\text{m}$ )	Scratch length (mm)	Scratch hardness(MPa)	Volume loss ( $\text{mm}^3$ )
Pure Al (1.9)	150	5	1	0.002
Pure Al (15.1)	210	5	0.5	0.004
Al 6061 (3.5)	160	5	0.9	0.003
Al 6061 (20.7)	240	5	0.4	0.007

The normal hardness obtained from the nanoindentation test is the resistance of material against local deformation created vertically by penetrating indenter, whereas scratch hardness is the response of material under dynamic deformation of the surface which is caused by the interfacial friction between the indenter and the material [174].

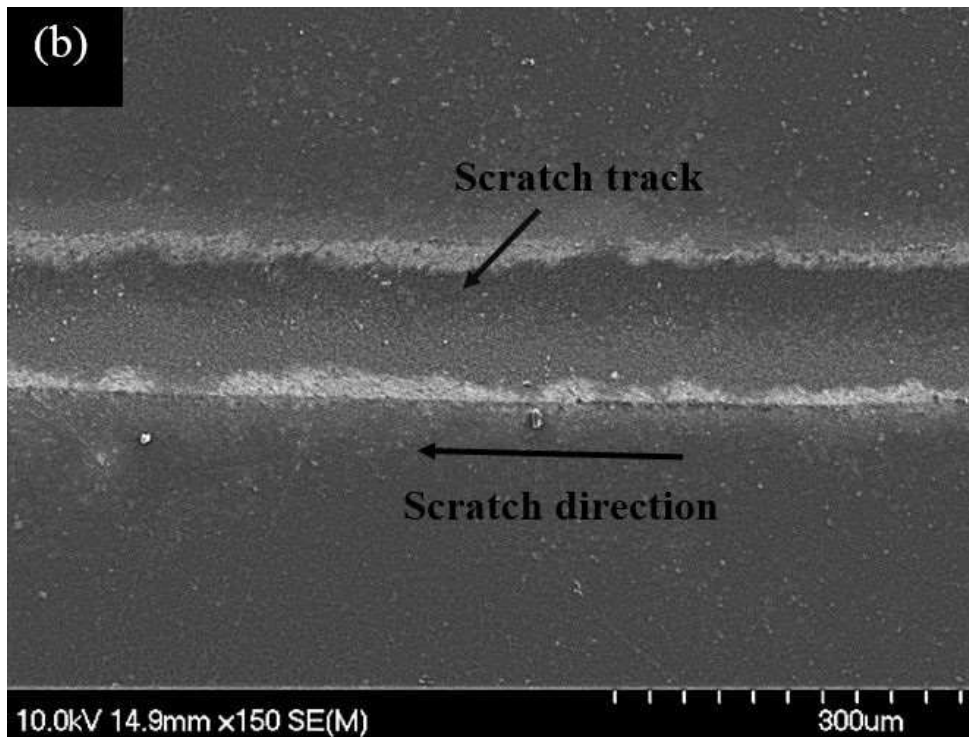
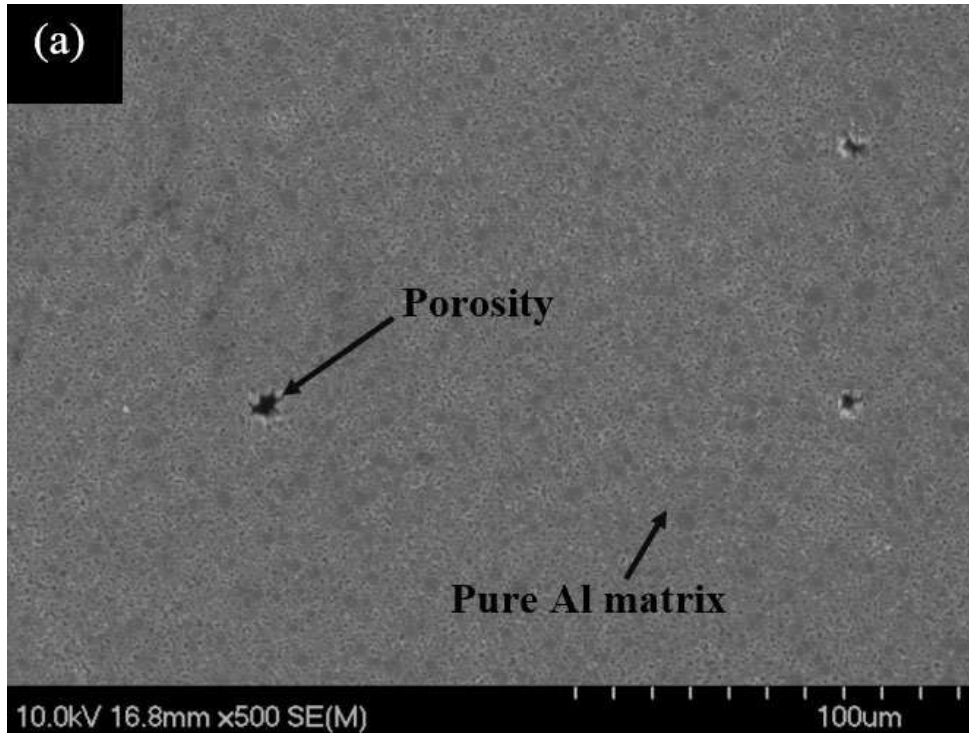
The assessment of scratch images show that the material pile up around the scratch is different in samples of different porosity levels. Porous samples have the highest pile up while the smallest pile up is for the non-porous samples. Due to the material pile up along the scratches, slightly different values in the scratch

widths were obtained, consequently at least 10 measurements of the scratch widths were taken along the scratch line and the average value for each scratch was used.

Due to the nature of the scratch process, the groove starts at very low depth, increases until reaching a maximum depth at the center of the scratch path and then gradually decreases in depth for the remainder of the scratch. The damage is minimal at the entry and exit of the scratches, while more intense damage is seen in the central region of the scratch.

When considering the low porosity samples, the contours of the scratches are shallower than porous samples. Figure 4.29 (b) shows only a small amount of material being pushed upwards at the edges of the scratch and in front of it. The volume of material removed for scratches of similar length increases with increasing porosity. In general, highly porous aluminium contains large pores. Large pores increase the relative volume of material removed during each scratch. More volume is removed during a scratch by plucking single grains. Material removal volume is higher in large grain samples. This is another consequence of the volume associated with the dislodgement of isolated large grains along the scratch edges. Large grain samples show faster increase in material removal volume due to earlier onset of lateral cracking.

At low porosity, specimens of pure Al and Al 6061 show no significant changes in scratch width, as a result there was no noticeable effect on the scratch hardness. The scratch depth and width of the less porous specimens were shallower and narrower than those of porous specimens, which may be attributed to the increased plastic resistance of the less porous specimen. No significant damage was observed in the low porosity specimens of pure Al and Al 6061. In both case, sharp cracks (Fig. 4.29(d), 4.30(c)) were generated inside the Al matrix. For pure Al, a small amount of fracture and for Al 6061 particle detachment were observed on the scratch tracks (Fig.4.29 (d) and 4.30(d)). Since the hardness of the diamond tip used in the scratch test was much harder than the ball which was used in the wear test as a counterface, grooves formed were much sharper.



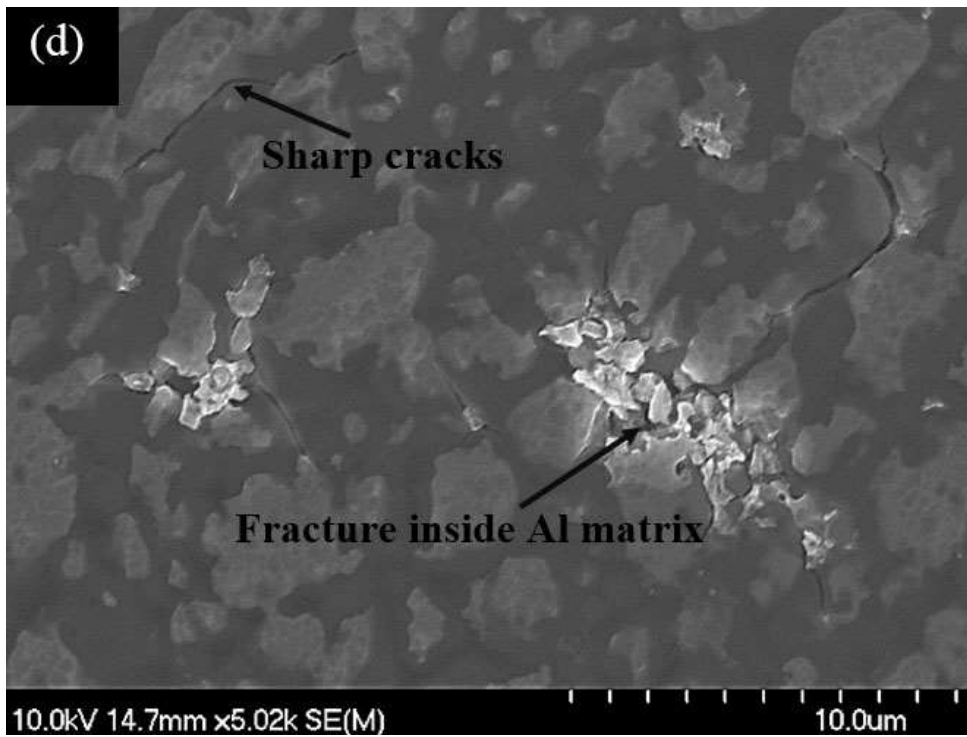
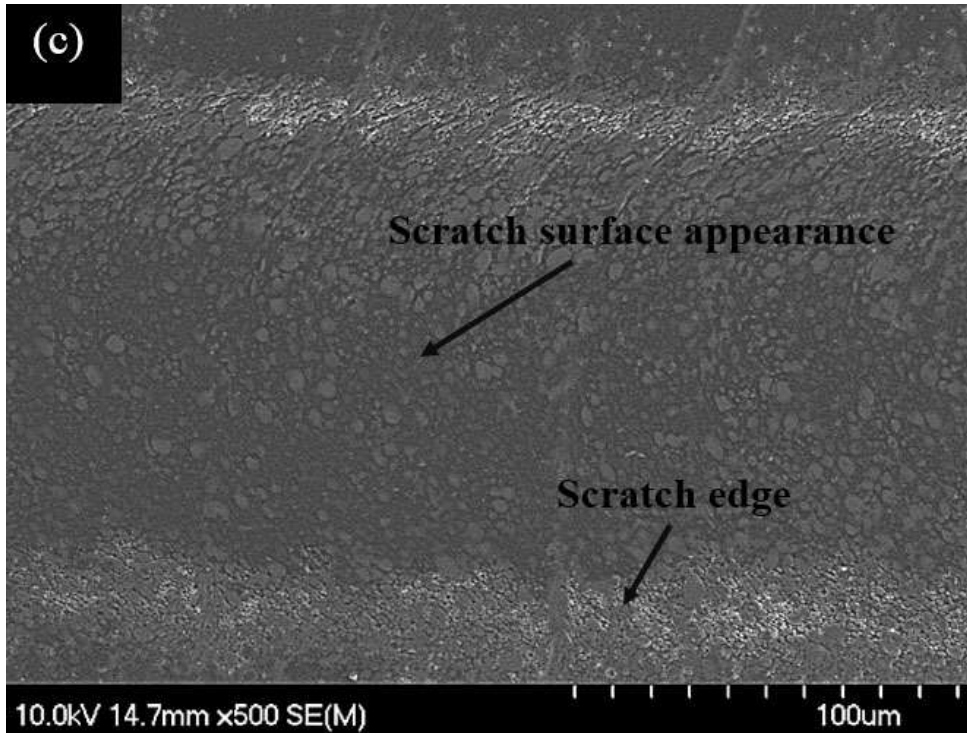
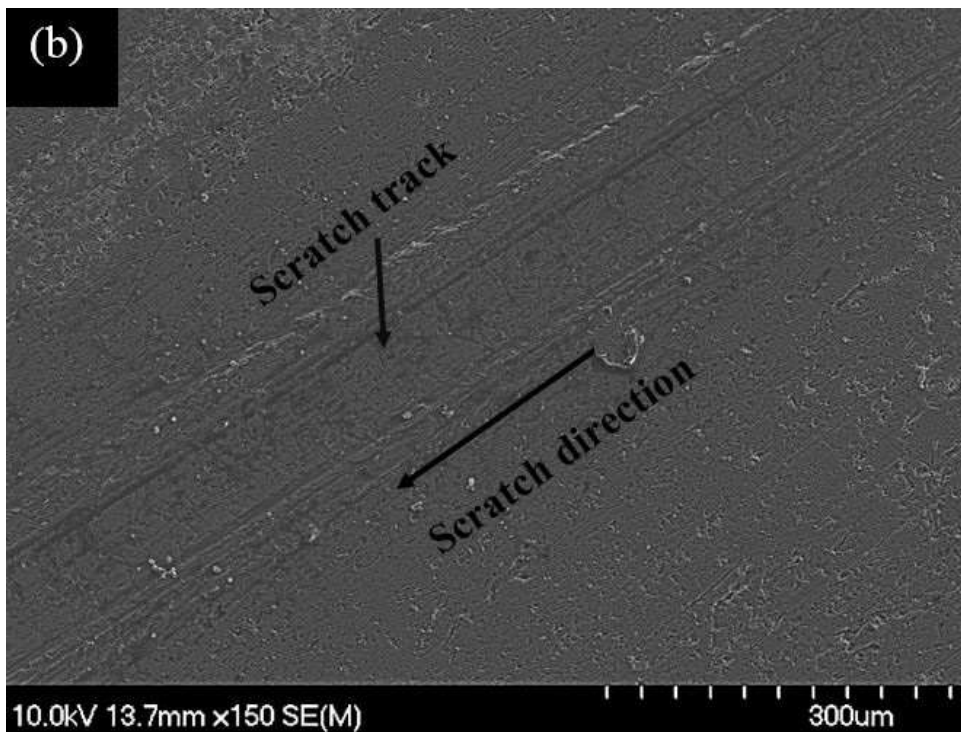
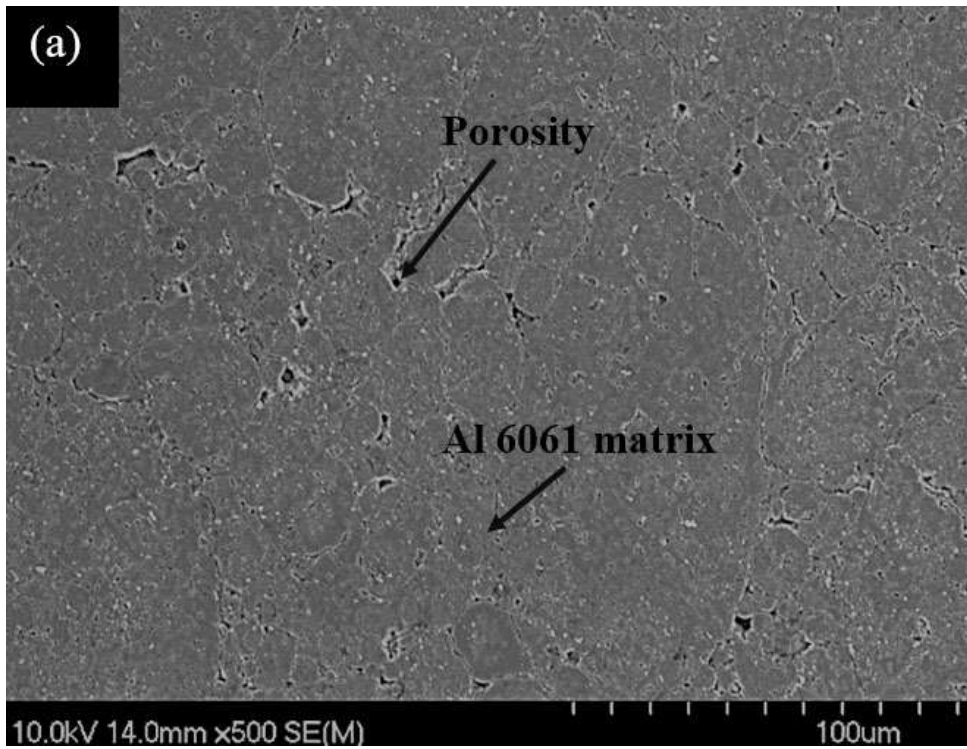


Figure 4.29 SEM micrographs of scratch track (a,b,c,d) for pure Al (1.9% porosity)



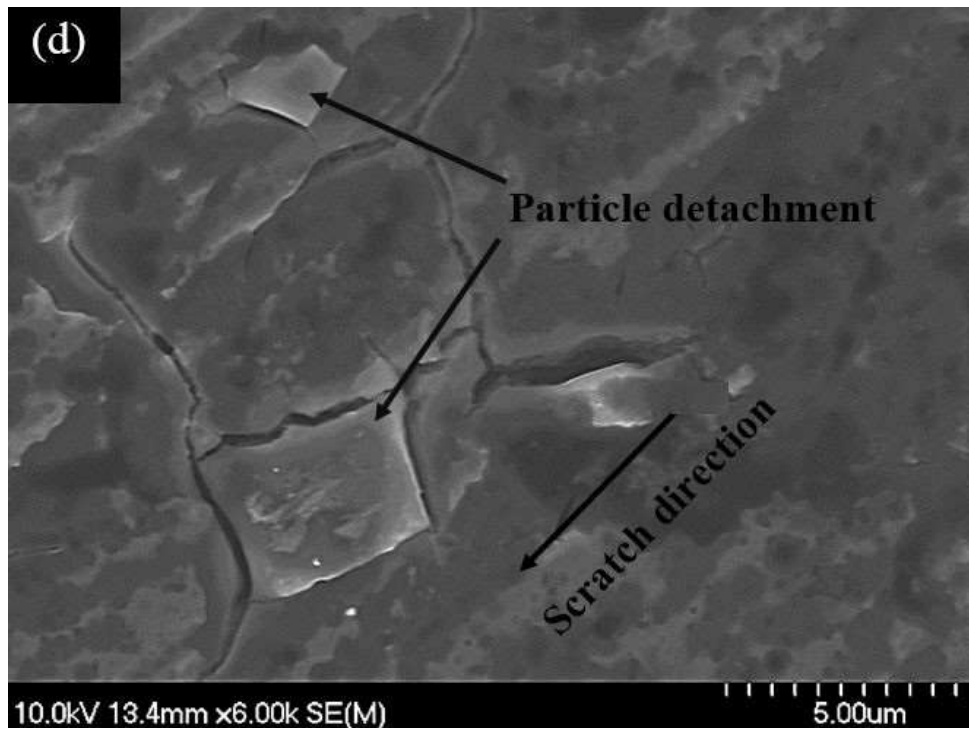
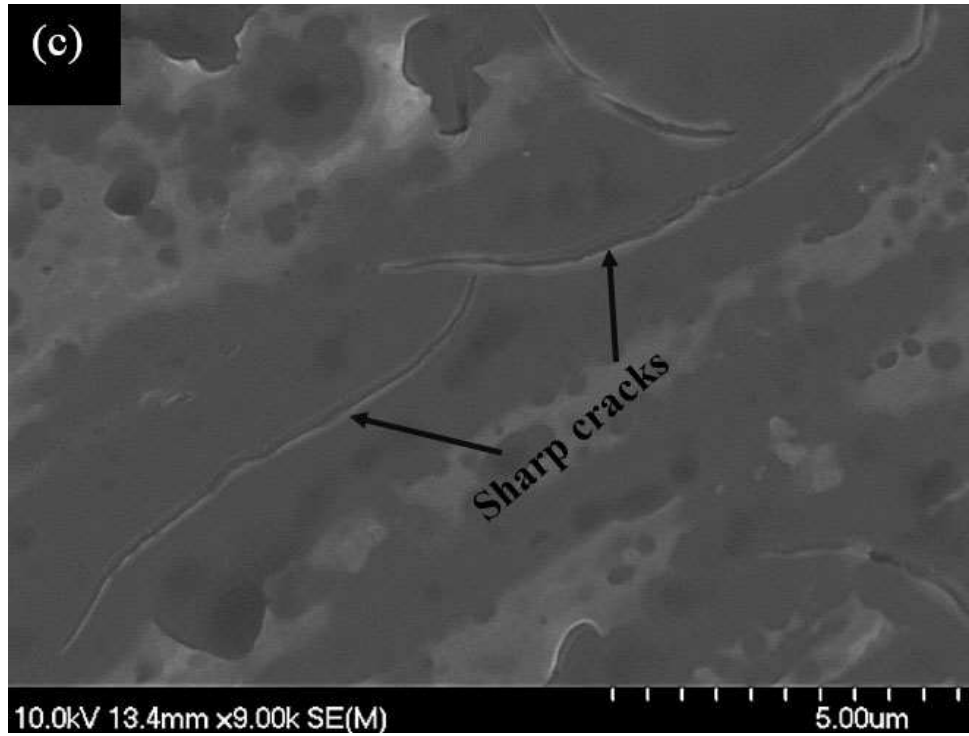
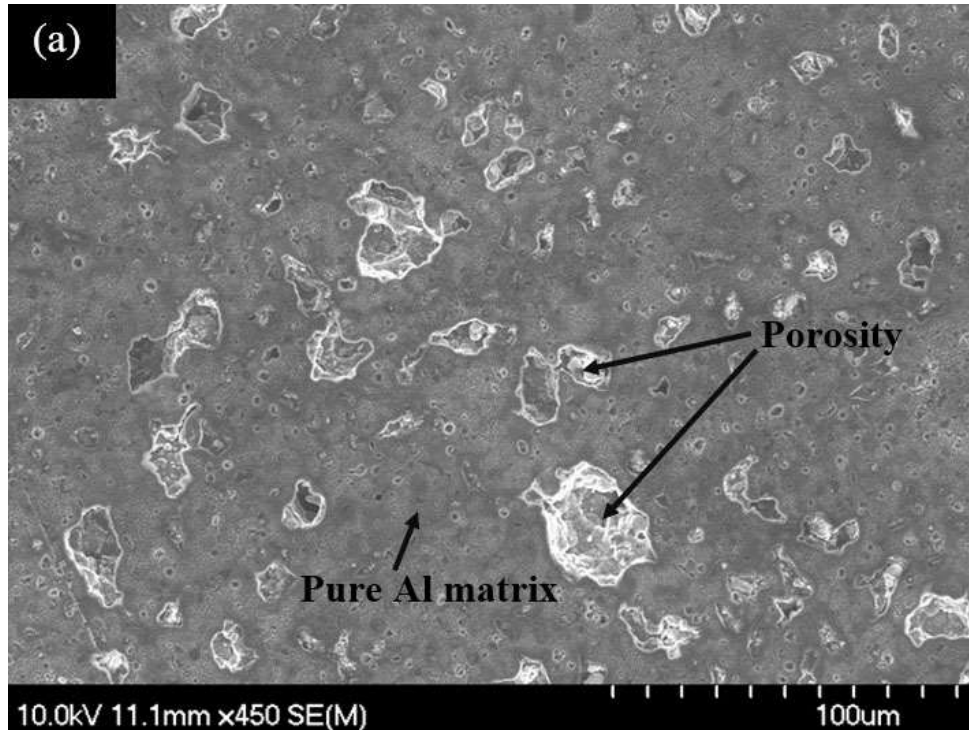
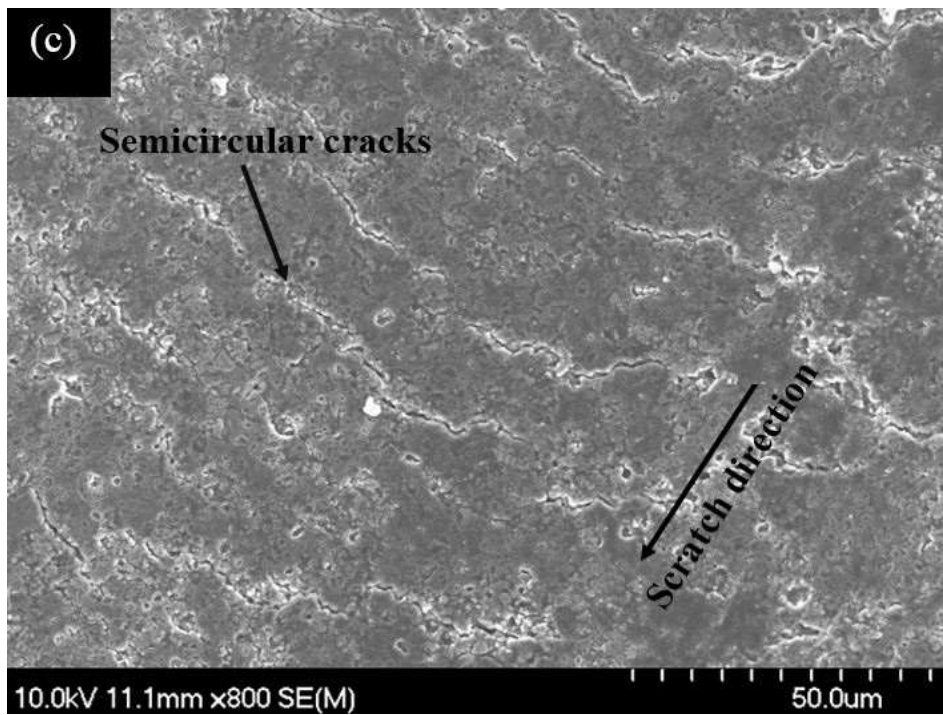
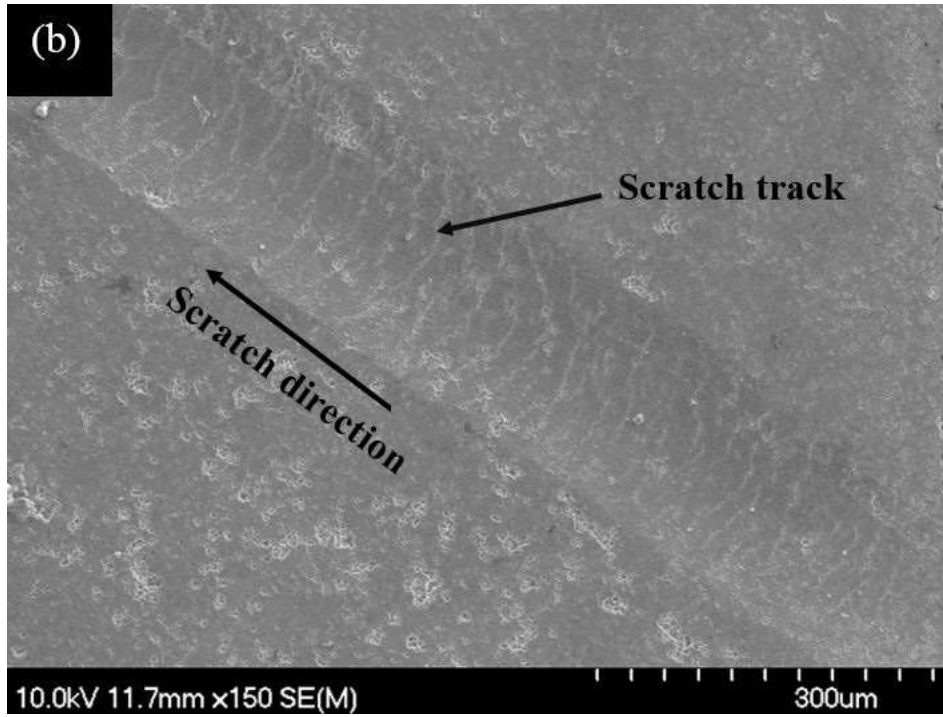


Figure 4.30 SEM micrographs of scratch track (a,b,c,d) for Al 6061 (3.5% porosity)

Scratch surface morphology of highly porous pure Al and Al 6061 exhibits signs of plastic deformation. The length profile through the scratch and its edges indicate a rougher appearance of the scratch surface. When the indenter slides on the work material surface, plastic cutting produces horizontal compressive stress on the work material surface in front of the indenter but a corresponding tensile stress behind it [175]. This tensile stress can easily cause surface cracking.





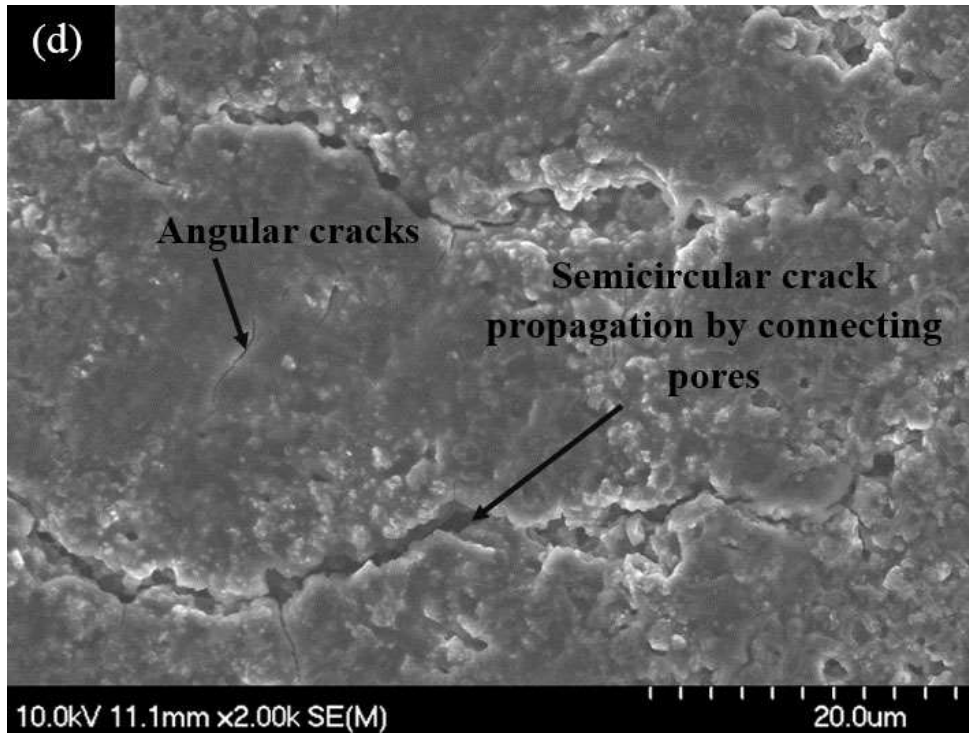
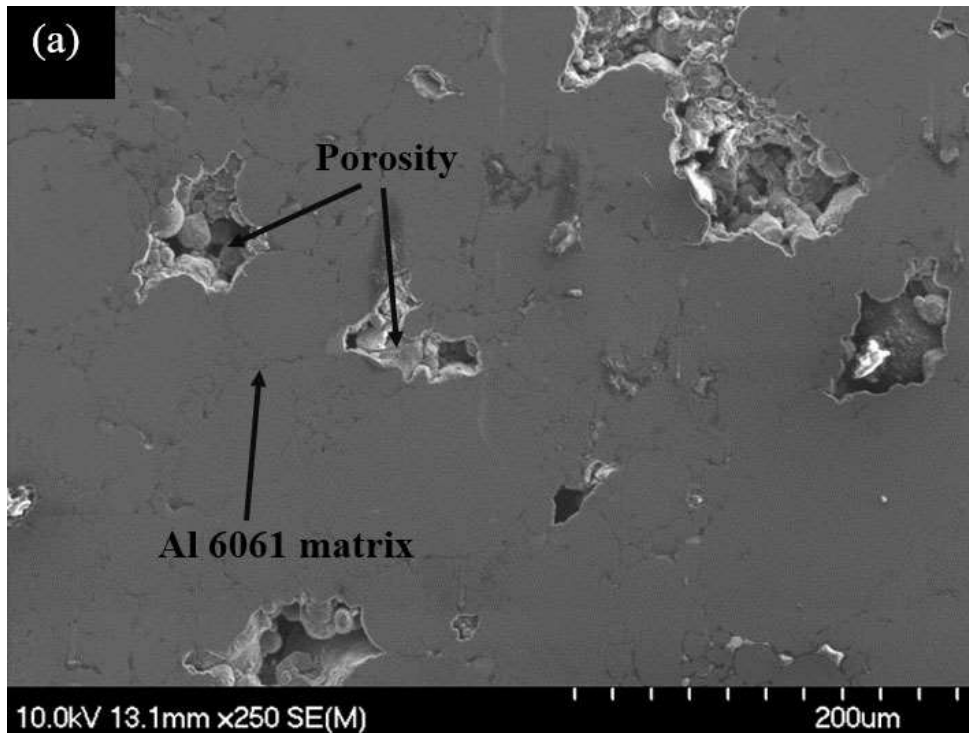
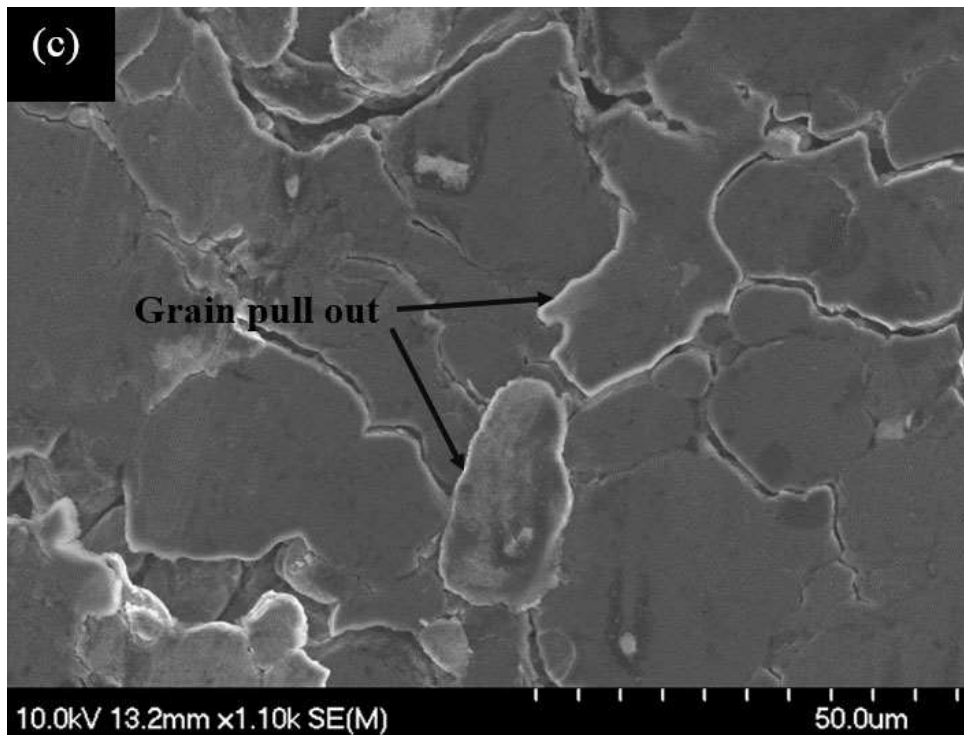
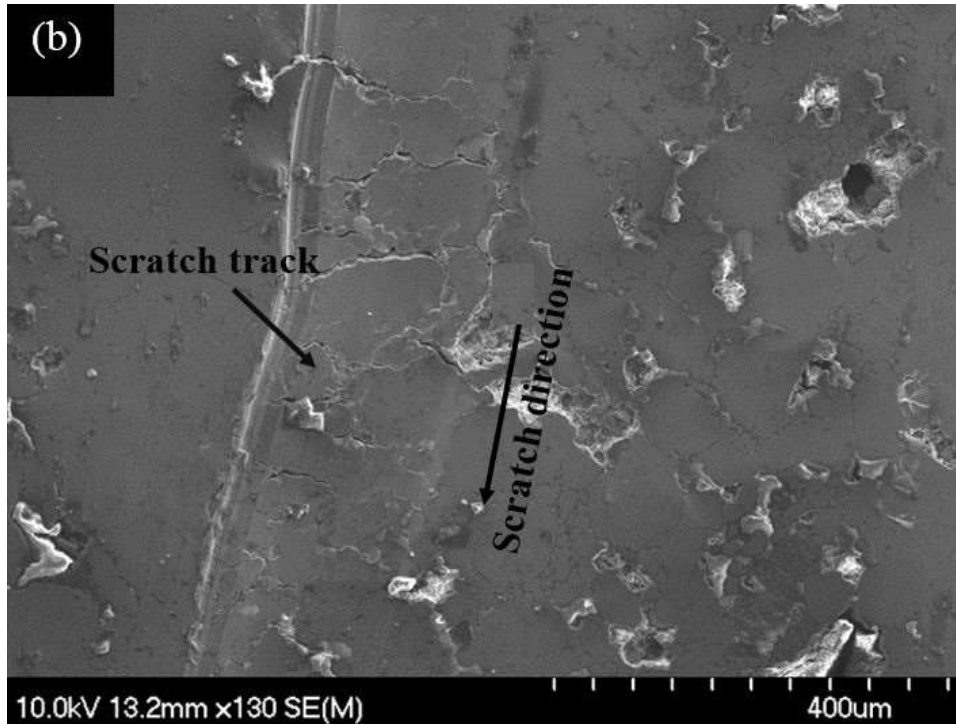
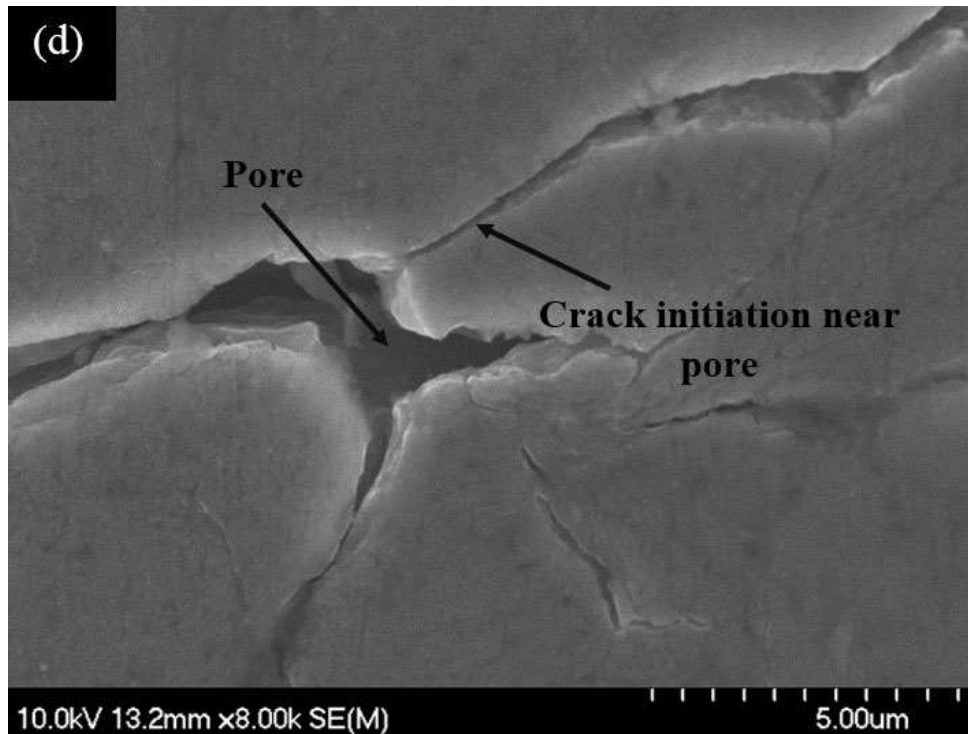


Figure 4.31 SEM micrographs of scratch track (a,b,c,d) for pure Al (3.5% porosity)







**Figure 4.32 SEM micrographs of scratch track (a,b,c,d) for Al 6061 (20.7% porosity)**

In case of highly porous pure Al, the scratch track was almost flat and periodic orientation of semicircular cracks (Fig.4.31 (c)) were observed [176]. Angular cracks initiated halfway with the semicircular cracks (Fig. 4.31 (d)). The deformation caused by the indenter in Al 6061 specimen results in grain pull out from the surroundings which ultimately leads to material loss (Fig.4.32(c)). Considerable brittle damage surrounds the scratch track in the form of cracking resulted in material deformation [177-183]. In some places, where large fragments are removed, the material loss can be significantly greater. As pore edges represent stress concentration areas they tend to fracture with the passing of the indenter. This is evident from the cracks initiating from pore edge. Figure 4.32 (d) shows the extension of these cracks due to the motion of the indenter.

As the load applied here is very small (1N), the damage is not extensive, but the grain dislodgement in Al 6061 specimen indicates that the scratching is highly sensitive to the amount of porosity.

## CHAPTER 5 CONCLUSIONS AND RECOMMENDATIONS

In the present project, the effects of surface porosity on the tribological properties of automotive Al alloys were studied. The tribological behavior of as received Al A380M alloy and pure Al having surface porosity range from 1.9% to 15.1% and Al 6061 with surface porosity ranging from 3.5% to 20.7% have been investigated. The following main conclusions can be drawn:

- i) There is an inverse relationship between the hardness and porosity content of Al alloys. Hardness decreases with an increase in surface porosity. For pure Al, a reduction in hardness of about 40% is observed as surface porosity increases from 1.9 % to 15.1% and for Al 6061, 90 % hardness reduction is observed as porosity increases from 3.5% to 20.7 %.
- ii) Wear resistance is not only a function of pore size but significantly affected by pore distribution. For a given amount of porosity and pore size uniform pore distribution results in accelerated wear. When the pores are uniformly distributed, cracks can propagate at a high rate as pores can easily link up with each other and form a wide network of cracks. This effect ultimately contributes to the fracturing of material and increasing wear rate. Pores in pure Al and Al 6061 are more uniformly distributed than Al A380M alloy which also contributes to the high wear resistance exhibited by Al A380M alloy.
- iii) Indentation hardness of porous materials leads to high maximum penetration depth and high contact depth. The morphology of the pores immediately beneath the Al matrix or within the zone of influence has a significant effect on the response of the indenter and measured nanohardness and Young's modulus. Especially the size and shape of the pores within the zone control the indenter response. When the indenter tip touches the solid phase, the solid phase resists the tip, but if there are pores beneath the tip, the resistance is reduced. That is, for a given load, the depth of penetration increases with increasing porosity. In this work, for pure Al, indentation depth increased from 2.5 $\mu\text{m}$  to 3.5  $\mu\text{m}$  for the same constant load 100 mN as the total amount of porosity increased from 1.9% to 15.1%. And for Al 6061, the depth increase was from 2.4  $\mu\text{m}$  to 3.0  $\mu\text{m}$  as surface porosity increased from 3.5% to 20.7%.
- iv) The coefficient of friction decreases considerably with increasing load but increases with increasing porosity percentage. Under dry sliding conditions, the generation of frictional heat

between two sliding surfaces raises the temperature at the interface and promotes softening of the aluminium, which in turn, lowers the coefficient of friction with increasing load. The rise in the coefficient of friction with increasing porosity might be attributed to the formation of more asperity-asperity contact during sliding.

- v) A predominance of abrasive and oxidative wear was identified in all Al specimens. As the size of the pores were very large compared to wear debris produced, some of the debris particles entrap into the pores and some were remained between the sliding surfaces and were repeatedly fractured and oxidized. The fracture of debris continuously exposed more fresh metal to the environment, which promote an oxidation reaction.
- vi) There was no significant variation in scratch width between pure Al and Al 6061 at low porosity. But in highly porous specimens significant increase in scratch width was observed in both pure Al and Al 6061 specimens. As a result, the scratch hardness drops. During scratching, periodic semicircular crack pattern was observed in the deformed region of highly porous pure Al and grain dislodgement inside the scratch track was identified for highly porous Al 6061 specimen.

Although a fair amount of work has been performed in this study, more work is needed for a comprehensive understanding of the wear process. A number of recommendations for future work are listed below:

- i) Developing a wear mechanism map under different loads and frequencies and include the effect of porosity. Such map would be beneficial for the aluminium manufacturing industry.
- ii) Using Atomic Force Microscopy to measure the surface roughness, local changes in friction and asses changes in local elasticity over a sample surface.
- iii) Changing the frequency during the wear test to observe the variation in wear rates with increasing the amount of porosity.

## REFERENCES

- [1] A. Srivastan TS, W. Y and L. EJ, "Processing, microstructure and fracture behavior of a spray atomized and deposited Aluminium-Silicon alloys," *Journal of Materials Science*, vol. 32, pp. 2835-2848, 1997.
- [2] Z. J, D. J and K. BM, "As-Spray-deposited structure of an Al-20Si-5FeO spre perform and its development during subsequent processing," *Journal of Materials Science*, vol. 26, pp. 5275-5291, 1991.
- [3] B. Prasard, K. Venkateswarlu, O. Modi, A. Jha, S. Das, R. Dasgupta and A. Vegneswaran, "Sliding wear behavior of some Al-Si alloys: Role of shape and size of Si particles and Test conditions," *Metallurgical and Materials Transactions*, vol. 29A, pp. 2747-2752, 1998.
- [4] R. Shivanath, SenguptaP.K. and T. Eyre, "Wear of Aluminium-Silicon alloys," *The British Foundrymen*, vol. 70, no. 12, p. 349, 1997.
- [5] R. Yassen and E. Dwarakadasa, "Wear of Aluminium under dry sliding conditions," *Wear*, vol. 84, pp. 375-379, 1983.
- [6] M. K H, K. D G and K. Y D, "Sintering characteristic of AlO<sub>3</sub>-reinforced 2xxx series Al composite powders. Journal of Alloys Compounds," *Journal of Alloys Compounds*, vol. 400, pp. 150-153, 2005.
- [7] Metal Handbook, 9th ed., vol. 7, Powder Metallurgy,ASM, 1984.
- [8] L. Zhen and S. Kang, "Deformation and fracture behavior of two Al-Mg-Si alloys," *Metallurgical and Materials Transactions*, vol. 28A, pp. 1489-1497, 1997.
- [9] A. Clegg and A. Das, "The influence of structural modifiers on the refinement of the primary silicon in a hypereutectic aluminium silicon alloy," *The British Foundrymen*, vol. 70, pp. 56-63, 1997.
- [10] M. R, B. JD and B. Y., "Microstructural and analytical characterization of Al<sub>2</sub>O<sub>3</sub> composite interfaces," *Materials Science and Engineering A*, vol. 135, pp. 111-117, 1991.
- [11] N. ED., "Semi-solid forming of Aluminium and Magnesium," *Light Metal Age*, vol. 57, pp. 54-58, 1997.
- [12] A. DM and M. PJ, "Corrosion behavior of cast Aluminium Matrix Composites in Chloride Media," *Journal of the Electrochemical Society* , vol. 132, p. 1257, 1985.

- [13] T. Zeuner, P.Stojanov, P.R.Sahm, H. Ruppert "Developing trends in disc brake technology for rail application," *Materials Science and Technology* , vol. 14, pp. 857-863, 1998.
- [14] H. Proudhan, J. Savkova, S. Basseville, V. Guipont, M. Jeandin and G. Cailletaud, "Experimental and numerical wear studies of porous reactive plasma sprayed Ti-6Al-4V/TiN Composite coating," *Wear* , vol. 311, pp. 159-166, 2014.
- [15] Z. Lin, Q. X. hui, D. Bo-hua, H. Xin-Bo and Q. ming-li, "Effect of porosity on wear resistance of SiCp/Cu composites prepared by pressureless infiltration," *Transactions of Nonferrous Metal Society of China*, vol. 18, pp. 1076-1082, 2008.
- [16] Q. Chen, D. Li and B. Cook, "Is porosity always detrimental to the wear resistance of materials? A computational study on the effect of porosity on erosive wear of TiC/Cu composites," *Wear* , vol. 267, pp. 1153-1159, 2009.
- [17] A. Simchi and H. Danninger, "Effects of porosity on delamination wear behaviour of sintered plain iron. Powder Metallurgy," *Powder Metallurgy*, vol. 47, pp. 73-80, 2004.
- [18] B. Dubrujeaud, M.Vardavoulias and M.Jeandin, "The role of porosity in the dry sliding wear of a sintered ferrous alloy," *Wear*, vol. 174, pp. 155-161.
- [19] D. Li and Y. Luo, "Effects of TiN nano-particles on porosity and wear behavior of TiC/TiNi tribo composite," *Journal of Materials Science Letters*, vol. 20, pp. 2249-2252, 2001.
- [20] A.A.Hamid, P.Ghosh, S.Jain and S.Ray, "Influence of particle content and porosity on the wear behaviour of cast in situ Al(Mn)-Al<sub>2</sub>O<sub>3</sub>(MnO<sub>2</sub>) composite," *Wear*, vol. 260, p. 368-378, 2006.
- [21] O. Sarikaya, " Effect of some parameters on microstructure and hardness of alumina coatings prepared by the air plasma spraying process," *Surface & Coatings Technology*, vol. 190, pp. 388-393, 2005.
- [22] N. Raghukiran and R. Kumar, "Processing and dry sliding wear performance of spray deposited hyper-eutectic aluminum-silicon alloys," *Journal of Materials Processing Technology*, vol. 213, p. 401-410, 2013.
- [23] C. Kanchanomaia, B. Saengwichian and A. Manonukul, "Delamination wear of metal injection moulded 316L stainless steel," *Wear*, vol. 267, pp. 1665-1672, 2013.
- [24] C. Tekmen, I. Ozdemir, U. Cocen and K. Onel, "The mechanical response of Al-Si-Mg/SiCp composite: influence of porosity," *Materials Science and Engineering A*, vol. 360, pp. 365-371, 2003.

- [25] H. Danninger, G. Jangg, B. Weiss and R. Stickler, "Microstructure and mechanical properties of sintered iron," *Powder Metallurgy International*, vol. 25, pp. 111-117, 1993.
- [26] A. Bergmark, L. Alzati and U. Persson, "Crack initiation and crack propagation in copper powder mixed PM steel," *Powder Metallurgy Progress*, vol. 2, pp. 222-230, 2002.
- [27] D. Gerard and D. Koss, "Low cycle fatigue crack initiation: modeling the effect of porosity," *International Journal of Powder Metallurgy*, vol. 26, pp. 337-343, 1990.
- [28] Y. Sahin, "Preparation and some properties of SiC particle reinforced aluminium alloy composites," *Materials and Design*, vol. 24, pp. 671-679, 2003.
- [29] Y. Sahin and M. Acilar, "Production and properties of SiCp. Composites: Part A.," *Composites Part A*, vol. 34, p. 709-718., 2003.
- [30] P. Yih and D. Chung, "Titanium diboride copper-matrix composites," *Journal of Materials Science*, vol. 32, pp. 1703-1709, 1997.
- [31] S. Ray, S. Fishman and A. Dhingra, "Proceedings on Cast Reinforced Metal Composites.," *ASM International*, pp. 77-86, 1988.
- [32] B.A.Mathew and R. Mastromatteo, "Metal injection moulding for automotive applications," *Metal Powder Report*, vol. 57, p. 20-23, 2002.
- [33] G. Bocchini, "Influence of porosity on the characteristics of sintered materials," *International Journal of Powder Metallurgy*, vol. 22, p. 185-188, 1986.
- [34] E. Klar and P. Samal, *Powder metallurgy stainless steels*, vol. 7, Powder Metal Technologies and Applications, ASM International, 1994.
- [35] R. Hardin and C. Beckermann, "Effect of porosity on the stiffness of cast steel," *Metallurgical. And Materials Transactions A*, vol. 12, pp. 2992-3006, 2007.
- [36] P.Deshpande and R.Lin, "Wear resistance of WC particle reinforced copper matrix composites and the effect of porosity," *Materials Science and Engineering A*, vol. 418, p. 137-145, 2006.
- [37] S. N.P., "An overview of the delamination theory of wear," *Wear*, vol. 44, pp. 1-16, 1977.
- [38] M. Vardavoulias, C. Jouanny-Tresy and M. Jeandin, "Sliding-wear behaviour of ceramic particle-reinforced high-speed steel obtained by powder metallurgy.," *Wear.*, vol. 165, p. 141-149, 1993.
- [39] M. Gui, S. Kang and J. Lee, "Influence of porosity on dry sliding wear behavior in spray deposited Al-6Cu-Mn/SiCp composite," *Materials Science and Engineering A*, vol. 293, pp. 146-56, 2000.

- [40] I. Bertilsson, B. Karlsson and J. Wasen, "International conference on powder metallurgy and particulate materials," Toronto, 1994.
- [41] R. Scheps, "Total Vehicular Energy Use Management," <http://aluminumintransportation.org/downloads/World%20Congress%20Presentation%20-%20final.pdf>," 16 December 2011. [Online].
- [42] E. A. Association, " Stiffness relevance and strength relevance in crash of car body components <http://www.drivealuminum.org/research-resources/PDF/Research/2010/2010-EAA-Aachen-Study.pdf>," 21 January 2014. [Online].
- [43] J. Boileau and J. Allison, "The Effect of Porosity Size on the Fatigue Properties in a Cast 319 Aluminum Alloy," *SAE transactions*, vol. 110, 2001.
- [44] G. Sigworth, C. Wang, H. Huang and T. Berry, "Porosity Formation in Modified and Unmodified Al-Si Alloy Casting," *AFS Transactions*, vol. 102, 1994.
- [45] M. Kim, H. Kwon, D. Kim and C. Loper, "Porosity formation in Relation to the Feeding Behavior of Al-Si Alloys," *AFS Transactions*, vol. 105, 1997.
- [46] C. Tian, J. Law, J. van der Touw and M. Murray, "Effect of melt cleanliness on the formation of porosity defects in automotive aluminium high pressure die castings," *Journal of Materials Processing Technology*, vol. 122, no. 1, pp. 82-93, 2002.
- [47] R. Lumley, I. Polmear, H. Groot and J. Ferrier, "Thermal characteristics of heat-treated aluminum high-pressure die-castings.," *Scripta Materialia*, vol. 58, no. 11, pp. 1006-1009., 2008.
- [48] J. Anson and J. Gruzleski, "Effect of Hydrogen Content on relative shrinkage and Gas Microporosity in Al-7% Si Casting," *AFS Transactions*, vol. 107, pp. 135-142, 1999.
- [49] G. Lutjering and J. C. Williams, *Titanium*, 2nd ed., Springer Verlag, 2003.
- [50] R. German, *Powder Metallurgy Science*, 2nd ed., Metal Powder Industries.
- [51] S. Kalpakjian and S. R. Schmid, *Manufacturing process for engineering materials*, NJ: Pearson Education, 2003.
- [52] P. E. Price and S. P. Kohler, *Cold isostatic pressing of metal powders.*, vol. 7, Ohio: Metals park, ASM, 1984.
- [53] A. R. Erikson and R. E. Wiech, *Metals Handbook*, vol. 7, Ohio: Metals park, ASM., 1984.

- [54] R. German, Powder Metallurgy Science, 2nd ed., New Jersey: Metal Powder Industries Federation, 1994.
- [55] Powder Metallurgy Design Solutions, Metal Powder Industries Federation, 1999.
- [56] H. H.-M., S. Hiller and F. GarciaMoreno, "Influence of compaction Conditions on the Formability of AlSi8Mg4 Alloy," *Metallurgical and Materials Transactions B*, vol. 40, pp. 755-767, 2009.
- [57] G. Schaffer and B. Hall, "The Influence of the Atmosphere on the Sintering of Aluminum," *METALLURGICAL AND MATERIALS TRANSACTIONS A*, vol. 33, pp. 3279-3284, 2002.
- [58] "Retrieved from In situ Microtomography Study of Metallic Powder Sintering : <http://www.esrf.eu/UsersAndScience/Publications/Highlights/2002/Materials/MAT3>," 2006.
- [59] Y. Kim, W. Griffith and F. Froes., "Journal of Metals," vol. 37, no. 8, pp. 27-33, 1985.
- [60] G. Zum, "Microstructure and wear of materials," 1987.
- [61] N. Sacks, "The wear and corrosive-wear response of tungsten carbide-cobalt hardmetals under woodcutting and three body abrasion conditions," 2002.
- [62] D. Rigney, " Sliding wear of metals.," pp. 141-163., 1988.
- [63] S. Jahanmir and N. P. Suh, "Mechanics of subsurface void nucleation in delamination wear," *Wear*, vol. 44, pp. 17-38, 1977.
- [64] B. Bhushan and B. K. Gupta, Handbook of Tribology, New York: coatings, and surface treatments. : McGraw-Hill, 1991.
- [65] H. Czichos, A Systems Approach to the Science and Technology of Friction, Lubrication, and Wear, New York: Elsevier Scientific Pub. Co., 1978.
- [66] Friction, Lubrication, and Wear Technology, vol. 18, ASM International, 1992.
- [67] H. Czichos, A Systems Approach to the Science and Technology of Friction, Lubrication, and Wear, New York: Elsevier Scientific Pub. Co, 1978.
- [68] T. Saada, M. Oike and N. Emori, "The effects of abrasive grain size on the transition between abrasive and adhesive wear," *Wear*, vol. 97, pp. 291-302, 1984.
- [69] R. Johnson, "The use of the scanning electron microscope to study the deterioration of abrasive papers," *Wear*, vol. 12, pp. 213-216, 1968.
- [70] B. Bhushan, R. Davies and H. Kolar, "Metallurgical re-examination of wear modes II: Adhesive and abrasive," *Thin Solid Films*, vol. 123, pp. 113-126, 1985.

- [71] A. P. Harsha, "Two-body and three-body abrasive wear behaviour of polyaryletherketone composites.," *Polymer Testing*, vol. 22, no. 4, pp. 403-418, 2003.
- [72] B. Bharat, *Introduction to Tribology*, New York: John Wiley & Sons, 2002.
- [73] J. D. Lucas, *Tribology of 316L Austenitic Stainless Steel Carburized Steel at Low Temperature*, Cleveland, OH: Case Western University Reserve University, 2010.
- [74] G.J.Gore, "Effect of hardness on three very different form of wear," *Wear*, pp. 544-563, 1997.
- [75] A. Vencel, N.Manic, V. Popovic and M. Mrdak, "Possibility of the abrasive wear resistance determination with scratch tester," *Tribology Letters*, vol. 37, pp. 591-604, 2010.
- [76] E. F. Finkin, " An explanation of the wear of metals.," *Wear*, vol. 47, no. 1, pp. 107-117, 1978.
- [77] F. P. Bowden and D. Tabor, *Friction and Lubrication of Solids*, part 1, Oxford: Clarendon press, 1950.
- [78] T. Stolarski, "Analysis of the resistance to motion in a sliding contact," *Wear*, vol. 171, pp. 203-209, 1994.
- [79] J. F. Archard, " Contact and rubbing of flat surfaces.," *Journal of applied physics*, vol. 24, pp. 981-988, 1953.
- [80] "Retrieved from The Chain Reaction of Wear: [http://www.pall.com/hydraulic\\_3779.asp](http://www.pall.com/hydraulic_3779.asp)," 2007. [Online].
- [81] Y. Wang, L. Huang, W. Liu and J. Li, "The blast erosion behaviour of ultrahigh molecular weight polyethylene," *Wear*, vol. 218, p. 128, 1998.
- [82] G. D'Errico, S. Bugliosi, R. Calzavarini and D. Cuppini, "Wear of advanced ceramics for tool materials," *Wear*, p. 267-272, 1999.
- [83] J. Tu, L. Zhu and H. Zhao, "Slurry erosion characteristics of TiN coatings on  $\alpha$ Ti and plasma-nitrited Ti alloy substrates," *Surface and Coatings Technology*, vol. 122, p. 176-182, 1999.
- [84] K. T. H, "Solid Particle Erosion", vol. 18, ASM handbook.
- [85] P. H. Tehrani and M. Saket, "Fatigue crack initiation life prediction of railroad," *Journal of Physics*, vol. 181, pp. 1-8, 2009.
- [86] N. Suh, "The delamination theory of wear," *Wear*, vol. 25, pp. 111-124, 1973.
- [87] N. Suh, " Fundamentals of Friction and Wear of Materials," *American Society of Metals*, pp. 43-71, 1981.
- [88] D. Rigney, L. Chen, M. Naylor and R. A.R, "Wear processing in sliding system," *Wear*, vol. 100, pp. 195-219, 1984.

- [89] H. Torabian, J. Pathak and S. Tiwari, "Wear characteristics of Al-Si alloys," *Wear*, vol. 172, no. 1, pp. 49-58, 1994.
- [90] N. Saka, A. M. Eleiche and N. P. Suh, "Wear of metals at high sliding speeds," *Wear*, vol. 44, no. 1, pp. 109-125, 1977.
- [91] S. Wilson and A. A. T., "Wear mechanism maps for metal matrix composites," *Wear*, vol. 212, no. 1, pp. 41-49, 1997.
- [92] J. Tu, W. Rong, S. Guo and Y. Yang, "Dry sliding wear behavior of in situ Cu-TiB<sub>2</sub> nanocomposites against medium carbon steel," *Wear*, vol. 255, pp. 832-835, 2003.
- [93] P. Bindumadhavan, T. Chia, M. Chandrasekaran, H. K. Wah, L. N. Lam and O. Prabhakar, "Effect of particle-porosity clusters on tribological behavior of cast aluminum alloy A356-SiCp metal matrix composites," *Materials Science and Engineering A*, vol. 315, pp. 217-226, 2001.
- [94] T. S. Mahmoud, F. H. Mahmoud, H. M. Zakaria and T. A. Khalifa, "Effect of squeezing on porosity and wear behaviour of partially remelted A319/20 vol% SiCp metal matrix composites," *Journal of Mechanical Engineering Science*, vol. 222, pp. 295-303, 2008.
- [95] F. F. Ling and E. Saibel, "Thermal aspects of galling of dry metallic surfaces in sliding contact," *Wear*, vol. 1, no. 2, pp. 80-91, 1957.
- [96] P. Menezes, L. Kishore and S. V. Kailas, "Role of surface texture of harder surface on subsurface deformation," *Wear*, vol. 266, pp. 103-109, 2009.
- [97] A. J. Moore and W. J. Tegart, "Relation between Friction and Hardness," *Proceedings of the Royal Society*, vol. 212, pp. 452-458, 1952.
- [98] C. Subramanian, "Effects of sliding speed on the unlubricated wear behaviour of Al-12.3wt.% Si alloy," *Wear*, vol. 151, no. 1, pp. 97-110, 1991.
- [99] K. M. Jasim and E. S. Dwarakadasa, "Effect of sliding speed on adhesive wear of binary Al-Si alloys," *Journal of materials science letters*, vol. 12, pp. 650-653, 1993.
- [100] J. F. Archard, "Contact and rubbing of flat surfaces," *Journal of applied physics*, vol. 24, pp. 981-988, 1953.
- [101] W. Hirst and J. Lancaster, "The Influence of Speed on Metallic Wear.," *Proceedings of the Royal Society A*, vol. 259, pp. 228-241, 1960.
- [102] S. K. Biswas and B. N. Bai, "Dry wear of al-graphite particle composites," *Wear*, vol. 68, no. 3, pp. 347-358, 1981.

- [103] A. Simchi and H. Danninger, "Effects of porosity on delamination wear behaviour of sintered plain iron," *Powder Metallurgy*, vol. 47, no. 1, pp. 73-80, 2004.
- [104] S. C. Lim and M. F. Ashby, "Wear mechanism maps," *Acta metall*, vol. 35, no. 1, pp. 1-24, 1987.
- [105] Y. Liu and R. Asthana, "A map for wear mechanisms in aluminum alloys," *Journal of materials science*, vol. 26, pp. 99-102, 1991.
- [106] A. T. Alpas and J. Zhang, "Delamination wear in ductile materials containing second phase particles," *Materials Science and Engineering A*, vol. 160, pp. 25-35, 1993.
- [107] A. T. Alpas and J. Zhang, "Transition between mild and severe wear in aluminium alloys," *Acta Materialia*, vol. 45, pp. 513-528, 1997.
- [108] T. S. Eyre, "Wear Characteristics of Castings Used in Internal-Combustion Engines," *Metals technology*, vol. 11, pp. 81-90, 1984.
- [109] T. Ishihara and B. K. Yen, "Effect of humidity on friction and wear of Al-Si eutectic alloy and Al-Si alloy-graphite composites," *Wear*, vol. 198, pp. 169-175, 1996.
- [110] H. Goto, M. Ashida and K. Endo, "The influence of oxygen and water vapour on the friction and wear of an aluminium alloy under fretting conditions," *Wear*, vol. 116, pp. 141-155, 1987.
- [111] A. T. Alpas and M. Elmadagli, "Progression of wear in the mild wear regime of an Al-18.5% Si (A390) alloy," *Wear*, vol. 261, pp. 367-381, 2006.
- [112] R. Antoniou and C. Subramanian, "Wear mechanism map for aluminum alloys.," *Scripta Metallurgica*, vol. 22, pp. 809-814, 1988.
- [113] R. Shivanath, P. K. Sengupta and T. S. Eyre, "Wear of aluminum-silicon alloys," *British Foundryman*, vol. 70, pp. 349-356, 1977.
- [114] J. Clarke and A. Sarkar, "Wear characteristics of as-cast binary aluminium-silicon alloys," *Wear*, vol. 54, pp. 7-16, 1979.
- [115] J. Andrews, M. Seneviratne, K. Zier and T. Jett, "Influence of silicon content on the wear characteristics of hypereutectic Al-Si alloys.," in *International Conference on Wear of Materials*, 1985.
- [116] B. P. Bai and S. Biswas, "Characterization of dry sliding wear of Al-Si alloys," *Wear*, vol. 120, pp. 61-74, 1987.
- [117] H. Torabian, J. Pathak and S. Tiwari, "Wear characteristics of Al-Si alloys," *Wear*, vol. 172, pp. 49-58, 1994.

- [118] T. Hisakado, "Wear mechanism of ceramics and surface topography,," *Journal of Tribology*, vol. 108, p. 9, 1986.
- [119] Y. He, L. Winnubst, A. Burggraaf and H. Verweij., "Grain size dependence of sliding wear in tetragonal zirconia polycrystals," *Journal of the American Ceramic Society*, vol. 79, p. 3090–3096, 1996.
- [120] A. Korshunov, T. Kravchenko, L. Polyakov, A. Smolyakov, I. Vedernikova and A. Morozov, "Effects of the number of equal-channel angular pressing passes on the anisotropy of ultra-fine titanium,," *Materials Science and Engineering A*, vol. 493, p. 160–163, 2008.
- [121] F. Xiong, R. Manory, L. Ward and M. Terheci, "Effect of grain size and test configuration on the wear behavior of alumina,," *Journal of American Ceramic Society*, vol. 80, pp. 1310-1312, 1997.
- [122] M. A. Chowdhury, M. K. Khalil, D. M. Nuruzzaman and M. L. Rahaman., "The Effect of Sliding Speed and Normal Load on Friction and Wear Property of Aluminum," *International Journal of Mechanical & Mechatronics Engineering*, vol. 11, no. 1, 2011.
- [123] M. X. Wei, K. M. Chen, S. Q. Wang and X. H. Cui, "Analysis for Wear Behaviors of Oxidative Wear," *Tribology Letters*, vol. 42, pp. 1-7, 2011.
- [124] S. Kumar and V. Balasubramanian, "Effect of reinforcement size and volume fraction on the abrasive wear behaviour of AA7075 Al/SiCp P/M composites-A statistical analysis," *Tribology International*, vol. 43, pp. 414-422., 2010.
- [125] H. Proudhon, J. Savkova, S. Basseville, V. Guipont, M. Jeandin and G. Cailletaud, "Experimental and numerical wear studies of porous Reactive Plasma Sprayed Ti-6Al-4V/TiN composite coating," *Wear*, vol. 311, pp. 159-166, 2014.
- [126] Z. Lin, Q. X. hui, D. Bo-hua, H. Xin-Bo and Q. ming-li, "Effect of porosity on wear resistance of SiCp/Cu composites prepared by pressureless infiltration," *Transactions of Nonferrous Metals Society China*, vol. 18, pp. 1076-1082., 2008.
- [127] Q. Chen, D. Li and B. Cook, "Is porosity always detrimental to the wear resistance of materials? A computational study on the effect of porosity on erosive wear of TiC/Cu composites," *Wear*, vol. 267, p. 1153–1159, 2009.
- [128] A. Simchi and H. Danninger, "Effects of porosity on delamination wear behaviour of sintered plain iron," *Powder Metallurgy*, vol. 47, no. 8, pp. 73-80, 2004.

- [129] S. Ray, S. Fishman and A. Dhingra, "Proceedings on Cast Reinforced Metal Composites," *ASM International*, pp. 77-86, 1988.
- [130] B.A.Mathew and R. Mastromatteo, "Metal injection moulding for automotive applications," *Metal Powder Report*, vol. 57, pp. 20-23, 2002.
- [131] G. Bocchini, "Influence of porosity on the characteristics of sintered materials," *International Journal of Powder Metallurgy*, vol. 22, pp. 185-188, 1986.
- [132] E. Klar and P. Samal, "Powder metallurgy stainless steels," *ASM Handbook, Powder Metal Technologies and Applications*, vol. 7, 1994.
- [133] I. Bertilsson, B. Karlsson and J. Wasen, in *International Conference on Powder Metallurgy and Particulate Materials*, Toronto, 1994.
- [134] R. Hardin and C. Beckermann, "Effect of porosity on the stiffness of cast steel," *Metallurgical and Materials Transactions A*, vol. 12, pp. 2992-3006, 2007.
- [135] P.Deshpande and R.Lin, "Wear resistance of WC particle reinforced copper matrix composites and the effect of porosity," *Materials Science and Engineering A*, vol. 18, pp. 137-145, 2006.
- [136] S. N.P, "An overview of the delamination theory of wear," *Wear*, vol. 44, no. 1, pp. 1-16, 1977.
- [137] M. Vardavoulias, C. Jouanny-Tresy and M. Jeandin, "Sliding-wear behaviour of ceramic particle-reinforced high-speed steel obtained by powder metallurgy," *Wear*, vol. 165, pp. 141-149, 1993.
- [138] M. Gui, S. Kang and J. Lee, "Influence of porosity on dry sliding wear behaviour in spray deposited Al-6Cu-Mn/SiCp composite," *Materials Science and Engineering A*, vol. 293, pp. 145-156, 2000.
- [139] C. Amsallem, A. Gaucher and G. Guillhot, "The unlubricated frictional behaviour of sintered iron," *Wear*, vol. 23, no. 1, pp. 97-112, 1973.
- [140] B. Dubrujeaud, M. Vardavoulias and M. Jeandin., "The role of porosity in the dry sliding wear of a sintered ferrous alloy," *Wear*, pp. 155-161, 1994.
- [141] J. A. Wang and H. Danninger, "Factor Influencing the wear behavior of PM steels," *Acta Metallurgica Sinica*, vol. 14, no. 1, pp. 33-41, 2001.
- [142] G. Straffelini and A. Molinari, "Dry Sliding Wear of Ferrous PM Materials.," *Powder Metallurgy*, vol. 44, no. 3, pp. 248-252, 2001.
- [143] J.-a. W and H. Danninger, "Factors Influencing the Wear Behavior of Sintered Steels," *Journal of Shanghai University*, vol. 5, no. 3, pp. 241-246, 2001.

- [144] J. Wang, Y. He and H. Danninger, "Influence of Porosity on the Sliding Wear Behavior of Sintered Fe-1.5Mo-0.7C Steels," *Journal of Materials Engineering and Performance*, vol. 12, no. 3, pp. 339-344, 2003.
- [145] A. D. Sarkar and J. Clarke, "Wear Characteristics of as-cast Binary Aluminium-Silicon Alloys," *Wear*, vol. 54, no. 1, pp. 7-16, 1979.
- [146] A. Sarkar and J. Clacke, "Friction and Wear of Aluminium-Silicon Alloys," *Wear*, vol. 61, no. 1, pp. 157-167, 1980.
- [147] K. Tingler, A Developmental Study in Tensile Properties of Plaster cast A356 Aluminum Alloy at Room and Elevated Temperature. Oklahoma, OK.; Oklahoma: Oklahoma State University Stillwater, 2008.
- [148] J. Gomes, A. Ramalho, M. Gaspar and S. Carvalho, "Reciprocating wear tests of Al-Si/SiCp composites: A study of the effect of stroke length," *Wear*, vol. 259, no. 1-6, pp. 545-552, 2005.
- [149] Y. Ma, Integrated Study of the Influence of Casting and Heat Treatment Parameters on Microstructures of Multiphase Multi-component Aluminum Alloys, University of Connecticut, 2008.
- [150] W. C. Oliver and G. Pharr, "Improved technique for determining hardness and elastic modulus using load and displacement sensing indentation experiments.," *Journal of Materials Research*, vol. 74, p. 1564-1580., 1992.
- [151] Z. N. Farhat and M. A. Islam, "Effect of porosity on dry sliding wear of Al-Si alloys," *Tribology International*, vol. 44, pp. 498-504, 2011.
- [152] N. Fleck, H. Otoyoy and A Needleman, "Indentation on porous solids," *International journal of solids and structures*, vol. 29, p. 1613, 1992.
- [153] B. Jang and H. matsubara, "Influence of porosity on hardness and Young's modulus of nanoporous EB-PVD TBCs by nanoindentation," *Materials Letters*, vol. 59, pp. 3462-3466., 2005.
- [154] X. Chen, T. Xiang and H. J. Vlassak, "Novel technique for measuring the mechanical properties of porous materials by nanoindentation," *Journal of Materials Research*, vol. 21, no. 3, 2006.
- [155] Z. Ling, X. Wang and J. Ma, "The response of porous Al<sub>2</sub>O<sub>3</sub> probed to nanoindentation," *Materials Science and Engineering A*, pp. 285-288, 2008.

- [156] G. K. Gyimah, D. Chen and P. Huang, "Dry Sliding Studies of Porosity on Sintered Cu-based Brake Materials," *Transaction on control and mechanical systems*, vol. 2, no. 5, pp. 219-224, 2013.
- [157] D. Dwivedi, " Adhesive wear behaviour of cast aluminium–silicon alloys: Overview," *Materials and Design* , vol. 31, p. 2517–2531., 2010.
- [158] M. Elmadagli, T. Perry and A. Alpas, "A parametric study of the relationship between microstructure and wear resistance of Al–Si alloys," *Wear*, vol. 262, pp. 79-92, 2007.
- [159] M. A. Chowdhury, M. K. Khalil, D. M. Nuruzzaman and M. L. Rahaman, "The Effect of Sliding Speed and Normal Load on Friction and Wear Property of Aluminum," *International Journal of Mechanical & Mechatronics Engineering*, vol. 11, no. 1, 2011.
- [160] M. X. Wei, K. M. Chen, S. Q. Wang and X. H. Cui, "Analysis for Wear Behaviors of Oxidative Wear," *Tribology Letters*, vol. 42, pp. 1-7, 2011.
- [161] R. A. Al-Samarai, Haftirman, K. R. Ahmad and Y. Al-Douri, "Effect of Load and Sliding Speed on Wear and Friction of Aluminum–Silicon Casting Alloy," *International Journal of Scientific and Research Publications*, vol. 2, no. 3, 2012.
- [162] S. Kumar and V. Balasubramanian, "Effect of reinforcement size and volume fraction on the abrasive wear behaviour of AA7075 Al/SiCp P/M composites-A statistical analysis," *Tribology International*, vol. 43, pp. 414-422, 2010.
- [163] J. Corrochano, J. Walker, M. Lieblich, J. Ibanez and W. Rainforth, "Dry sliding wear behaviour of powder metallurgy Al–Mg–Si alloy-MoSi<sub>2</sub> composites and the relationship with the microstructure," *Wear*, vol. 270, p. 658–665, 2011.
- [164] M. Bermudez, G. Martinez-Nicolas, F.J. Carrion, I. M.-M. a and E. H. J.A. Rodriguez, "Dry and lubricated wear resistance of mechanically-alloyed aluminium-base sintered composites," *Wear*, vol. 248, pp. 178-186, 2001.
- [165] A. A. Hamid, P. Ghosh, S. Jain and S. Ray, "The influence of porosity and particles content on dry sliding wear of cast in situ Al(Ti)–Al<sub>2</sub>O<sub>3</sub>(TiO<sub>2</sub>) composite," *Wear*, vol. 265, pp. 14-26, 2008.
- [166] O. Yılmaz and S. Buytoz., "Abrasive wear of Al<sub>2</sub>O<sub>3</sub>-reinforced aluminium-based MMCs," *Composites Science and Technology*, vol. 61, p. 2381–2392, 2001.

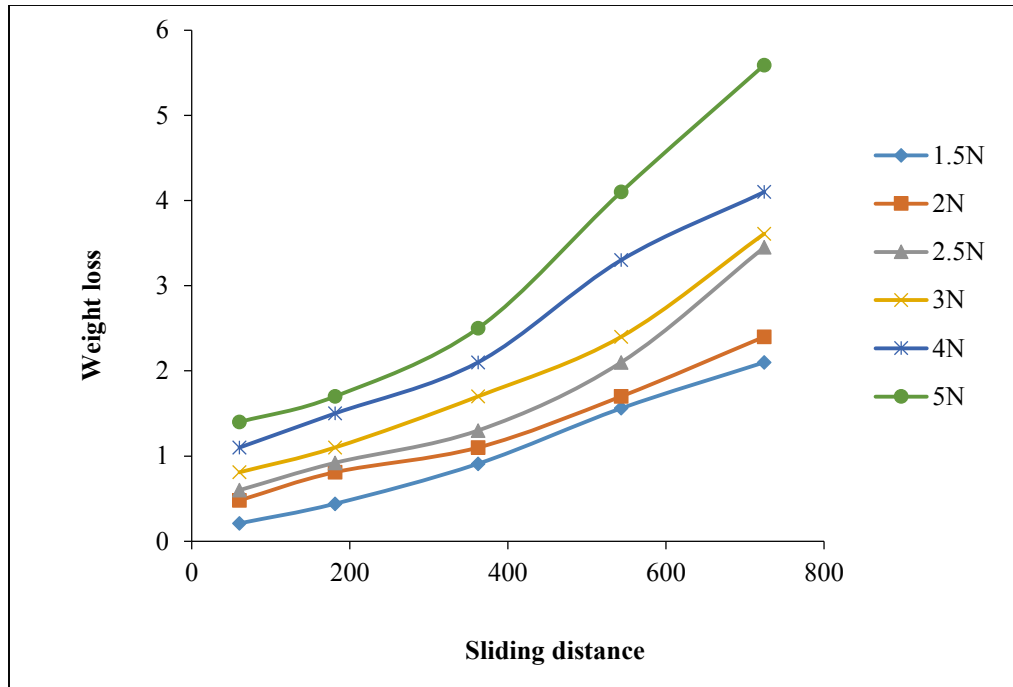
- [167] B. Yalcin, " Effect of porosity on the mechanical properties and wear performance of 2% copper reinforced sintered steel used in shock absorber piston production.," *Journal of Materials Science and Technology*, vol. 25, no. 5, pp. 577-582., 2009.
- [168] A. P. Rao, K.Das, B. Murty and M.Chakraborty, "Microstructure and the wear mechanism of grain-refined aluminium during dry sliding against steel disc.," *Wear*, vol. 264, pp. 638-647, 2008.
- [169] F.Alshmiri, H.V.Atkinson, S.V.Hainsworth, C.Haidon and S.D.A.Lawes, "Dry sliding wear of aluminium-high silicon hypereutectic alloys," *Wear*, vol. 313, pp. 106-116, 2014.
- [170] S. Deya, T. Perry and A. Alpas, "Micromechanisms of low load wear in an Al–18.5% Si alloy," *Wear*, vol. 267, pp. 515-524, 2009.
- [171] M. A. Islam and Z. N. Farhat, "The influence of porosity and hot isostatic pressing treatment on wear characteristics of cast and P/M aluminum alloys," *Wear*, vol. 271, p. 1594– 1601., 2011.
- [172] S. Sinha, S. Reddy and M. Gupta, "Scratch hardness and mechanical property correlation for Mg/SiC and Mg/SiC/Ti metal-matrix composites.," *Tribology International*, vol. 39, pp. 184-189, 2006.
- [173] Standard test method for scratch hardness of materials using a diamond stylus, ASTM standard designation.
- [174] C. Yan and L. Zhang, "Single-Point scratching of 6061 Al alloy reinforced by different ceramics particles," *Applied Composite Materials*, pp. 431-447, 1995.
- [175] K. Farokhzadeh, A. Edrissy, G. Pigott and P. Lidster, "Scratch resistance analysis of plasma-nitrided Ti-6Al-4V alloy," *Wear*, vol. 302, pp. 845-853, 2013.
- [176] A. Karimzadeh, M. Ayatollahi, A. Bushroa and M. Herliansyah, "Effect of sintering temperature on mechanical and tribological properties of hydroxyapatite measured by nanoindentation and nanoscratch experiments," *ceramics international*, 2014.
- [177] S. Varma and R. R. Romero, "The effect of impact and continuous scratches on the corrosive wear behavior of Fe-18%Cr-5%Ni alloy and 304 stainless steel for two grain sizes," *Wear*, vol. 201, pp. 121-131, 1996.
- [178] K. Friedrich, H. Sue, P. Liu and A. Almajid, "Scratch resistance of high performance polymers," *Tribology International*, vol. 44, pp. 1032-1046, 2011.

- [179] M. Klecka and G. Subhash, "Grain size dependence of scratch-induced damage in alumina ceramics," *Wear*, vol. 265, pp. 612-619, 2008.
- [180] Y. Xie and H. Hawthorne, "On the possibility of evaluating the resistance of materials to wear by ploughing using a scratch method," *Wear*, vol. 240, pp. 65-71, 2000.
- [181] V. Vitry, F. Delaunois and C. Dumortier, "Mechanical properties and scratch test resistance of nickel-boron coated aluminium alloy after heat treatments," *Surface & Coatings Technology*, vol. 202, pp. 3316-3324, 2008.
- [182] P. Narasimman, M. Pushpavanam and V. Periasamy, "Wear and scratch resistance characteristics of electrodeposited nickel-nano and micro SiC composites," *Wear*, pp. 197-206, 2012.
- [183] A. Vencel, N. Manic, V. Popovic and M. Mrdak, "Possibility of the abrasive wear resistance determination with scratch tester," *Tribology Letters*, vol. 37, pp. 591-604, 2010.

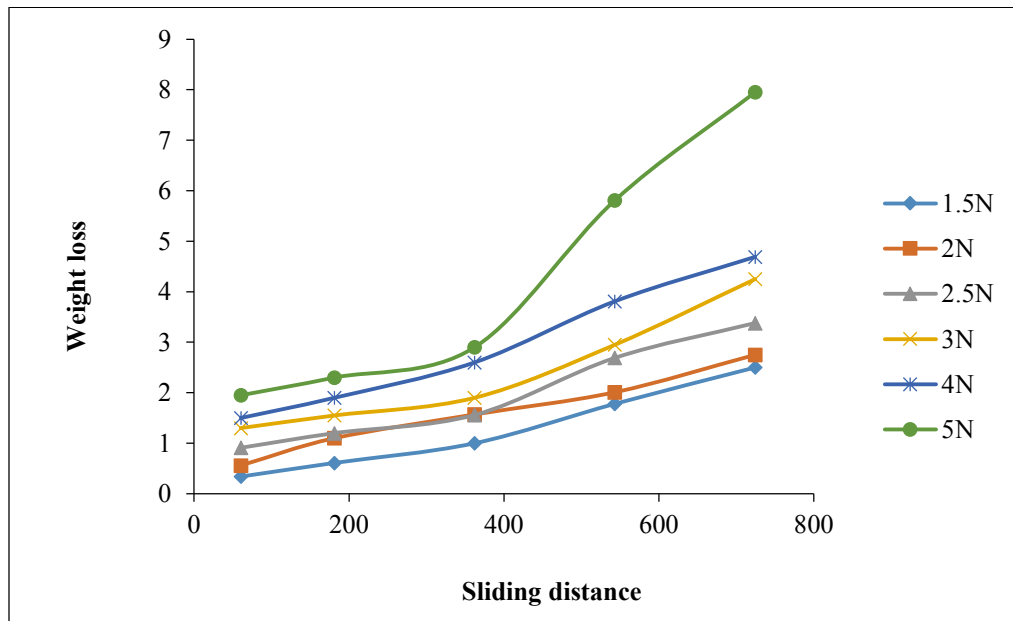
## **Appendix A: Raw Data**

Reciprocating ball-on-flat test results

(a)



(b)



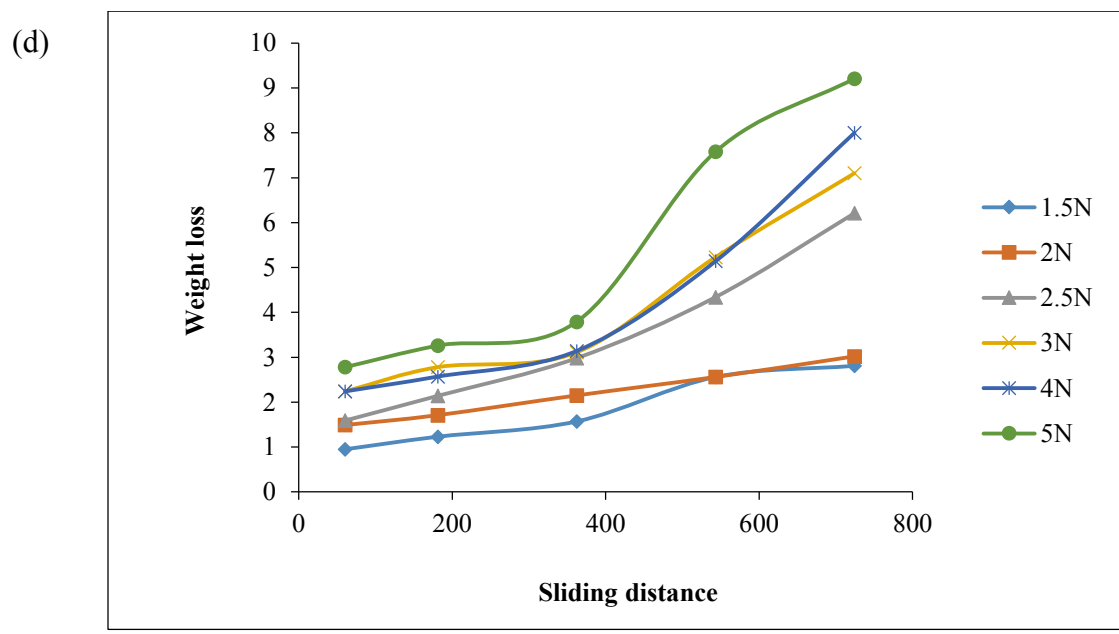
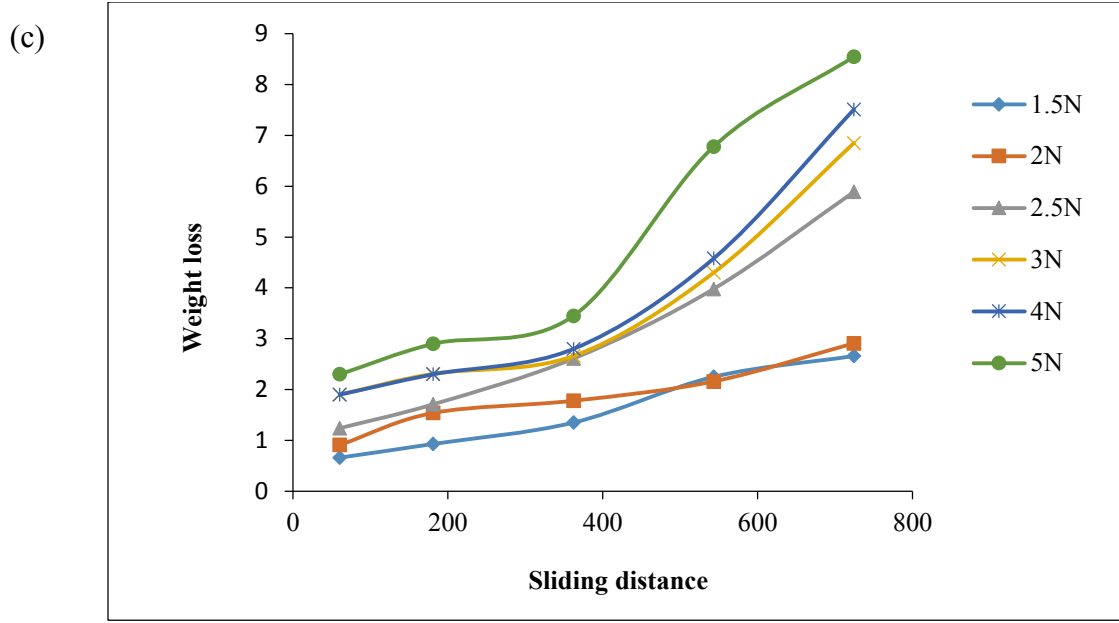
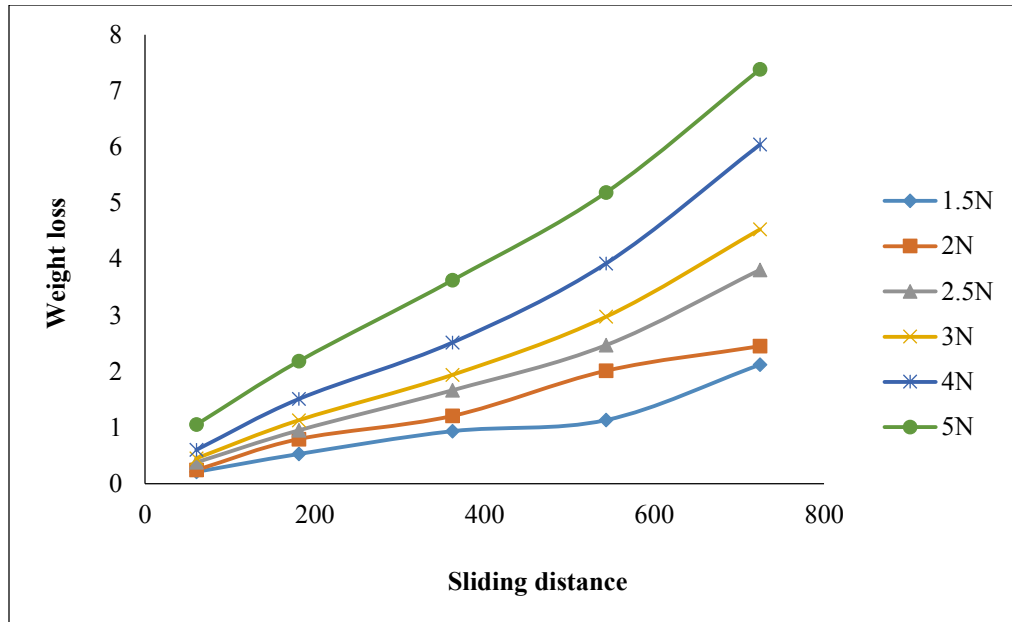
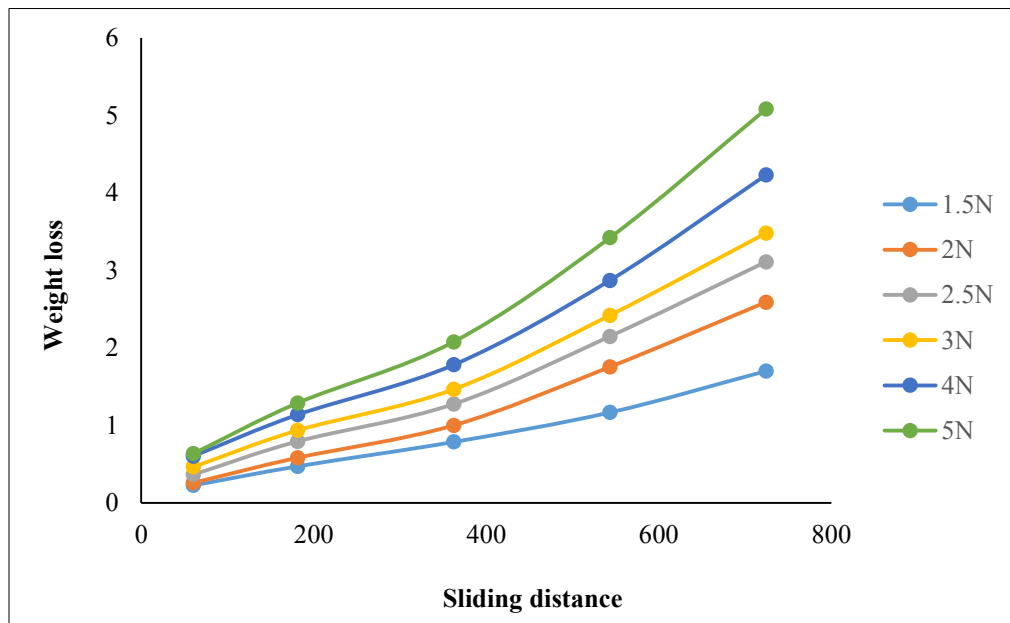


Figure A 1 Weight loss vs sliding distance for Pure Al with porosity a) 1.9% b) 5.8% c) 12.7% d) 15.1%

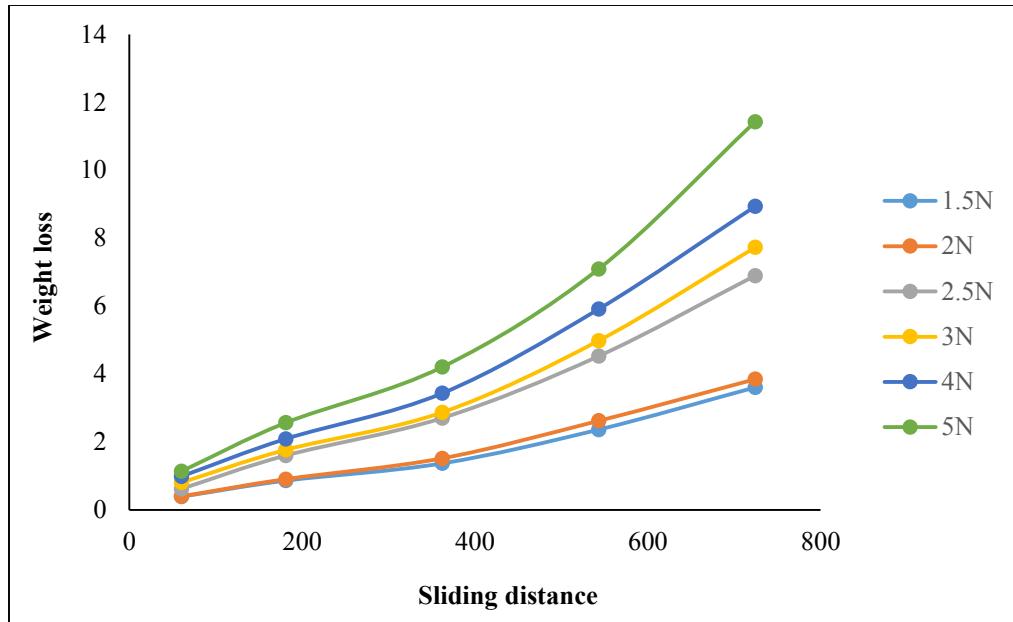
(a)



(b)



(c)



(d)

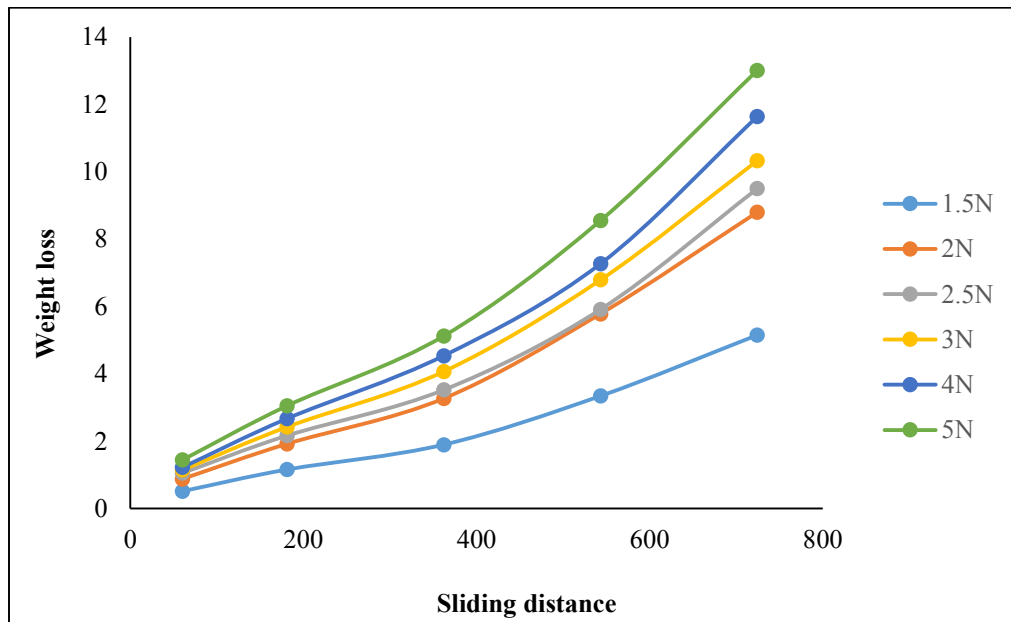


Figure A 2 Weight loss vs sliding distance for Al 6061 with porosity a) 3.5% b) 10.3% c) 16% d) 20.7%